8-2003

A computational approach to understanding material system : infrared coating of Ni-P on steel

Peter Gregory Engleman

To the Graduate Council:

I am submitting herewith a thesis written by Peter Gregory Engleman entitled "A computational approach to understanding material system : infrared coating of Ni-P on steel." I have examined the final electronic copy of this thesis for form and content and recommend that it be accepted in partial fulfillment of the requirements for the degree of Master of Science, with a major in Materials Science and Engineering.

<div align="right">Narendra Dahotre, Major Professor</div>

We have read this thesis and recommend its acceptance:

<div align="right">Accepted for the Council:
<u>Dixie L. Thompson</u></div>

<div align="right">Vice Provost and Dean of the Graduate School</div>

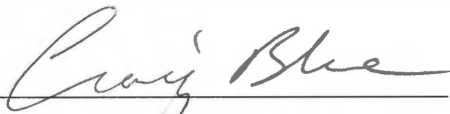(Original signatures are on file with official student records.)
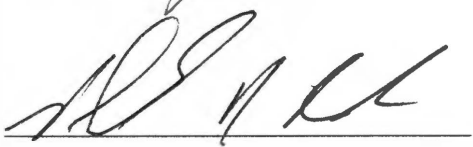
To the Graduate Council:

I am submitting herewith a thesis written by Peter Gregory Engleman entitled "A Computational Approach to Understanding a Material System: Infrared Coating of Ni-P on Steel". I have examined the final paper copy of this thesis for form and content and recommend that it be accepted in partial fulfillment of the requirements for the degree of Master of Science, with a major in Materials Science and Engineering.

_____
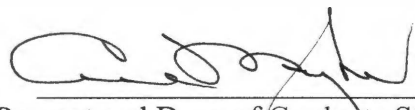Narendra B. Dahotre, Major Professor

We have read this thesis and
recommend its acceptance:

_____

_____

Acceptance for the Council:

_____
Vice Provost and Dean of Graduate Studies

A COMPUTATIONAL APPROACH TO UNDERSTANDING A MATERIAL SYSTEM: INFRARED COATING OF NI-P ON STEEL

A THESIS PRESENTED FOR THE MASTER OF SCIENCE DEGREE

THE UNIVERSITY OF TENNESSEE, KNOXVILLE

PETER GREGORY ENGLEMAN

AUGUST 2003

Dedication

This thesis is dedicated to my very supportive friends and family, especially my mother Barbara Engleman, my best friends Linda Lee Blaine, Tom Zobrist, and Mary Elizabeth Peterson, and to my advisors Drs. Craig Blue and Narendra Dahotre who pushed me even when I was being stubborn and who became more than just advisors.

Acknowledgements

I wish to thank all of those who assisted me in completing my thesis for Master of Science in Materials Science and Engineering. Thanks to my major professor Narendra Dahotre and Dr. Craig Blue of Oak Ridge National Laboratory (ORNL), for their guidance and perseverance. Many thanks to Dr. Suresh Babu, of ORNL, for his guidance in using Thermo-Calc™ and Dictra and to Larry Walker, of ORNL's High Temperature Materials Laboratory (HTML), for his assistance in obtaining the line scan and X-ray maps needed to complete the analysis for this project. Thanks to the technical staff at ORNL with special thanks to Randy Howell and David Harper for their patience and guidance when needed. Thanks also to the technical staff at the University of Tennessee Space Institute-Center for Laser Applications (UTSI-CLA), Knoxville, especially Diane Scarborough and Corey Fletcher for their assistance in using the always fickle yet improving software and equipment at the CLA.

Thank you Dr. Philip Rack, of the University of Tennessee, Knoxville, for serving on my thesis committee.

Abstract

It is thought that Ni-P can be used as a binder for ceramics (WC, TiC, etc.) used in coating applications such as those for corrosion and wear resistance. It is the intent of this study to use existing, commercially available models, such as Thermo-Calc® and Dictra®, to predict what phases will be present, in what quantities, and where, with respect to the interface, these phases can be found for Ni-P coatings fused on steel using high-density infrared processing techniques. It is also the goal of this study to attempt to predict the amount of co-diffusion that will occur between the coating and substrate materials and what effect(s) this will have on the material properties.

High-density infrared processing offers a method for close process control. Since it is a cold-wall technique, the specimen is heated directly and begins cooling immediately when the furnace is shut down. Using infrared processing also allows close control of time and temperature parameters providing the ideal environment for exploring diffusion controlled experiments.

Table of Contents

List of Figures

xvii

1. Introduction

It is often desirable to impart certain properties of one relatively expensive material to a less expensive substrate by applying a thin coating of the former to the latter[1]. Ni-P coatings are widely used in the chemical, mechanical and electronics industry because they offer good wear and corrosion resistance, strong adhesion, tend to be good diffusion barriers, and are generally wet well by many commercially available solder alloys[1,2,3].

Metallization schemes for nickel-based alloys are of current interest to prevent excessive intermetallic formation during processing (packaging/fabrication) and during operation (or in service) of electronic devices[4]. While the formation of a thin intermetallic layer, due to reaction between the solder and the substrate during fabrication, is desirable to achieve a good metallurgical bond, excessive intermetallic growth may have a deleterious effect[3,4]. Often, the intermetallic layers are brittle and degrade the fatigue and fracture strengths of the solder joints[5], leading to poor reliability. Therefore, it is necessary to understand and control the factors that govern the kinetics of interfacial reactions[4,6,7]. The rate and extent of growth of the intermetallic layers in solder joints are determined by several factors, such as the metallurgy of the substrate and coating, processing and operating conditions[4].

Phase diagrams are useful for developing and optimizing process parameters and for understanding solidification mechanisms of multicomponent systems[8]. Recently, substantial progress in solidification science has been made[9,10,11,12,13,1415]; thermodynamic

databases and calculations have reached a level where they are becoming useful and easier to implement for solidification modeling of multicomponent alloys[9,16,17,18]; despite this success, faster computation algorithms for delivery of phase diagram information to solidification models are needed to treat practical alloys[9,19,20]. The solidification community makes extensive use of diffusion analysis in liquids and in solids to predict such things as phases present and microstructure[9,21,22,23,24]. More recently, multicomponent versions of dendritic growth theory and solid (back) diffusion analysis have become available[9,19,20], however, data and analysis are still required to assess their importance.

On a more fundamental level, active research is beginning to understand the details of the instabilities of two-phase eutectic growth in ternary systems[9,17,25]. Both cellular (colony) and dendritic structures composed of two solid phases can exist[9]. Occurrences of ordering can be observed near well-defined stoichiometric compositions in some solid solutions[26]; in some cases the incidence of these ordered phases are restricted to small regions near an ideal stoichiometric composition and their boundaries in the phase diagram are well defined by miscibility gaps[26]; in other cases a phase boundary that would separate the ordered phase from the surrounding disordered alloy cannot be detected and is confined to temperatures below a definite phase transition temperature[26].

As stated above, more data and analysis are required to assess the importance of the models. Infrared processing provides a method where close control of both the specimen temperature and the time at temperature is inherent to the process. This close control of

2

time and temperature means that the experimental results can be more accurately compared to the theoretical results.

In this study, Dictra™ and Thermocalc™ were used to model the constituent diffusion and the phases present, respectively, for a Ni-10 (wt %)P coating applied to an AISI A570 (Table 1) steel substrate. The coating was applied using room temperature aspiration techniques and was fused in a small infrared furnace where the temperature of the specimen and the time at temperature could both be closely monitored. Several specimens were processed at varying times and temperatures; the specimens were then cross-sectioned and inspected using both light microscopy and an electron microprobe to compare with the data from the models.

Table 1 Coating and substrate composition.

Element (wt%)	C	Mn	P	S	Si	Cu	Ni	Fe
Coating	0	0	10	0	0	0	90	0
A570*	0.142	0.45	0.012	0.013	0.012	0.014	0	Bal.

---

* From certificate of analysis and tests received with steel, originating from Cargill Steel and Wire.

2. Literature Review

2.1 Computational Methods

It is essential to develop mathematical techniques designed specifically to permit thermodynamic calculations to be performed conveniently[17] and efficiently. The advent of modern computers has made it possible to perform these sophisticated thermodynamic calculations which were previously impossible[9,11,12,13,17]. Yet, the needs for better modeling are many and include: analytical models for single-phase cell growth; models for the cell to dendrite transition; models for eutectic growth with cellular and dendritic interface morphologies; and models for simultaneous two-phase growth in peritectic alloys[9]. More advanced problems include combining, numerically, phenomena that occur at different length scales, such as the coupling between phase-field models and computational fluid dynamics[9]. Of specific interest to this study is phase diagram and diffusion modeling in a multicomponent system.

2.1.1 Phase Diagram Modeling

If phase diagrams are to be calculated, then it is necessary to have means of expressing the thermodynamic properties of multicomponent phases as analytical functions of composition[17]. Many types of computer programs have been developed for the calculation of phase diagrams[17,18,20,27]. Analytical series expansions have been developed for representing experimental thermodynamic data of ternary and higher order solutions as functions of composition permitting the data to be stored in computer data banks, rendering computer-assisted thermodynamic calculations such as the calculation of phase

diagrams possible[17,18]. It has been shown that the order in which the binary and ternary coefficients are calculated is very important when the series expansions were used to calculate the phase diagram of a system that contains a ternary miscibility gap[17]. The modeling of thermodynamic properties as functions of concentration near non-stoichiometric compounds requires a different type of expansion than is necessary for the treatment of dilute solutions or of solutions with extended ranges of composition[17].

If there is a great difference in temperature between the region of solid demixing and the region of melting, then one has to consider the possibility that the interaction parameters might be temperature dependent[26]. When miscibility gaps or ordering tendencies in the solid state extend up to the melt temperature, an interaction parameter for the melt, positive or negative respectively, has also to be considered[26]. If it is the case that in a quasibinary system phases with different structures occur in addition to the excess Gibbs functions for all phases, then the data set describing the transformation between these phases must also be known[28]. Provided these data are given, the chemical potentials of the components A and B can be derived from the Gibb's Free Energy functions, and the phase diagram can be calculated by solving for the equilibrium conditions[26].

The major difference in the ternary system and binary system is the number of degrees of freedom; that is, there is one more degree of freedom in the ternary system when compared with the binary system[29]. This additional degree of freedom may show some effects that are not expected in the binary system during solidifiaction[29].

Pelton and Bale[17] have shown that it is possible, in principal, to calculate the Gibb's free energy for an element from the data available for a ternary system without making any measurements in the binary system of interest. In practice however, the experimental data are rarely of sufficient precision to permit this method to be used because the accuracy of this method is dependent upon the precision of the experimental data in regions of the ternary phase diagram where the partial derivatives may change rapidly with composition[17]. This problem can be avoided by first determining the coefficients for the secondary and tertiary elements from the binary phase diagram and then by incorporating the coefficients into the expression for the Gibb's free energy for the element in question[17]. Pelton and Bale[17] also imply that this method may not work when the ternary system was only checked over a limited composition range.

The Kohler approximation is another method that has been used to calculate large numbers of ternary phase diagrams[17]. In cases where only a few isolated ternary data points are available then the extended Kohler equation can be used to guarantee a reasonable behavior of the ternary thermodynamic properties over the composition regions where measurements are not available[17]. However, if extensive ternary data is available over a large range of compositions, then it is preferable to use the simple polynomial expansions[17].

In those cases where order-disorder transformations occur, and where the ordered low temperature modification is only a superstructure of the high temperature modification, this method of phase diagram calculations does not work any longer[26]; especially, if a

spinoidal miscibility gap within an ordered phase occurs. In the case of magnetic ordering effects the specific heat, c_p, functions due to ordering can sometimes be derived using the concept of critical exponents[26]. However, in ordered phases with structural vacancies no theory on critical exponents exists[26], however, in many cases the critical temperature of the order-disorder transitions would occur beyond the liquidus temperature[26].

Directional solidification studies of binary alloys with compositions in the two-phase region of the peritectic phase diagram at large temperature gradient to interface velocity, G/V, ratios to suppress the morphological instability of both the parent (α) and the peritectic phases (β) –each phase grows as a planar front[9]. Even in this simplified case, a rich variety of microstructures has been identified that are sensitive to the relative importance of nucleation, diffusion and convection[30,31,32]. These microstructures can be broadly classified into the following groups based on geometric patterns and underlying transport mechanisms: (a) discrete bands of the two phases; (b) partial bands or particulates (or islands) of one phase in the matrix of the other phase; (c) single primary to peritectic phase transition; (d) simultaneous growth of the two phases with a planar solid-liquid interface; (e) dispersed phases due to nucleation ahead of the interface; and (f) oscillating continuous tree-like structures of the primary phase that are surrounded by the peritectic phase[9].

2.1.2 Solidification Modeling

In the one-dimensional model of discrete band formation, it was assumed that the nuclei of the new phase spread rapidly in the lateral direction, so that no appreciable lateral gradients exist[9]. Because the relative rates of spreading and growth of the parent phase must be considered, this is generally not valid[9]. In most metallic alloys microstructure formation is controlled by solute diffusion and curvature, with heat diffusion occurring over much longer times. Simulation at this level normally requires following the interface separating the solid and liquid phases (front tracking)[33,34].

The practical application of solidification modeling to is closely linked to the ability to model microstructural development in multicomponent alloys (three or more components)[9,17]. One situation peculiar to ternary systems is the formation of eutectic cells by the presence of a dilute ternary solute[9]. Solutions of the full diffusion equations have been performed using DICTRA™[19], a diffusion analysis code build on top of Thermo-Calc.

2.1.3 Microstructure Modeling

Clearly microstructure modeling is strongly dependent on the input parameters. Thus the quality of phase diagrams and of system properties such as diffusion coefficients, interface energies (and their variation with orientation, temperature, and composition), etc. are of great importance and should be measured and calculated more precisely[9].

Nucleation typically plays a significant role in the solidification of undercooled melts such as that observed in the solidification of droplets. Microstructure correlates very strongly with droplet diameter and also with the availability of nucleant sites and the cooling rate[35]. Under given conditions it is usual for one phase to dominate, but the primary phases can also be mixed. There are many examples in which the phase competition is between BCC and FCC phases, and this has been most closely examined for Fe-Ni[9]. In the Fe-Ni-Cr system, it has been shown that the FCC or BCC phase can be selected through the use of an appropriate substrate put in contact with the droplet to trigger solidification[35]. "Inverse modeling" starts with information about the microstructure and optimizes the input parameters such as the phase diagram [36]. This new approach to determine stable and especially metastable phase equilibria is useful in cases where conventional techniques do not work[9,36].

Mixed control is always found when both nucleation and growth play a controlling role in the microstructure selection, such as in the columnar to equiaxed transition of dendritic or eutectic structures or in low velocity microstructures in the two-phase region of peritectic systems[9].

The irregular solution formalism works satisfactorily, only if the excess Gibbs Energy for a solid solution region without ordering effects has to be calculated. But, this formalism cannot cover simultaneously both ordering effects and spinoidal demixing in the same phase[26]. The behavior of the thermodynamic factor and also some features of the phase

diagrams might be better understood, if the phenomenological description of the excess Gibbs energy could be replaced by a derivation based on a model[26].

2.1.4 Available Methods

Modeling of microstructure formation in materials processing has progressed dramatically over recent years, especially in the fields of recrystallized structures[37,38,39], of grain formation in solidification processes[40], and of dendritic growth[23]. It has also become increasingly important in predicting microstructural defects and final mechanical properties[21].

One problem that with most of the existing models is that they are restricted to binary alloys with substitutional solutes[13]. With these models, calculation of diffusion for substitutional species requires that the back diffusion of the solvent be calculated, thus conserving the number of moles. For an alloy with interstitial solutes, these models are not applicable because back diffusion of the solvent is not required, thus the number of moles is not necessarily conserved, possibly causing an error[13]. Another problem is the lack of models that are able to treat multicomponent alloys, as most commercial alloys are multicomponent[13]. There were several models[33,34], which can describe the multicomponent alloy solidification, but they were limited to one-dimensional problems (for example DICTRA™ code) and cannot describe pattern formation, solute trapping, solute drag and paraequilibrium phenomena in multicomponent alloy solidification[13].

2.1.4.1 Phase Diagram

Shah et al. state that there are many computational methods for calculating the melting

point of alloys and compounds and that the result of these simulations is a theoretical

metastability limit rather than a thermodynamic melting point[41]. Rapid development of

thermodynamic software packages, such as ThermoCalc™, has made it possible to

calculate the complex phase equilibria in multicomponent systems. It is evident that

gradually, the accuracy of these calculations will become more and more dependent on

the databases behind the packages[16].

2.1.4.2 Microstructure

Phase field modeling has the ability to describe the complex pattern formation in phase

transitions such as dendrites[13]. This is a useful method for realistically simulating

microstructural evolution involving diffusion, coarsening of dendrites and the curvature

and kinetic effects on the moving solid-liquid interface[13]. It is efficient because all the

governing equations are written in a unified form without distinguishing the interface

from the solid or from the liquid phase[13]. In the model, the phase field characterizes the

physical state of the system at each position and time[13]. The phase field variable, φ,

changes steeply but smoothly at the solid-liquid interface region, which avoids direct

tracking of the interface position. Therefore, the model can be regarded as a type of a

diffuse interface model, which assumes that the interface has a finite thickness and that

the physical properties of the system vary smoothly through the interface[13].

Unfortunately only a limited number of systems have been modeled using the phase field

model, due to the magnitude of the calculations involved.

2.1.4.3 Solidification and Diffusion

In multicomponent solidification, no general relationships exist among temperature, interface velocity and concentration[7]. Most phase field approaches for alloy solidification[14,15,20,23,42,43] use a mole fraction as the concentration variable and are limited to the solidification of binary alloys[13]. Thus, they are not useful for an alloy system with interstitial solutes, due to the difference in diffusion mechanism between an interstitial and a substitutional species[13]. If substitutional, the diffusion of a solute requires the back diffusion of the solvent and the number of moles per unit volume is conserved at $1/\Delta$, where Δ is the partial molar volume[13]. If interstitial, however, the back diffusion of the solvent is neither required nor the number of moles is conserved[13].

It is essential to the use of phase-field formulation as a useful computational tool that solutions may be computed which have an interface thickness much larger than that which occurs in reality[11]. Such a realistic thickness would require numerical resolution of the phase field over an impracticably large range of length scales from atomic to macroscopic dimensions[11]. For the most part phase-field models have provided a new formulation of well-known free-boundary problems associated with solidification and have not generated new models[11]. There are two areas where phase-field models have been particularly effective; including the WBM1 and WBM2 models, Warren, Boettinger, and McFadden[11], theory of solute trapping, and the computation of complicated realistic interfaces such as dendrites and coarsening[11].

One hope comes from the continuing development of the thermodynamic based databank for multicomponent liquids and solids such as DICTRA™[9]. Such an approach naturally includes concentration dependent and off-diagonal diffusion terms[9]. Even ignoring these problems, difficulties remain with coupling dendrite tip models to subsequent solidification path calculations, especially for unequal (diagonal) diffusion coefficients in the liquid[9]. In addition, more accurate models for solute diffusion in multiphase eutectic and peritectic structures during solidification are needed[9].

2.2 Experimental

2.2.1 Nickel-Phosphorus

The use of electroless nickel-phosphorus coatings in industry in both their basic form and as composites with ceramic dispersions is well established[44]. Brenner et al. have reported the electrodeposition of nickel-phosphorus coatings as far back as 1950[45], and although the process has had little effect on industrial practices, a number of studies have been performed concerning the structure and properties of deposits obtained using electrodeposition[45,46]. In addition to the work carried out using electroless and electrodeposition methods, work has also been performed using the pulse plating method and superimposed pulsed current on the electroless process[44]. Electroless deposition of nickel-phosphorus coatings tend to have low residual stresses unlike Ni films prepared by vacuum deposition which tend to have very high residual intrinsic stresses[2]. Additionally electroless deposition of Ni coatings offers a low cost alternative to physical deposition methods[2].

Crystallization of the amorphous Ni-P coating may be enhanced by reaction with the solder alloy; indeed Jang, Kim, Tu, Frear, and Thompson[2] have observed a correlation between crystallization and a change in the composition of the amorphous matrix[2]. This is different from self or thermal crystallization in that for thermal crystallization the amorphous and crystalline phases both have the same composition, while "reaction-assisted" crystallization where the crystallization is enhanced by the reaction kinetics[2]. In general, self-crystallization of amorphous Ni-P coating occurs at temperatures above 250°C and after hours of annealing[47,48] and is a process typical of nucleation and growth[47,48,49,50], depending upon the Ni/P ratio, and the annealing temperature and time[2]. It should be noted here that because the Ni-P system is a two-component system with several compounds, the crystallization products are not as simple as those found in a one-component system[2]. In the case of metal-phosphorus systems it is expected that a change in bond type, from metallic to non-metallic, should take place as one moves from the metallic to the phosphorus end of the system[51]. Chandrasekaran et al. have shown that in transition metal-phosphorus alloys with compositions ranging up to 50 at% P, the metallic bond is predominant and that the volumes associated with these structures persist over most of the composition range of metal-phosphorus alloys[51].

Nickel-phosphorus coatings are generally produced on low-alloy steels, aluminum, magnesium, and copper alloys as well as on plastics and ceramics[52]. When corrosion resistance is required, as-deposited are preferred since the aging treatment reduces corrosion resistance[53].

Nickel-Phosphorus alloys suffer from poor formability and low ductility, but their desirable properties make them a candidate for application as a coating. Therefore, nickel-phosphorus is a poor choice to be used where it is important to relieve stress due to its low ductility[6].

2.2.2 Infrared Processing

Infrared processing offers a quick and cost-effective method for the joining and brazing of advanced materials[54]. Upon terminating the power, the specimen temperature drops instantly since the furnace wall is not heated up by the infrared processing[54,55]. Infrared joining, a rapid isothermal processing technique[55], has been widely used in the electronics industry[56] because it offers a quick and cost effective method for the joining of advanced materials[55]. Lee et al. adopted infrared joining in their study due to its sensitive thermal response, its rapid, simple and economical advantages[57,55], and because the microstructural evolution of the joint interface can be effectively realized due to the sensitive response of infrared joining[57].

Infrared processing offers the advantages of low cost, independent of specimen size, can be implemented for high volume production, and it offers high controllability and repeatability. Due to the inherent nature of the process, the coatings are diffusion bonded to the substrate, resulting in a tenacious bond between the coating and the substrate, IR processing of Ni-P coatings does not require an interlayer.

2.2.3 Bonding

2.2.3.1 Transient Liquid Phase

Reactive isothermal solidification is the process in which a system that contains both liquid and solid phases undergoes solidification at a constant temperature through the formation and growth of intermediate phases resulting from mass transport processes and chemical reactions[58]. The kinetics and mechanisms involved in reactive solidification are not clear[58]; the process can be regarded as reactive diffusion in a solid-liquid couple[59]. In some binary systems, only one of the equilibrium intermediate phases grows during the process[60,61,62,63], and the growth kinetics of the intermediate phases were found to deviate from the expected parabolic behavior of bulk diffusion-controlled growth[59,62,63].

Conventional transient liquid phase (TLP) diffusion bonding has been of interest when joining advanced alloys and metal matrix composites for which neither fusion welding nor solid-state bonding methods might be successful[64]. Interdiffusion between the interlayer and the base material leads to the formation of a low melting point liquid phase (e. g. eutectic) at the bonding temperature which is held constant[64]. In this method, as in any fusion welding method, the formation of a liquid phase can assist in the disruption of the oxide layer and promotes metallic bonding[64]. Bond strengths as high as those of the parent materials have been reported when using this method to join several aluminum alloys with copper interlayers[65,66]. The highest bond strengths are in fact achieved with specimens showing a particular level of waviness of the bond line[24]. This means that, for a successful bonding process, it is important to promote the formation of interfacial

17

instabilities, but it is equally important to prevent the excessive growth of such instabilities in order to avoid unfavorable microstructures[24]. In contrast to fusion welding methods, the bonding temperature when TLP diffusion bonding is much lower than the melting point of the base material and therefore any detrimental effects on the parent material are minimized[64]. In TLP bonding, a solidification reaction occurs with the composition of the bond tending towards the overall composition[67]. The kinetics of this solidification reaction is expected to be strongly dependent on the bonding parameters such as temperature of joining, heating rate, and metal thickness used[67].

Assadi, Shirzadi, and Wallach[24] have developed a variation of the TLP method where a temperature gradient is imposed upon the bond joint that they refer to as temperature gradient-transient liquid phase (TG-TLP) diffusion bonding. In conventional TLP diffusion bonding, isothermal solidification is assumed to occur simultaneously at both advancing solid/liquid interfaces as a consequence of continued diffusion of solute from the liquid phase into the adjacent solid phases, i.e. bilateral counter-flow movement of the solid/liquid interfaces[24].

During isothermal solidification in conventional TLP diffusion bonding, any insoluble oxide particles and impurities, trapped within the liquid phase, are pushed forward by the advancing solid-liquid boundaries[64]. Eventually, these particles agglomerate at the bond line and also prevent metal-to-metal contact from being fully established[64]. Therefore, the shear strengths of such joints are found to be somewhat less than the shear strengths of the corresponding parent materials[64]. In addition, the random distributions of oxide

18

particles at normally flat interfaces or bond lines cause wide scatter in the mechanical strengths of the bonds[64]. The flat interfaces themselves may also limit bond strengths[64].

A novel method for TLP diffusion bonding has been developed that is capable of providing excellent bonds with parent material shear strengths[65]. This method relies on imposing a temperature gradient across the bond line when TLP diffusion bonding rather than maintaining a uniform temperature during bonding[64]. This results in sinusoidal or cellular interfaces[64,66]. Bond strengths are thus increased, possibly due to the higher metal-to-metal contact along the non-planar interfaces as compared to the planar interfaces associated with either conventional TLP or solid-state diffusion bonding processes[64]. The kinetics of a TLP process would at first sight, appear to depend largely on the overall diffusivity of solute (from the liquid phase) in the solid parent material[64]. If the diffusion coefficient in the solid is assumed to be zero, the solidification stage theoretically would never occur because the solid/liquid boundaries could not move, i.e. would be locked due to a lack of diffusion in both the liquid (once homogenization has been achieved) and also the solid phase[64]. The composition of the liquid would become fixed[64]. An additional feature of imposing a temperature gradient during TLP diffusion bonding is to produce a non-planar bond line which can lead to improved mechanical properties of the resulting bond[64].

Lee et al. showed that due to segregation during isothermal solidification, some regions may contain higher contents of some of the elements than the original coating alloy[55].

2.2.3.2 Diffusion

Solid-bonds with rather good joint properties can be acquired by diffusion bonding, the long processing time and the high corresponding operation/installation costs may render this joining method useless for practical applications, especially for joining large-sized work pieces[55]. It has been shown in the case of the titanium/aluminum system that the slow heating and cooling rates of conventional furnaces do not easily provide desirable joint properties due to the long-elevated heat history[55]. Because of the complexity of the metallization scheme and the multicomponent nature of the diffusion couples, it is imperative to rationalize the origin of the interfacial microstructure in terms of the diffusion path, which is the average composition in a direction perpendicular to the original interface plane of the diffusion couple[4] (Figure 1).
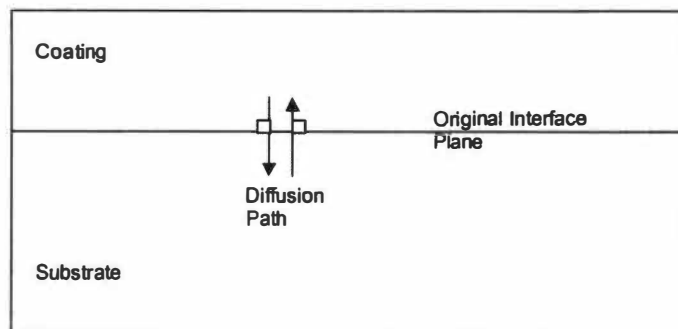
Figure 1 The diffusion path is the average composition in a direction perpendicular to the original interface plane of the diffusion couple.

2.2.4 Microstructure

The preferential substitution site of alloying elements is likely to have an important influence on thermodynamic properties (and mechanical properties as well) of compounds[68]. Phosphorus has been reported to embrittle iron[69]. The addition of carbon was shown to reduce the influence of phosphorus on embrittlement[69]. When carbon was added ($\leq$80 ppm), the grain-boundary phosphorus content decreased[69]. Metalloids such as phosphorus, arsenic, antimony and tin produce embrittlement of carbide/ferrite and surrounding ferrite/ferrite interfaces[69]. This appears to be a non-equilibrium segregation problem however[69]. A study of iron by phosphorus, phosphorus and sulfur, and antimony and sulfur demonstrated that the embrittlement was different in that it was not reversible[69]. Segregation occurred at all temperatures in ferrite but was negligible or limited in austenite[69].

Phosphorus was reported to be 50 times more prevalent at the grain boundaries as in the grain interiors[69]. Specimens were fractured within the Auger chamber[69]. Phosphorus was observed on the surface of intergranular fractures, but not on the cleavage fractures[69]. Auger analysis showed that the amount of phosphorus on the intergranular fractures increased with bulk phosphorus content[69]. As the aging temperature decreased, the grain-boundary phosphorus increased and the fracture became more intergranular[69]. When quenched from the two-phase region, fractures did exhibit phosphorus at the grain boundaries[69]. When an Fe-0.2P alloy was furnace cooled from the austenite region, the

fracture surface exhibited a layer of nearly pure phosphorus at the grain boundary with a thickness of 1 to 1.5nm[69].

Phosphorus does substantially increase the strength of ferrite[69], and the presence of phosphorus in the nickel-phosphorus coatings proves to be very important because hardnesses of >1000HV are possible simply by heat-treating the piece[52]; but, elements such as silicon, phosphorus, sulfur, oxygen, and nitrogen have been show to be detrimental to nickel-base superalloys and have to be controlled through appropriate melting practices[69].

Lee et al. found in their studies involving the infrared joining of TiAl intermetallics[57] that a multilayered interfacial microstructure was formed by the atomic interdiffusion at high joining temperatures which included isothermal solidification of new solid layers and the following solid-state interdiffusion between these layers and the base metal. Due to the solid-state interdiffusion, the multi-layered interfacial structure formed at the processing temperature phase-transformed to the room-temperature microstructures during rapid cooling[57]. Because the atomic diffusivity in liquids is rather fast, the cooling solidification effects may occur and effect the composition at the interface during fast cooling, even if the estimated cooling rate is as high as about 1000°C/minute[57]. At the onset of isothermal solidification, the liquid/solid interface is unstable due to the rapid atomic interdiffusion rates and the dissolution effects of the base metal[57]. According to Kirkaldy[70] and van Loo[25] a columnar two-phase zone is produced when a diffusion path passes through a two-phase region from a single-phase region at an angle to the tie lines,

but then exits into another phase[57]. Lee et al. found this to be true of the TiAl system bonded with Ti-15Cu-15Ni foil, they also found that for longer processing times the liquid/β interface will successively move inward and gradually become planar, which is a more stable interface based on the surface energy lowering principle[57]. This analysis is based on the ideal case in which no lateral diffusion occurs and all of the α-Ti columns are equal in size on the cross-sectional plane. However, some lateral diffusion is unavoidable in real cases and will cause the diffusion direction not to be completely perpendicular to the original joint surface, producing a rather ragged joint interface morphology[57]. Also of concern is that the kinetic effects of the processing temperature will act on the microstructural evolution, such as the relative diffusivities of the elements[57]. The higher the joining temperature, the faster the atomic interdiffusion rate and the higher the moving plane velocity will be (where the moving plane can be the solidification, liquification or transformation plane)[57]. Therefore, specimens joined at higher processing temperatures with similar processing times will produce thicker solid-state layers and the formation of certain phases may be hindered or enhanced[57]. So, the processing temperature mainly affects the kinds of stable phases and the stability of the individual phase in each joining condition[57].

As a liquid melt composed of two (or more) atomic species solidifies, the resulting solid typically has composition unequal to that of the liquid. This composition depends in part on the local conditions under which growth occurred, in particular on the rapidity of solidification[27]. As a result, the growth conditions largely determine the resulting solid microstructure and it material properties[27]. Furthermore, the solute redistribution in the

23

solid and liquid phases during primary solidification and the associated solidification path control the type and amount of intermetallic particles that form[22]. The growth direction, shape and kinetics of dendrites are strongly influenced by the anisotropy of the chemical potential, which is linked to the anisotropy of the interfacial energy (and its second derivative)[22]. In most common metals, the anisotropy of the interfacial energy is very small (a few percents), this making the problem even more difficult[22].

At high joining temperatures, as in this study, the volume diffusion will be the rate-limiting step with local equilibria existing at the interface. According to the principle of multiphase diffusion in binary[54] or ternary[70] solid-state systems, it is reasonable to suggest that each domain corresponds to one of the stable phases formed at the joining temperature[55].

3. Theoretical and Experimental Procedures

3.1 Computational Procedures

Thermo-Calc™ and Dictra™ are commercially available software packages that are commonly used in industry, research, and educational environments. Thermo-Calc™ is primarily designed to perform thermodynamic calculations, while Dictra™ uses the Thermo-Calc™ engine to perform diffusion modeling. Thermo-Calc™ and Dictra™ were chosen for use in this project because of their commercially availability, their widespread usage, their relative ease of use, and because their ability to be used together to model a system allows for more consistent results. More detailed procedures for using Thermo-Calc™ and Dictra™ can be found in Appendix A.

3.1.1 Diffusion Modeling using Dictra™

In order to get the most accurate results, the model must be constructed in such a way that it best mimics real world conditions. Dictra™ restricts the construction to one dimension, which is generally represented horizontally (Figure 2). The nature of the problem dictated using geometric spacing of the test points about the interface, so, values of 1.1 and 0.9 were chosen for the geometric factor, R, for the substrate and the coating respectively, allowing the density of test points to increase with proximity to the interface.

The major elements, for the purpose of the interdiffusion calculations, were Fe, Mn, and P for the substrate material and Ni and P for the coating material (because carbon tends to

25
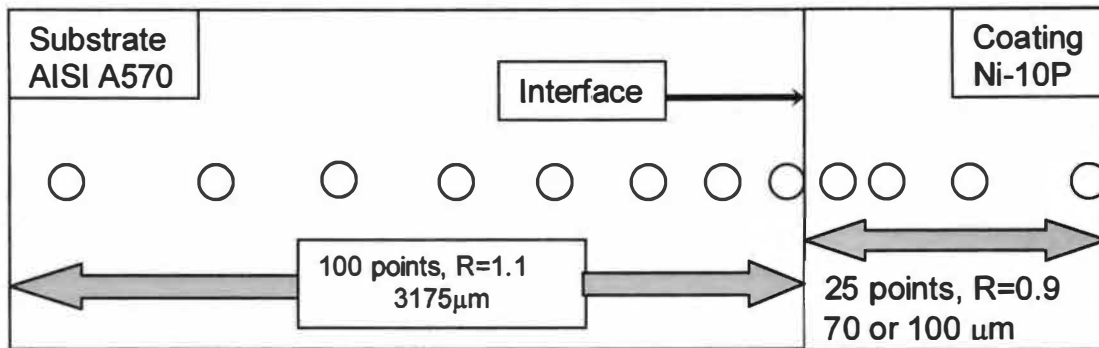
Figure 2 One-dimensional model of the Ni-10P/A570 system.

diffuse interstitially, it was not considered for the purposes of modeling per the reasons listed in the introduction[13]). The chemical compositions of the substrate (A570 Steel) and coating (Ni-P), given in Table 1, were used for modeling purposes. It was assumed that diffusion would proceed both from the substrate into the coating and from the coating into the substrate.

Two different coating thicknesses were modeled (70μm and 100μm) such that the actual coating thickness should fall between the two. The substrate thickness was designated to be 3.175mm (3175μm).

Once the composition, the thicknesses and the grid spacings were set for the substrate and the coating materials, modeling of the system was performed for four processing times, each at four different processing temperatures (Table 2). Due to the nature of Dictra™, it is not trivial to input heating and cooling profiles, it was assumed that heating to the processing temperature was instantaneous and that cooling from the elevated processing

Table 2 Processing times and temperatures.

Temperature (°C)	Specimen Number	Processing Time (s)	Coating Mass (g)
950	1	0	1.67
	2	1	1.74
	3	10	1.43
	4	20	1.42
975	5	0	1.67
	6	1	1.55
	7	10	1.42
	8	20	1.37
1000	9	0	1.51
	10	1	1.40
	11	10	1.47
	12	20	1.45
1025	13	0	1.50
	14	1	1.43
	15	10	1.39
	16	20	1.42

temperature to room temperature was instantaneous, i.e. there was no solid-state diffusion between the coating and substrate during heating or cooling.

After Dictra™ completed calculating the co-diffusion, diffusion of the coating elements into the substrate and visa-versa, diffusion profiles (distance vs. wt %) across the interface were plotted for each element at each time and temperature.

3.1.2 Phase Diagram Modeling using Thermo-Calc™

In order to gain a better insight of the results from the Dictra™ models, it is important to understand what phases might be formed. For the purpose of this work, Thermo-Calc™ was used to create a pseudo-binary phase diagram of the Ni-10P (wt %)/AISI A570 system. A detailed description of how to do this can be found in Appendix A. The phase

diagram was constructed by first associating the amount of P in the coating with to the amount of Ni and then by associating the amounts of the major constituents in the steel to the amount of iron, the system is reduced to a pseudo-binary system. Completion of the pseudo-binary phase diagram was accomplished by setting the X-axis to represent the composition as it varies from Ni-10P (100% by weight) to AISI A570 (100% by weight) and by setting the Y-axis to temperature (°C or K). The pseudo-binary phase diagram was then plotted. It is important to note that this is an equilibrium phase diagram and may not represent any non-equilibrium phases.

3.2 Experimental Procedure

Once the theoretical modeling was completed, it was essential to validate the models using experimental data.

3.2.1 Coating Alloy Preparation

Since a Ni-10 (wt %) P alloy without an organic carrier could not be procured, it was necessary to manufacture an alloy in-house. The alloy was prepared by carefully measuring out 100g of Ni_2P (spectrographically measured to be 21.34 wt % P) and 110.77 g of Ni powder that should yield a Ni-10.1 wt % P alloy. The powders were placed in a quartz ampoule. Prior to sealing the ampoule, a 100mTorr vacuum was pulled and the ampoule was backfilled with argon. This process was repeated two more times to ensure that the oxygen content in the ampoule was low. Finally, a –0.5 atmosphere vacuum was pulled on the ampoule to help control the amount of pressure that would build up on heating.

Once the powders were sealed within the ampoule, the ampoule was placed in a Blue M™ Rad-O-Glow® convection furnace. To melt and homogenize the powders to form the alloy, the ampoule was heated from 200°C to 1100°C over a period of 5-1/2 hours, held at 1100°C for ½ hour, shaken vigorously and quenched in a bucket of water. At this point it was necessary to check the composition of the alloy synthesized in the ampoule.

3.2.2 Substrate Preparation

Once the alloy was prepared for use, it was essential to have the AISI A570 steel substrate ready. The substrate was prepared by shearing 40 coupons, 51mm X 51mm X 3.75mm of AISI A570 steel from a single sheet (so that they would all have the same thermal and mechanical history). Any scale was removed by sandblasting followed by wire brushing to remove any embedded silica. Just prior to use the samples were finished using 600-grit sandpaper to remove any residual oxides and to ensure that all of the specimens had a similar surface finish. The coupons were then wiped down with acetone and methanol to remove any residue and to provide a clean surface for alloy adhesion.

3.2.3 Infrared Coating

Prior to application of the Ni-P coating to the A570 steel, a series of experiments were performed to determine the melting point and density of the Ni-P alloy.

During the following procedure, observations were conducted to determine the melting point of the Ni-P alloy. A small chunk, approximately 8g, of alloy was placed on an

29

A570 steel coupon, separate 1/32" K-type thermocouples were attached to the Ni-P alloy and the A570 steel coupon using a Unitek Peco model 1-251-03, spot welder. The coupon and the Ni-P alloy were placed in a small infrared furnace, built in-house, with the piece of alloy placed approximately in the center of the steel coupon. The infrared furnace consists of 22, 1500W tungsten-halogen (T3) bulbs, 10" long, arrayed radially within a water-cooled stainless steel reflector and around a 3-1/2" diameter quartz tube. The quartz tube serves as a specimen chamber with atmospheric control –a desired vacuum, or gas mixture can be applied within the tube. The furnace is controlled by a Yokogawa™, UP-550, PID controller and is capable of a theoretical maximum power output of 33kW.

Both thermocouples were attached to a computer equipped with a National Instruments™ data acquisition system using a LabView™ routine developed in-house. This system has the capability to handle up to 16 K- or S-type thermocouples and up to 500,000 samples/second. Using a 'Y', a special fixture allowing the thermocouple to be monitored by two instruments, the thermocouple attached to the A570 steel was used as the control thermocouple during heating.

Two furnace runs were performed to determine the melting temperature of the alloy, and to examine the ability of the Ni-P alloy to wet the A570 steel and to see how the alloy would flow. Both of the furnace runs were performed according to the following profile: start set point, 20°C; 210s to reach 700°C; wait until the control thermocouple was +/- 2°C; hold at 700°C for 30s; 300s to reach 1000°C; wait until the control thermocouple

was +/- 2°C; hold at 1000°C for 20s; allow to cool to room temperature in furnace (Figure 3). Prior to running each test, the furnace was evacuated to 150mTorr and backfilled with Ar-4%H a total of three times. Ar-4%H was flowed through the furnace at a rate of 0.5 SCFM for each trial.

The heating curve was examined to determine the temperature at which the endothermic melting reaction occurred, indicated by a horizontal portion of the heating curve. Chances for solid-state diffusion between the alloy and the substrate effecting the melting point measurement were minimized in two ways. First, the alloy was not mechanically joined to the substrate. Second, the alloy was significantly large enough and the heating time was short enough to prevent significant interaction.

Once the melting point of the alloy was determined, and by using the Ni-P binary phase diagram, the composition of the alloy could be determined by drawing a horizontal line across the phase diagram at the melting temperature (obtained from the heating curve of the alloy, Figure 4) and noting where it crosses the phase diagram. Since the approximate composition of the alloy is known, a vertical line can be drawn from the closest point, where the horizontal temperature line crosses the phase diagram, to the approximate composition. In this manner, a more accurate alloy composition can be determined.

In order to match the 70µ-100µm coating thickness of the modeled system, the density of the coating alloy had to be determined. Archimedes method for density calculation was
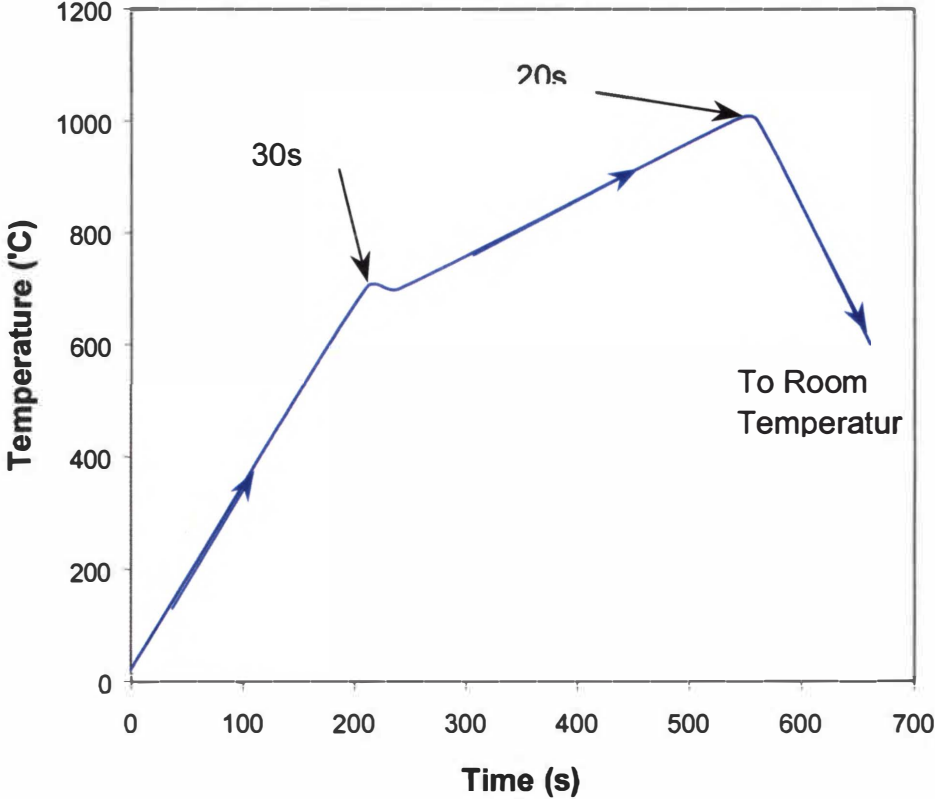
31

Alloy Heating Curve Schematic

Figure 3 Schematic representation of the heating profile used to determine the melting point of the Ni-P alloy.
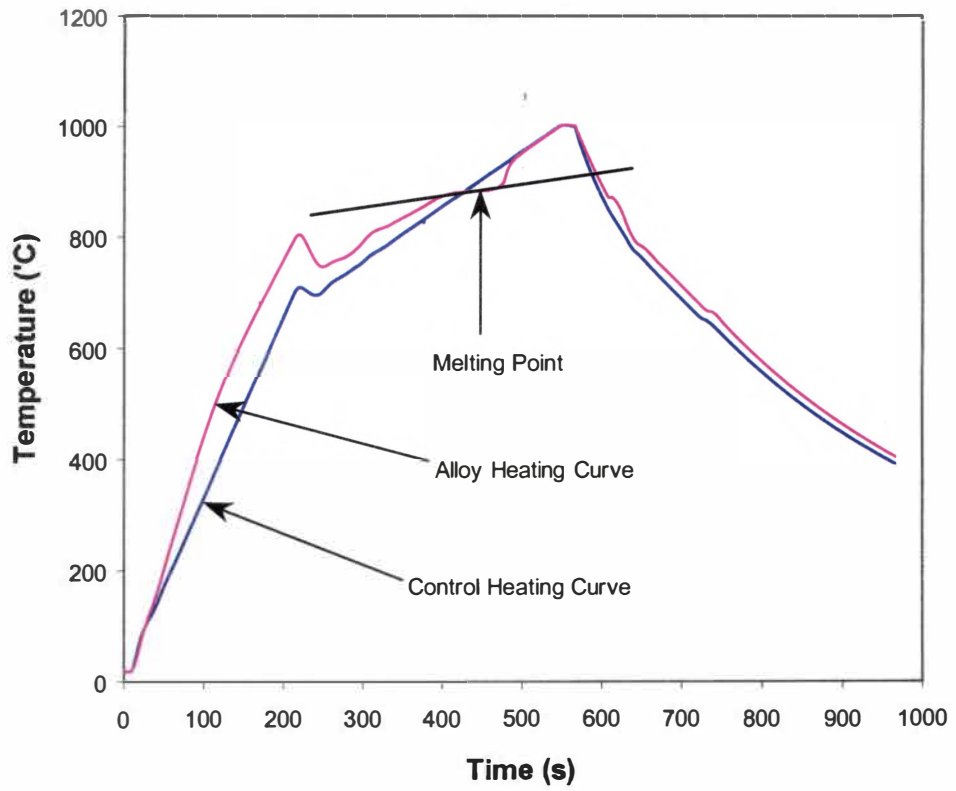
Figure 4 Heating curve showing the melting temperature of the Ni-P alloy.

used to accomplish this, using methanol as the displaced fluid.

Because the Ni-P alloy was determined not to flow, it was decided that it would be necessary to crush the alloy onto a powder that could be spread easily over the surface of a steel coupon. Crushing began by placing the alloy between two clean blocks of hardened, plain carbon steel and crushing in a hydraulic press. This process was repeated until the alloy was pulverized into small pieces. Further refinement of the powder was performed using a Tectator, model 1000-3811, pulverizer to reduce the powder to <850μm in size.

After the Ni-P alloy and the coupons were prepared, processing of the test specimens could begin. An uncoated coupon was used to set the furnace controller PIDs so that the sample would be heated to the desired temperature, +/-2°C, and so that the specimen would heat according to the defined profile without "ringing"[*]. Sixteen specimens were processed according to the times and temperatures in Table 2. A general heating profile was used to process all of the specimens, the only change made was in the final time and temperature. The general profile was as follows: start set point, 20°C; target set point, 850°C; time to temperature, 1s; this guarantees that the furnace will heat the specimen as quickly as possible to the set point temperature. Hold at 850°C for 30s to equilibrate specimen temperature; 1s to reach processing temperature (this ensures that the furnace reaches full power so that the specimen reaches processing temperature as quickly as

---

[*] Ringing is when the furnace intensity varies greatly to maintain the current set point.

possible); wait for specimen to reach its processing temperature, +/-2°C; hold specimen at processing temperature for the allotted time; shut down furnace and wait until the specimen temperature <100°C prior to removing from furnace. Before beginning each furnace run, the same evacuation and backfilling procedure listed under alloy preparation was used to minimize any oxidation of the sample during processing.

3.2.4 Microscopy Procedures

Once all of the processing was completed, all of the samples had to be sectioned, mounted, polished and etched so that their microstructure and composition could be examined using optical microscopy, SEM and microprobe methods. Each specimen was cross-sectioned through an area with a uniform coating thickness and finish using a Buehler, Allied Techcut 10™ sectioning saw with an abrasive cutting wheel. Each specimen was engraved with its processing temperature and time, after it was sectioned, to identify it. When all of the samples were cross-sectioned and labeled, they were mounted in Bakelite with all of the specimens of one temperature group mounted in the same mount and according to their processing time (Figure 5). The specimens were then polished using a Buehler Phoenix Beta™ grinder/polisher with 180-, 240-, 320-, 400-, 600-, 800-, and 1200-grit SiC paper. The final polish was accomplished with 0.3μm alumina paste making certain that all specimens had a mirror finish with no scratches visible at 10X in an optical microscope. Each specimen was then observed in the unetched condition using an optical microscope (Olympus model BX60M with IA32 v1.10 software by Leco Corp.) at 10X, 50X and 100X. The specimens were then etched to reveal the microstructure in the coating and the substrate. Etching was accomplished
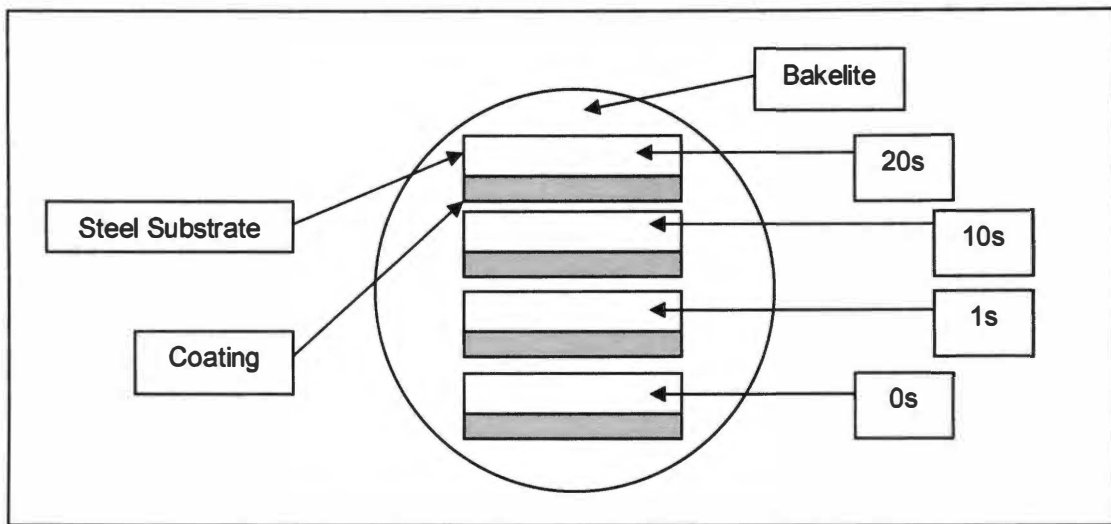
Figure 5 Specimen mounting configuration.

by submersing the mounted specimens in the reagent for a few seconds and then

observing the specimens until the desired effect was achieved. A mixture of 1:4 Nitric

(HNO_3) and Acetic (CH_3COOH) acids was found to etch both the coating and the

substrate, and a time of 40s was found to reveal the microstructure without overetching

the specimen. The microstructure was then observed using an optical microscope at 10X,

50X, and 100X to investigate both the coating and the substrate structures. A Jeol model

8200, electron microprobe was used to take SEM images and to perform quantitative

chemical analysis on the specimens, profiling the presence of Ni, P, Fe, and Mn in the

coating and substrate. Once the processing was complete, and the data was taken, the

data could be analyzed, comparing the physical and theoretical results.

36

4. Results and Discussion

4.1 Dictra™: Computational Diffusion Results

Dictra™ was used to model the co-diffusion of the coating and substrate materials. The results were used to plot the composition (wt %) vs. position curves for the major constituents, Fe, Ni, P, and Mn, of the system (Appendix B). The general trend that can be seen in all of the figures is that the interface appears to advance from the coating into the substrate (Figure 6). This is evidenced by the decrease of Fe and Mn and the increase of Ni and P on the substrate side of the interface. Figure 7 shows two plots for weight percent of iron versus position for the conditions 1025°C for 0s, 1s, 10s and 20s. Observation of the graph shows that the amount of iron near the interface is probably diffusion rate controlled. This becomes especially apparent for the longer hold times (curves 3 and 4 represent 10s and 20s respectively); a slight decrease in the percentage of iron is noticed on the steel side of the interface just ahead of the front, and a slight increase in the percentage of iron is seen on the coating side of the interface just behind the front.

The significance of diffusion rate control is in the phase formation and microstructure, which will be discussed later. Other general trends were observed from the diffusion modeling. For all of the elements modeled, it was clear that the diffusion distance increased with time for all of the elements at all of the temperatures. It is also apparent, as would be expected, that the solubility does increase with temperature (Figure 8). It
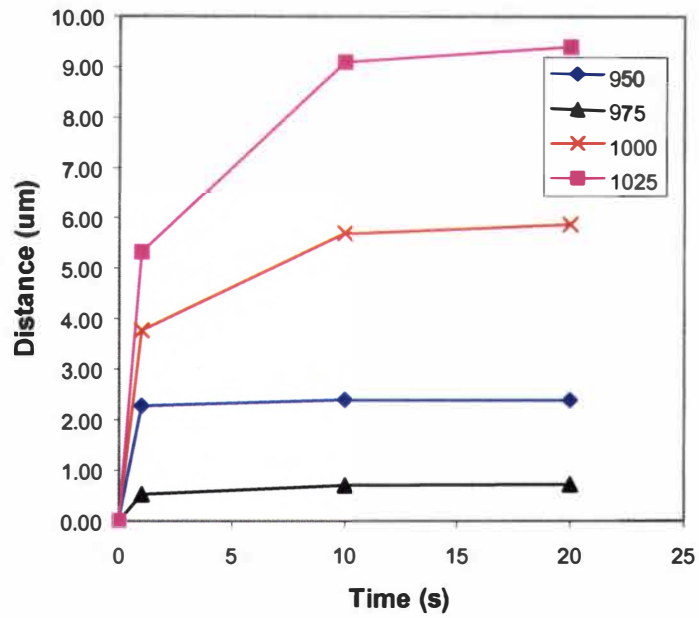
37

Interface Width for Iron
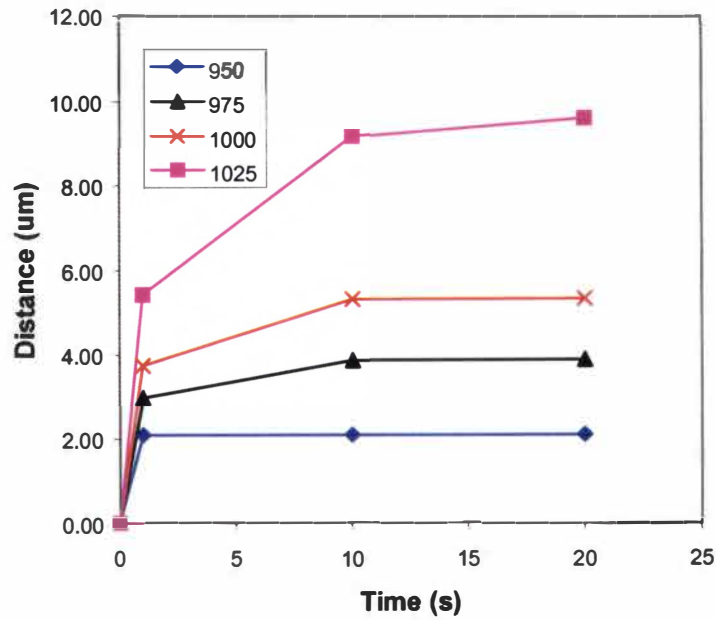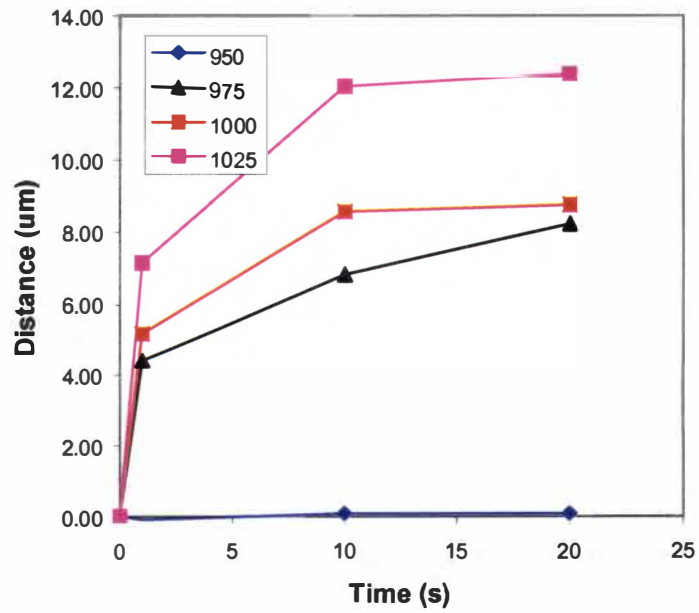

a)

Interface Width for Manganese
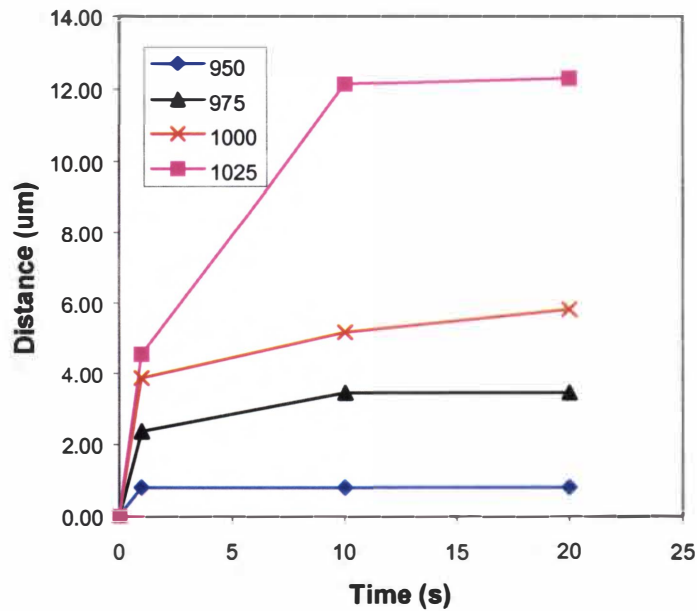
b)

Figure 6 Interface width in microns as calculated using Dictra™ for each of the elements modeled a) iron, b) manganese, c) nickel, and d) phosphorus.
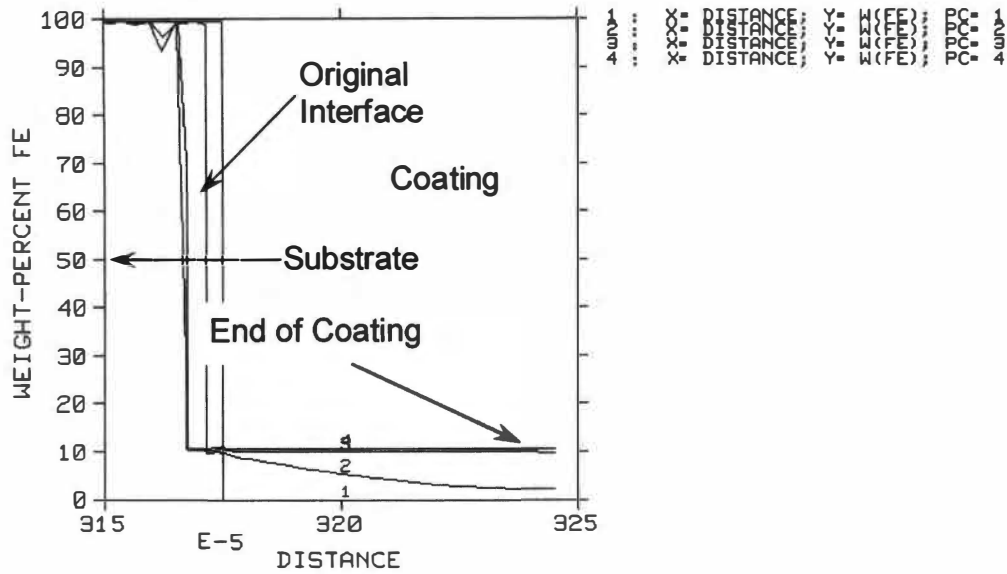
Interface Width for Nickel

c)

Interface Width for Phosphorus

d)

Figure 6 (Continued).
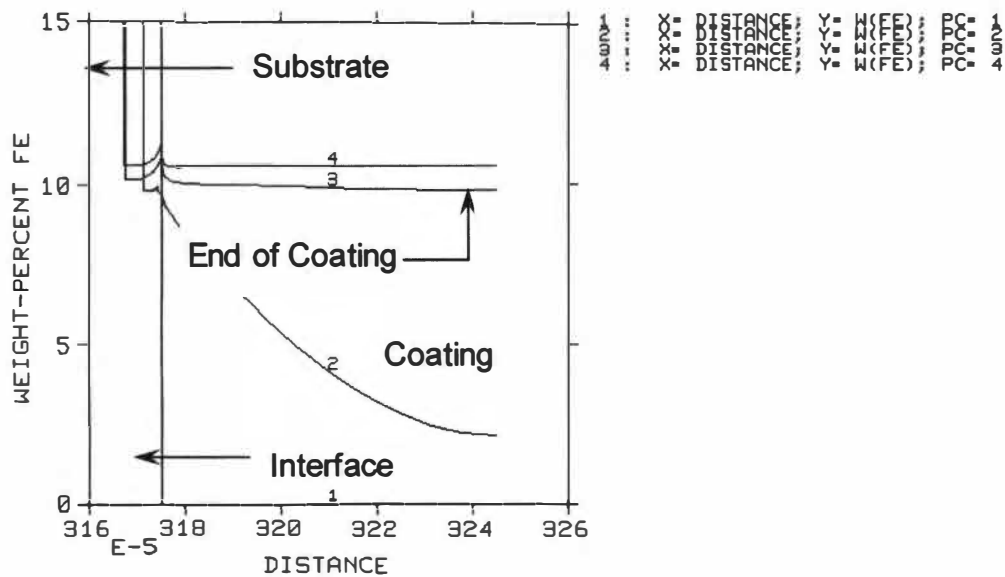
Figure 7 shows the Dictra™ model of the diffusion of iron into the coating (>317.5E-5) at 1025°C for 0, 1, 10, and 20s (curves 1, 2, 3, and 4 respectively) over the composition ranges of a) 0 to 100% iron and b) 0 to 15% Fe. Distance is shown in meters.
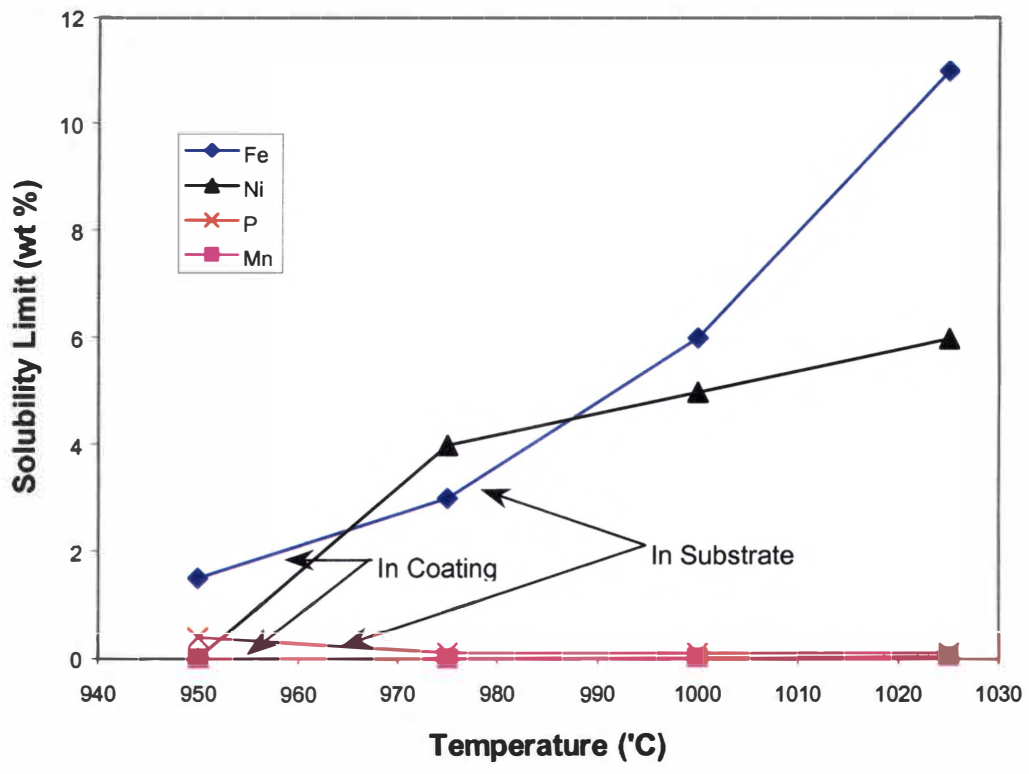
Figure 8 Theoretical solubility limits for iron, nickel, phosphorus and manganese as they diffuse across the interface from their start positions (Fe and Mn in Ni-10P and Ni and P in A570 steel).

can also be seen that the composition gradient generally decreases with increasing time and temperature (Figure 6).

4.2 Thermo-Calc™: Computational Phase Diagram Results

Figure 9 shows the pseudo-binary phase diagram for the Ni-10P / AISI A570 system generated using Thermo-Calc™. One of the first things noticed was the total solubility of the Ni-10P in the A570 at higher temperatures and the similarity between the A570 side of the phase diagram and the low carbon region of the iron-carbon phase diagram. This suggests that at low Ni-10P contents (<20% Ni-10P) the alloy formed at the substrate may behave as a low-alloy steel. Indeed, as the rest of the diagram is examined it is seen that on the iron (steel) rich side of the diagram the alloy does encounter a ferrite to austenite (BCC to FCC) transformation upon heating, while on the Ni-10P side of the diagram, no such transformation is encountered.

Some questions that arise are why is the diagram so complex? And, why are there so many strange shaped regions? The answers to these questions lie in the nature of the diagram itself. The diagram is an equilibrium description of two multi-component alloys where, when all of the possible interactions are taken into account, there may be some complex, multi-element interactions. In fact, considering the complexity of the Ni-P and Fe-P binary phase diagrams (Figure 10 through Figure 12) and the number of phosphides that are formed, it is a wonder that the diagram is not more complex (for instance, it could include a plethora of $(Ni, Fe)_x P_y$ compounds).

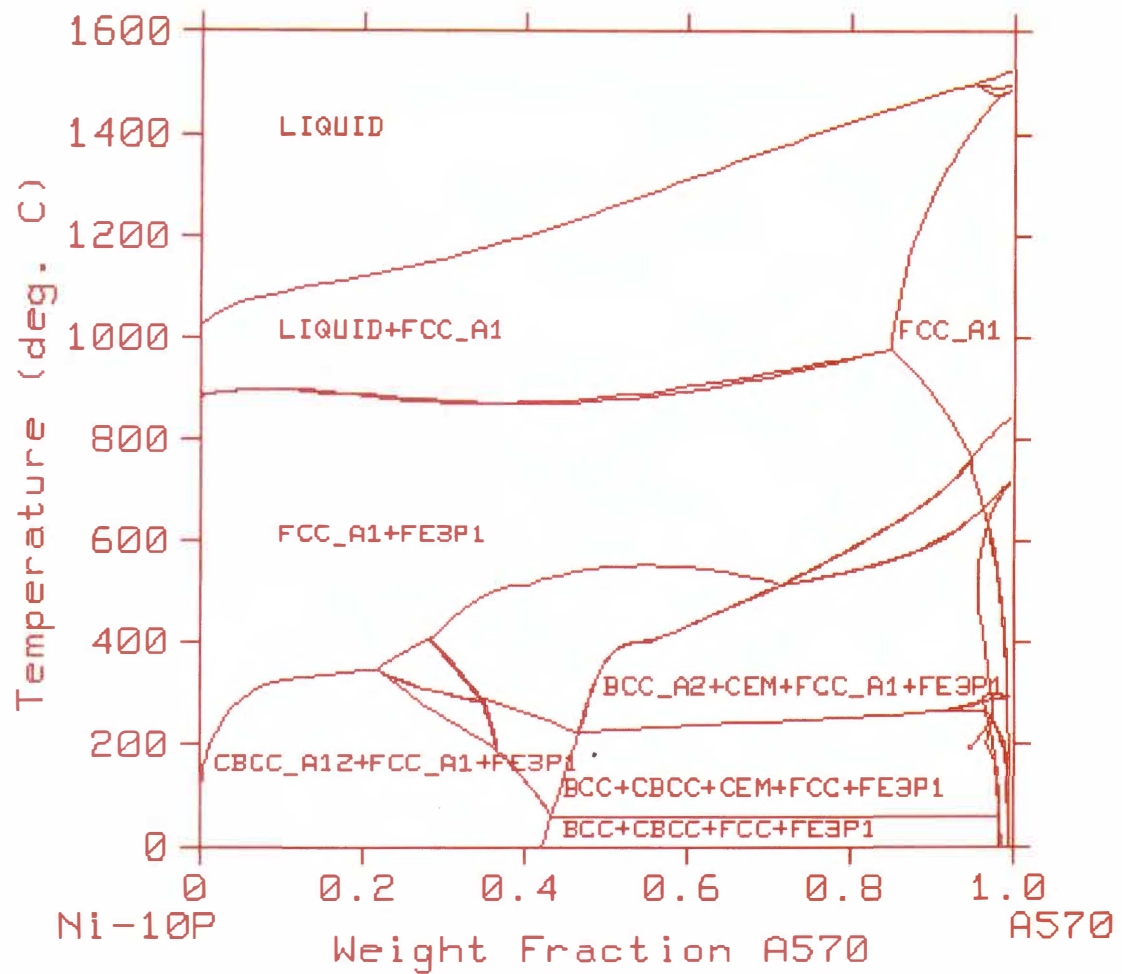**Figure 9** Pseudo-binary phase diagram of the Ni-10P/AISI A570 steel system.

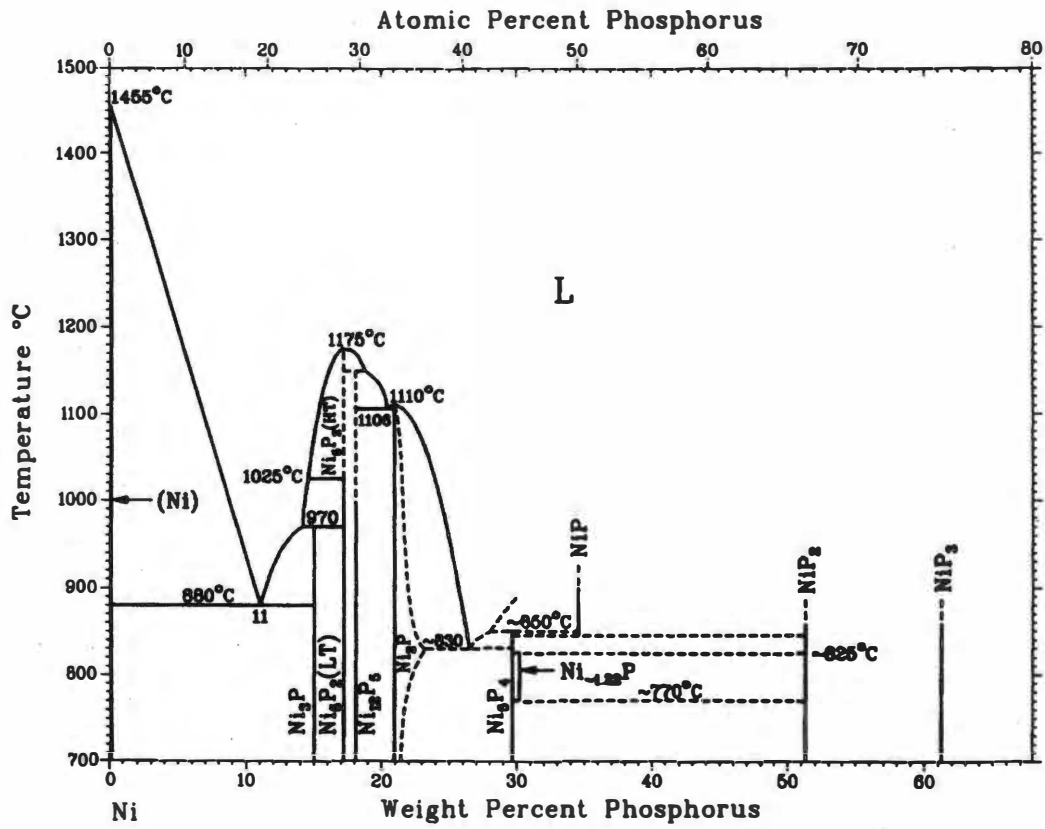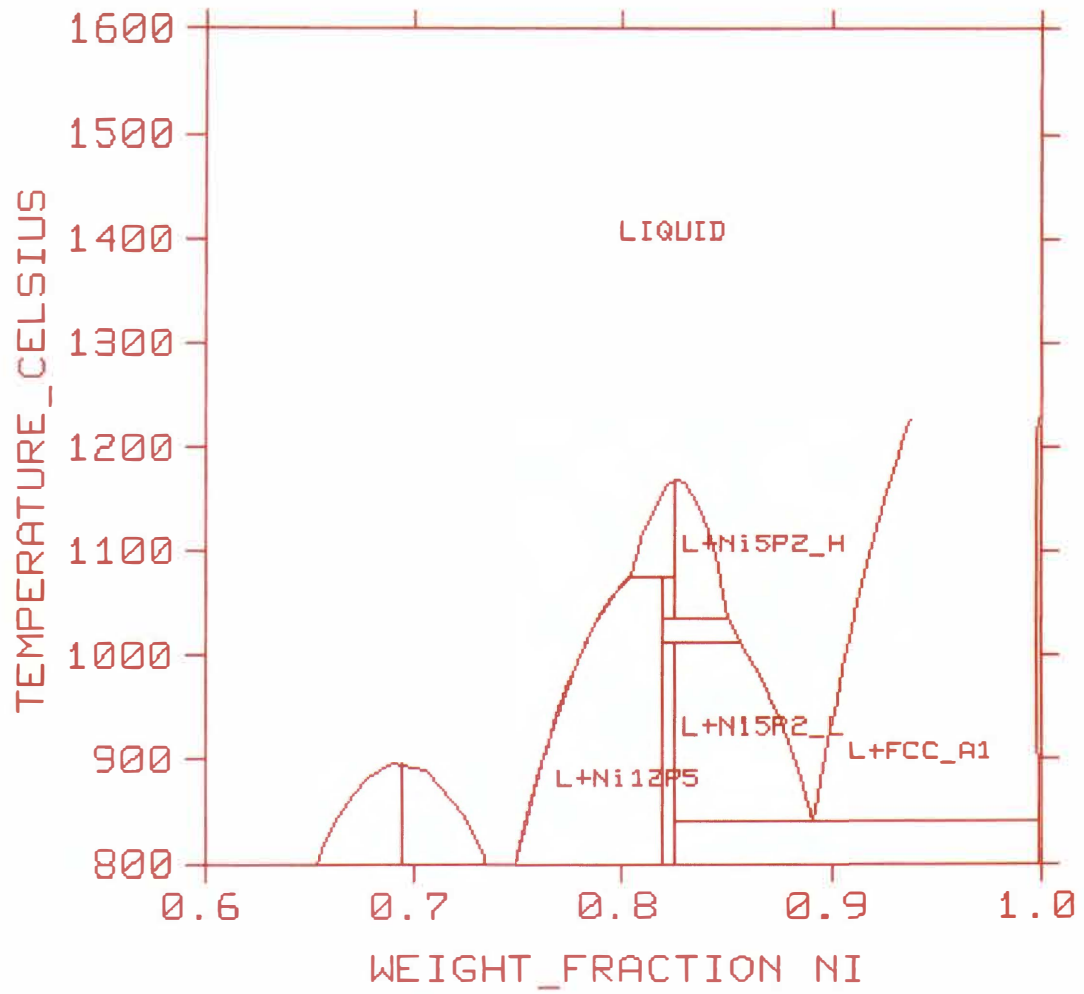**Figure 10** Published version of the Ni-P binary phase diagram[72].

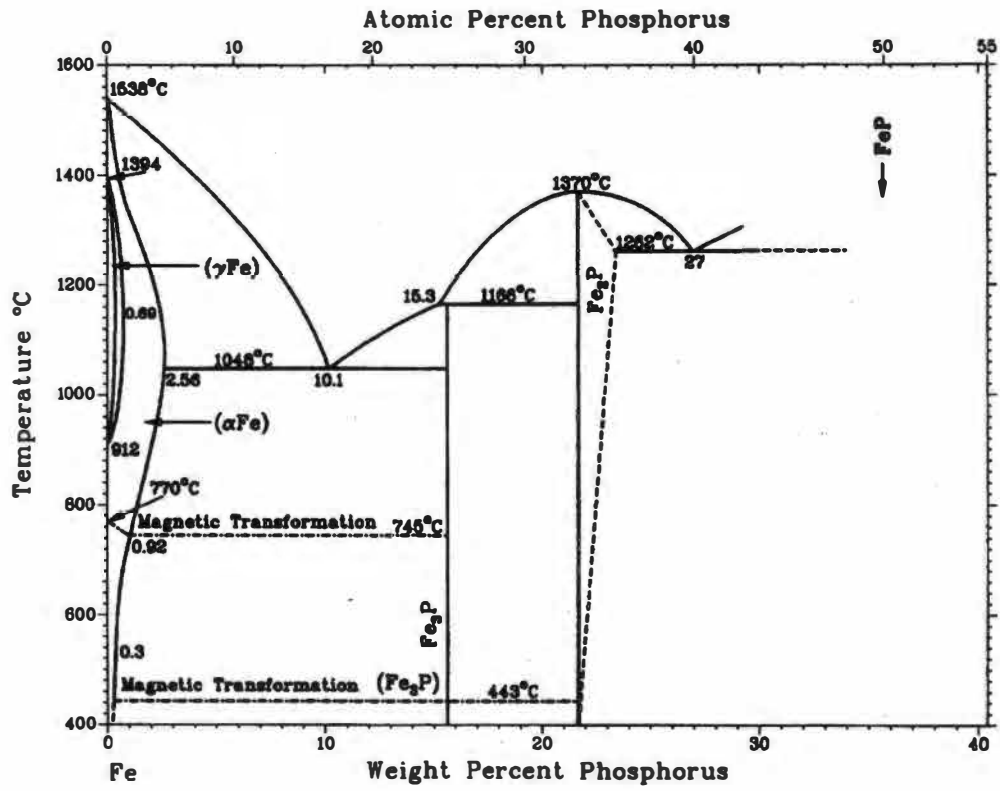**Figure 11** Nickel-phosphorus phase diagram calculated using Thermo-Calc™.

Figure 12 Published version of the iron-phosphorus phase diagram[71].

46

Table 3 Table comparing the published Ni-P phase diagram[72] to the theoretical Ni-P phase diagram computed using Thermo-Calc™.

Phase Diagram Comparison		
	Published	Calculated
Feature	Temperature ('C)	
Ni-P Eutectic	880	840
$L + Ni_5P_2 \rightarrow Ni_3P$	970	1007
$Ni_3P_2(HT) \rightarrow Ni_3P_2(LT)$	1025	1031
$Tm(Ni_5P_2)$	1175	1160
	Weight Percent	
Ni-P Eutectic	11	11
Ni_5P_2	17.2	17.5
$Ni_{12}P_5$	18.2	18

Thermo-Calc™ was also used to plot a binary phase diagram of the Ni-P (Figure 11) to compare to published versions (Figure 10[72]). There are no significant variations between the two, phase diagrams, in the region near the composition of interest (Ni-10 +/- 2 wt % P). There are minor differences in the shape of the curves that can possibly be attributed to small differences in the constants used to calculate the phase diagrams, or more likely due to corrections made to the published phase diagram from experimental data (Table 3).

There are some minor differences between the Ni-P phase diagram calculated using Thermo-Calc™ and the phase diagram published in Binary Phase Diagrams[72]. Some of the discrepancies arise because Thermo-Calc™ does not base calculations on non-stoichiometric compounds (such as $Ni_{1.22}P$), some of which are represented in the published phase diagram (Figure 10[72]). The other differences arise from adjustments that have been made to the published phase diagram resulting from experimental work. These changes reveal the formation of the non-stoichiometric compounds mentioned before as

47

well as the dissimilarities in the formation and dissolution temperatures of Ni-P compounds.

4.3 Combining the Thermo-Calc™ and Dictra™ Models

By examining the Thermo-Calc™ and Dictra™ models together some clues about the microstructure might be revealed. For example, at 950°C and for times greater than 0s, through a range a few microns thick (the width of the interface, as calculated using Dictra™, Figure 6) we would expect a collection of FCC and BCC phases with some Fe_3P, as predicted from the pseudo-binary phase diagram computed using Thermo-Calc™. There is not significant diffusion of nickel or phosphorus into the substrate, so, it is expected that the substrate will, in this case, have a microstructure very similar to an uncoated piece of A570 steel that has a similar thermal history (BCC or BCC with some Fe_3P). As for the coating, it is seen that a large amount of steel would have to diffuse in (>42 wt%) before the coating would begin to have any of the BCC phase present, remaining mostly FCC with some Fe_3P. For the calculations carried out at higher temperatures (975°C, 1000°C, and 1025°C) we see similar trends except that the width of the interface region begins to increase as both time and temperature increase.

By looking at the pseudo-binary phase diagram and the diffusion models together, we can begin to get an idea of the structure that forms during processing. Porter and Easterling[73] state that the diffusion of solute into liquid during solidification of an alloy can be compared to the conduction of latent heat into the liquid during the solidification of a pure metal. Examination of the Ni-10P/AISI A570 pseudo-binary phase diagram

indicates that the liquidus temperature increases with increasing A570, the solute in this case, indicating that as the amount of A570 in solution increases, isothermal solidification will occur. From this we would expect to see constitutional supercooling of the alloy formed at the solid-liquid interface as the specimen is being held at temperature. Due to the method of heating and the geometry of the specimens (radiant heating of a thin coated specimen) the heat flow will be from the coating into the substrate. Provided that the temperature gradient across the interface is less than some critical gradient, a protrusion may form due to the compositional supercooling. Provided that the tip of the protrusion remains below the local liquidus temperature solidification is possible and the protrusion can develop.

Assuming that diffusion occurs laterally as well as normal to the direction of the interfacial plane (Figure 13), as these protrusions develop they may form into columns normal to the planar interface, causing the solute to be rejected laterally and pile up at the root of the protrusion, which in turn causes recesses to form, triggering the formation of
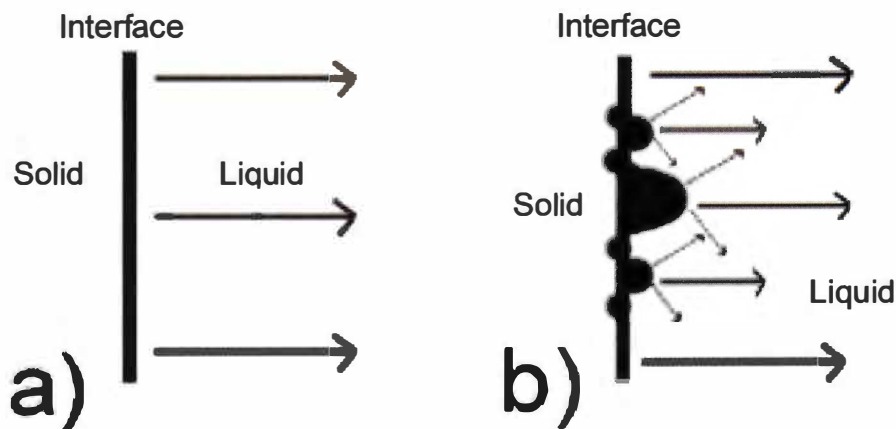

Figure 13 Schematic representation of a) planar and b) combined planar and lateral diffusion.

other protrusions[73]. Or, more specifically, the protrusions form as the substrate dissolves into the liquid coating forming saturated regions, protrusions/columns, that isothermally solidify. As time extends, solid-state diffusion continues homogenizing the protrusions. Homogenization will proceed from the interface region into the alloy and substrate regions. The processing temperature of the specimen determines the composition of these columns. As shown in Figure 8, as the processing temperature increases, the solubility limit of the substrate alloy in the liquid increases. The rate of diffusion also increases with temperature, as is evidenced by the theoretical data of Figure 6, so it is expected that the height of the columns will also increase with temperature. Obviously, diffusion is a time dependent process, so column height will also be expected to increase with time.

Due to the complex nature of the system, this is not the only microstructure that may be formed. Since this is a multi-component system, it is expected that each element will diffuse at a different rate. Also, it is well known that the rate of diffusion in liquids is orders of magnitude greater than the rate of diffusion in solids. So, we would expect to see more of the substrate constituents dissolved into the liquid coating (Figure 6). Additionally, we would expect the substrate constituents to be distributed more homogeneously throughout the coating. This could result in coring upon cooling. As the temperature decreases those portions of the melt with higher melting temperatures, which may consist of a single element, compounds (simple, or complex), or alloys of different types (eutectic, or peritectic for example), will solidify first, forming a small solid nuclei, barring the effects of recalescence or undercooling. As the specimen continues to cool,

50

successive layers of solid are deposited with each successive layer having a little bit more of the lower melting point components[74]. As these cores thicken, some solute is rejected into the remaining liquid forming columns in a similar fashion to that mentioned previously[73]. This time the direction of the column formation would be normal to the core. As these columns form, they too will reject some solute into the remaining liquid, resulting in still more columns growing perpendicular to their direction of growth. The final result is the treelike dendritic structure (Figure 14)[74]. The remaining liquid is expected to cool forming a microstructure that is consistent with eutectic solidification[73]. It should be recalled that these microstructures are consistent with equilibrium conditions; since the cooling time is finite, we expect some supercooling to occur resulting in the formation of some non-equilibrium microstructures. Furthermore, it is well known that phosphorus tends to be found in higher concentrations along grain boundaries forming cells upon solidification[52,69]. From the results of the Dictra™ model (Appendix B) it is seen that the phosphorus is not expected to diffuse more than a few microns into the substrate, but we also expect diffusion to be enhanced along grain boundaries[75]. So, most of the phosphorus would be expected in the coating and in the grain boundaries in the interface region, but some phosphorus would also be expected along the grain boundaries in the substrate, near the interface region.
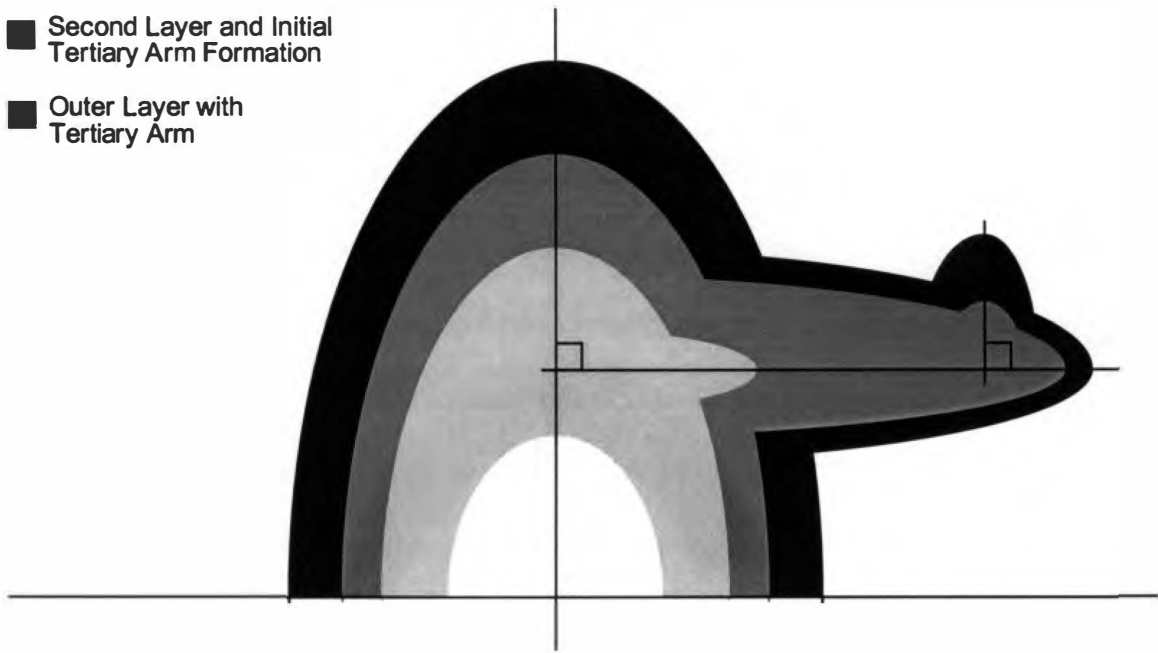
Figure 14 Schematic representation of dendritic growth and formation of the treelike dendritic structure. The melting point of each successive layer is lower than that of the previous with the core composition having the highest melting point.

4.4 Experimental Results

4.4.1 Coating Compositions

After performing the diffusion and phase modeling for the system, experiments were performed to test the accuracy of the Thermo-Calc™ and Dictra™ predictions for this system. Since the coating alloy was manufactured in-house, the first step was to determine the composition of the alloy to insure that it was of the same composition as the coating alloy that was modeled. Also, in order to see how the alloy would wet and flow on a piece of the A570 steel, it was determined that using a melting point test would be the most useful method to use.

Figure 4 shows one of the heating curves obtained from the test. From the heating curve the melting point of the alloy is easily determined. This temperature can then be marked as a horizontal line on the Ni-P binary phase diagram. Because the approximate alloy composition from the manufacturing process is already known, this information can be used to make a more accurate alloy composition determination by drawing a vertical line on the phase diagram from the point where the temperature line crosses the phase diagram nearest the estimated composition (Figure 15). This test was performed twice to insure accuracy. From both tests the alloy melting point was found to be 890°C which corresponds to an alloy composition of Ni-10.1 wt % P which is an error of only 1% from the composition used for modeling and so should provide a reasonable comparison to the theoretical models.
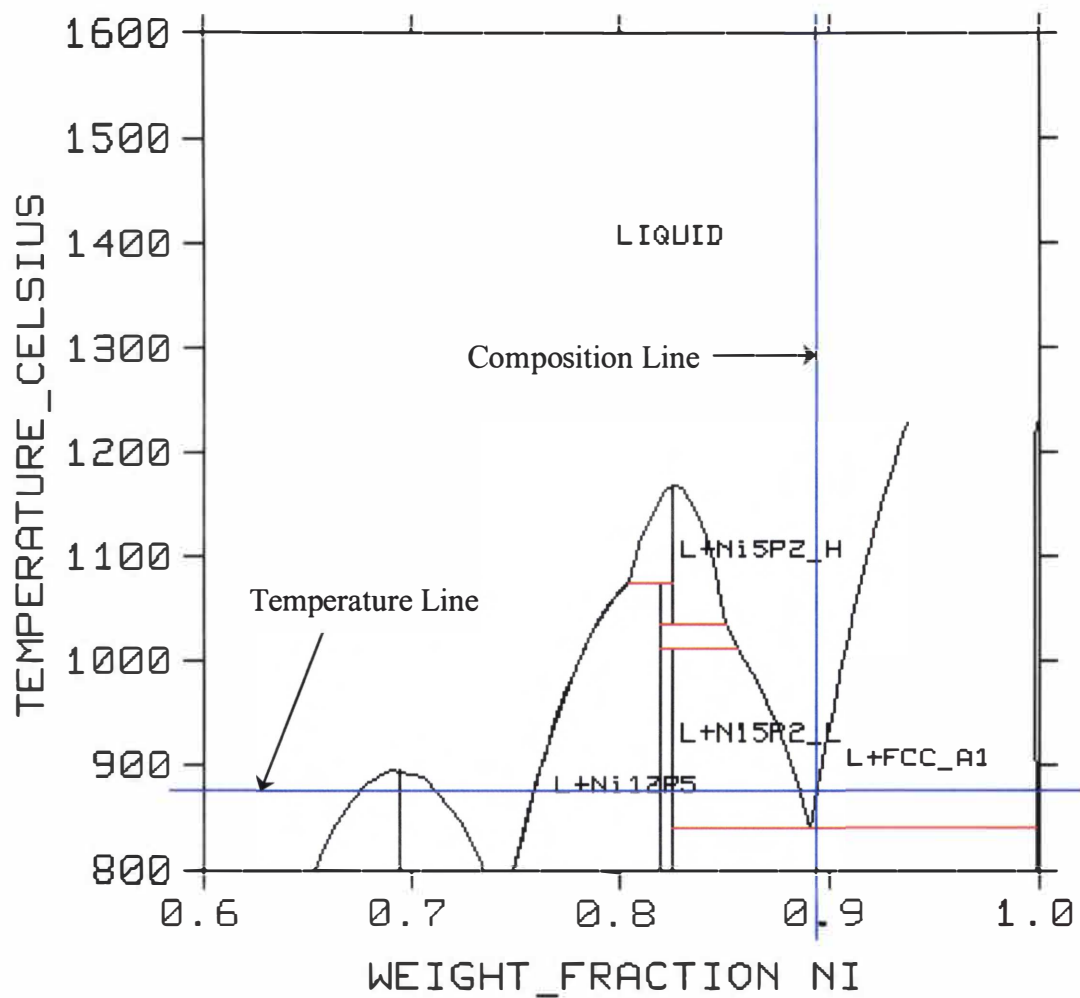
Figure 15 Schematic representation of coating composition determination from melting point data.

From the tests, it was also found that the Ni-10P alloy wets the AISI A570 steel well but did not flow evenly over the surface of the A570. Wetting was determined by visual inspection of the wetting angle where the lower wetting angle would correspond to better wetting (Figure 16)[76]. Although no actual measurements were made, visual inspection did reveal a low wetting angle. Also revealed by visual inspection was the fact that the alloy did not flow evenly over the surface of the A570 coupon. This is most likely due to a high surface tension, restricting the flow of the Ni-10P. These results mean that we can expect to see an interfacial reaction between the alloy and the substrate. In order to make sure that a large enough surface area of the surface of the coupon is covered with a uniform thickness (70μm-100μm) of coating, to compare to the theoretical results, the alloy is going to have to be spread evenly over the surface of the A570 coupon prior to processing. On the other hand, no special precautions need to be made to make sure the alloy doesn't run off of the coupon.
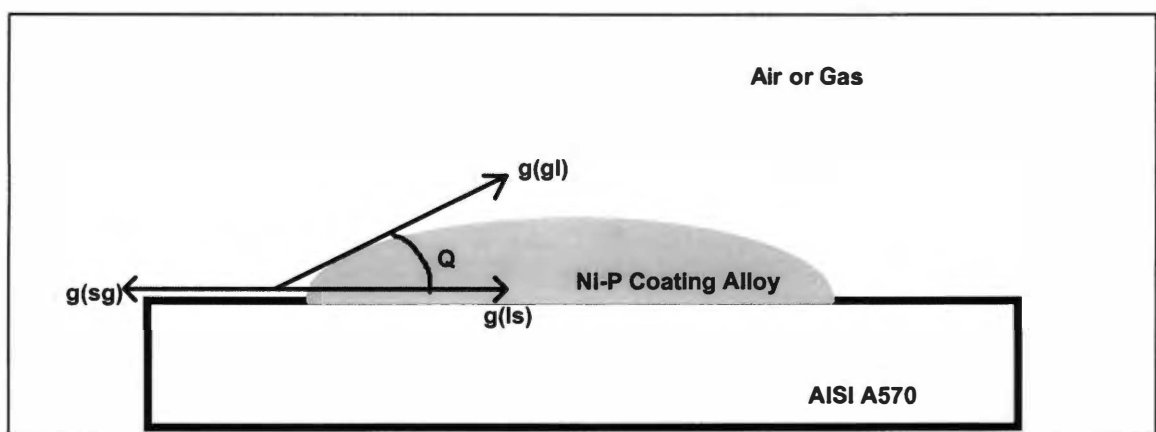

Figure 16 Representation of the wetting angle for Ni-10P on AISI A570 steel; θ is the wetting angle, g(ls), g(gl), and g(sg) are the free energies of the liquid/solid, gas/liquid and solid/gas interfaces respectively.

4.4.2 Coating Density

Once the alloy was determined to be the correct composition, it was necessary to determine the mass of alloy that would be necessary to produce a coating of uniform thickness (70μm-100μm) on one of the A570 steel coupons. Archimedes method for determining density was used with methanol as the displaced fluid. The density of the Ni-10P alloy was determined to be 7.16g/cm^3, which is very close to the theoretical density value obtained using the rule of mixture. From this information, and by calculating the volume of coating needed to cover a coupon with a layer of coating from 70μm-100μm thick the mass of the coating required for each coupon was determined to be from 1.30g to 1.86g.

The mass of coating alloy used for each trial is shown in Table 2. The heating and cooling curves were used mainly to insure the uniformity of the heating cycle from sample to sample. With the exceptions that only one channel was recorded and that time and temperature were varied for each sample, the heating curves are very similar to those found in Figure 4.

4.4.3 Optical Microscopy

Figure 17 shows an unetched view of the cross-section of the coupon processed at 975°C for 0s. It is crucial in understanding the system to realize that the process times do not include the time to temperature, or the cooling time. It is easily seen that there were some columns that formed at the interface. Also apparent in this figure is that there is some dendritic formation in the coating. Examination of all of the specimens revealed a
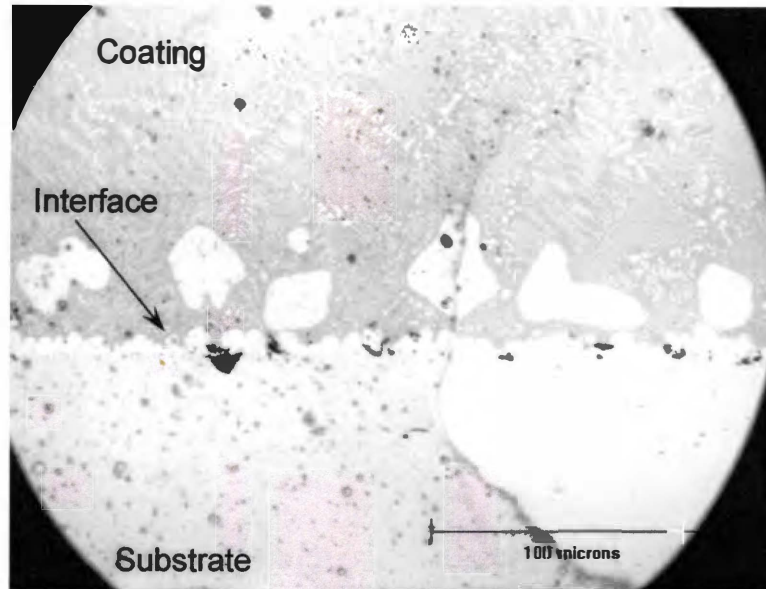
Figure 17 Optical micrograph of an unetched specimen processed at 975°C and a processing time of 0s. The column formation and dendrite cores are already visible.

similar microstructure for all processing times and temperatures. The major differences that were noted was that the column "height" appeared to increase with time and temperature and dendritic formation and complexity increased with time and temperature. Figure 18 and Figure 19 show how the column height (averaged over 20 columns for each condition) changes with time and temperature respectively. From these it can be seen that column height increases with increasing temperature and does not vary uniformly with processing time. This is to be expected as it has already been shown that solubility increases with temperature, thus a greater amount of solute is present prior to isothermal solidification occurring. The end result is longer columns at higher temperatures.

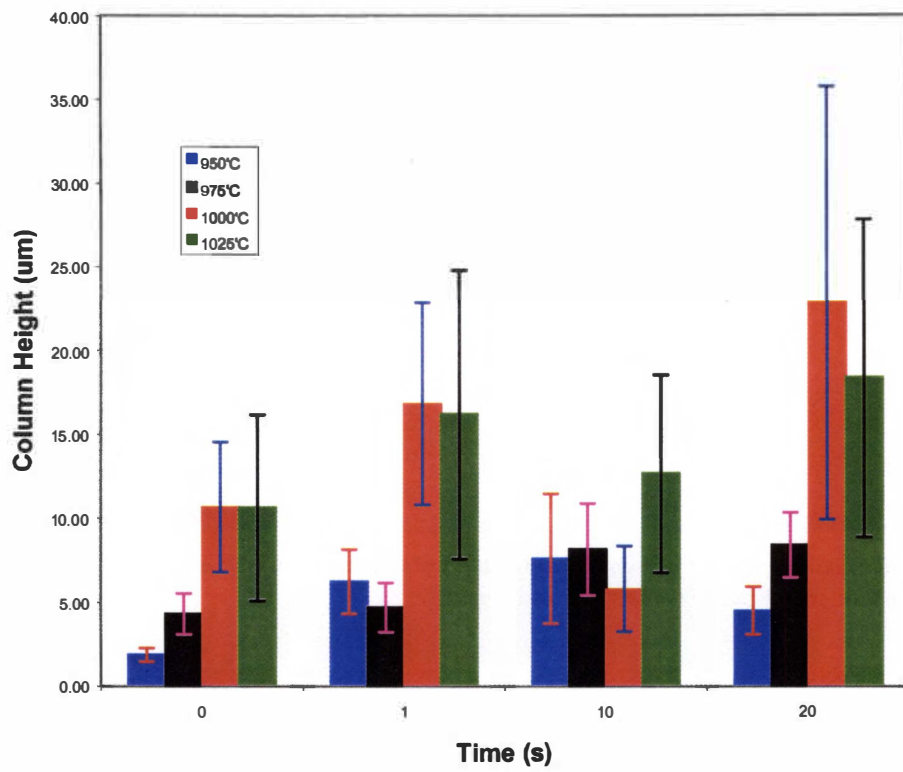Since it is difficult to quantify dendritic properties without doing extensive work, the

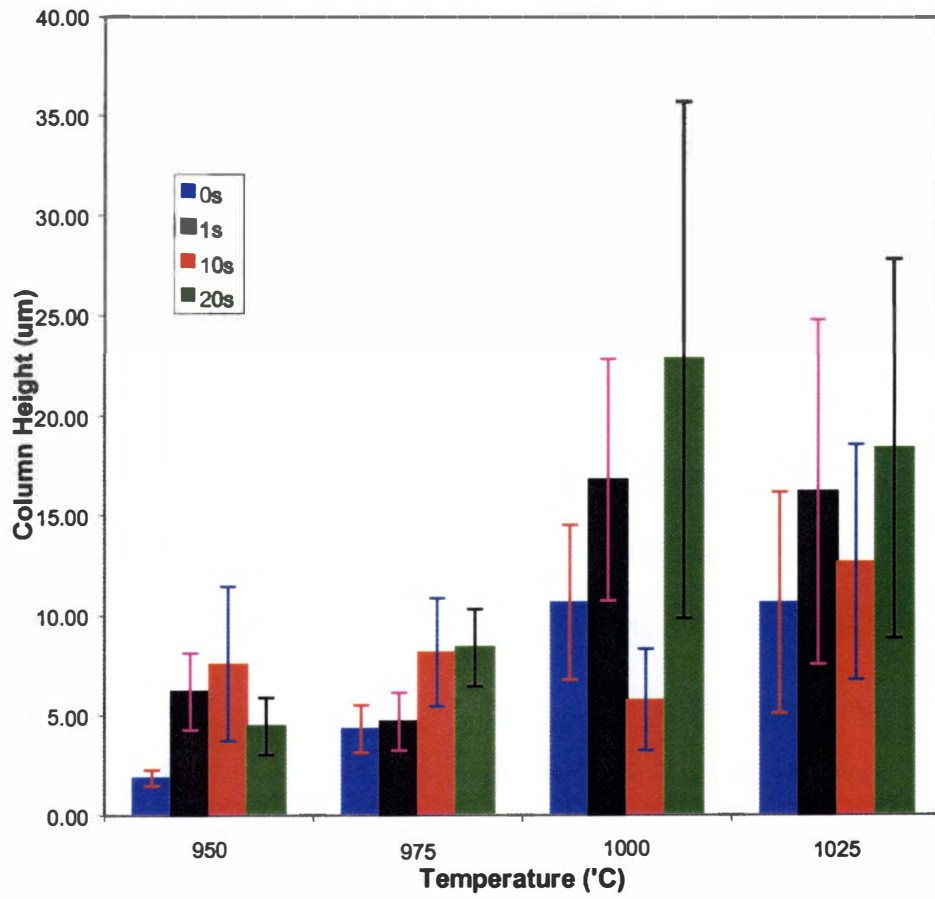**Figure 18** Graph of average column height versus time.

Figure 19 Graph of average column height vs. temperature.

dendritic qualities will be discussed briefly here. At 950°C and 0s there weren't any dendrites formed; as the processing time increased several nuclei began to form and grow, but none of the nuclei developed primary arms. At 975°C and 0s there were already some dendritic nuclei present (Figure 17). As time increased the nuclei became unstable and formed primary arms by 20s. Primary dendritic arms are visible in the specimen processed at 1000°C for 0s and secondary dendritic arms are beginning to form by 10s. The dendrites continue to grow through 20s. Very thick primary dendritic arms are present in the specimen processed at 1025°C for 0s. At 1s the dendrites are already forming secondary arms and at 10s the dendrites are continuing to thicken and grow, in a few cases tertiary dendritic arms can be seen as they begin to form. Finally the specimen processed for 20s shows a complex structure where some of the primary and secondary arms are beginning to "pinch" off from each other.

Even more detail was revealed in the microstructure after etching the specimens with a 1:4 nitric acid/acetic acid mixture. The first thing that was apparent was the microstructure of the substrate. Etching revealed a coarse hypoeutectic pearlitic steel microstructure in all cases. Etching also revealed a fine microstructure in the coating. An optical micrograph of the etched specimen processed at 975°C for 0s can be seen in Figure 20. At first glance the microstructure appears to be a combination of the spheroidal and plate-like eutectic forms. It is strongly suspected that the fine microstructure is the acicular eutectic type where the needle-like regions are being seen from different angles for each of the different grains. What is also seen at this point is
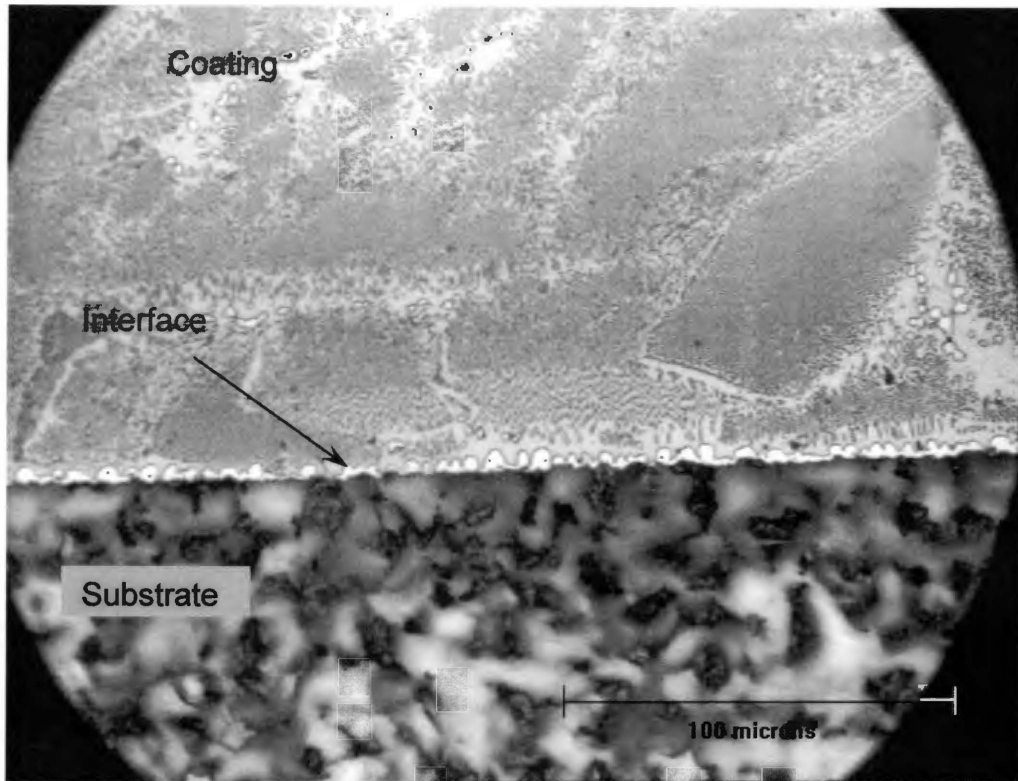
Figure 20 Optical micrograph of an etched specimen processed at 975°C and a processing time of 0s. The column formation and dendrite cores are already visible.

that the dendrites that have formed on the grain boundaries and that there are regions surrounding the dendrites that are absent of the fine microstructure, the fine microstructure occurring only within the grains. This suggests a hypoeutectic alloy as described by Rhines[74]. At this point we can only speculate as to what the structure is, because this is a complex system of elements. Further work to determine the composition of the dendrites, eutectic rods, columns, and the matrix needs to be done in order to further classify the system.

4.4.4 Microprobe Analysis

Microprobe analysis was performed to further classify the microstructure of the specimens and to determine the amount of co-diffusion between the coating and the substrate. Electron images were taken of each specimen (Figure 21 to Figure 24) and elemental line scans and X-ray maps were performed to determine the quantities and distributions for Fe, Ni, and P, disregarding Mn because it was present in such minor quantities (0.45 wt%).

Figure 25 shows a composite (secondary electron and back-scattered electron) image of the cross-section of the specimen processed at 975°C for 0s. The similarity between this image and the optical images is immediately apparent; the dendritic nuclei seen in the unetched specimens are easily seen as well as the finer microstructure apparent in the etched specimens. In fact, the microstructure is more easily viewed due to the higher magnification capabilities of the electron microprobe.

The biggest differences that arise are discrepancies between the data obtained from the microprobe line scans and the theoretical data from the model. Both the model and the experimental data show trends towards a solubility limit for iron in the coating and for nickel and phosphorus in the substrate; unfortunately the theoretical and experimental solubility limits are not in agreement. This can be explained by recalling that the Dictra™ model does not take lateral diffusion into account and by recognizing that the dendrites and columns are going to contain greater amounts of higher melting point
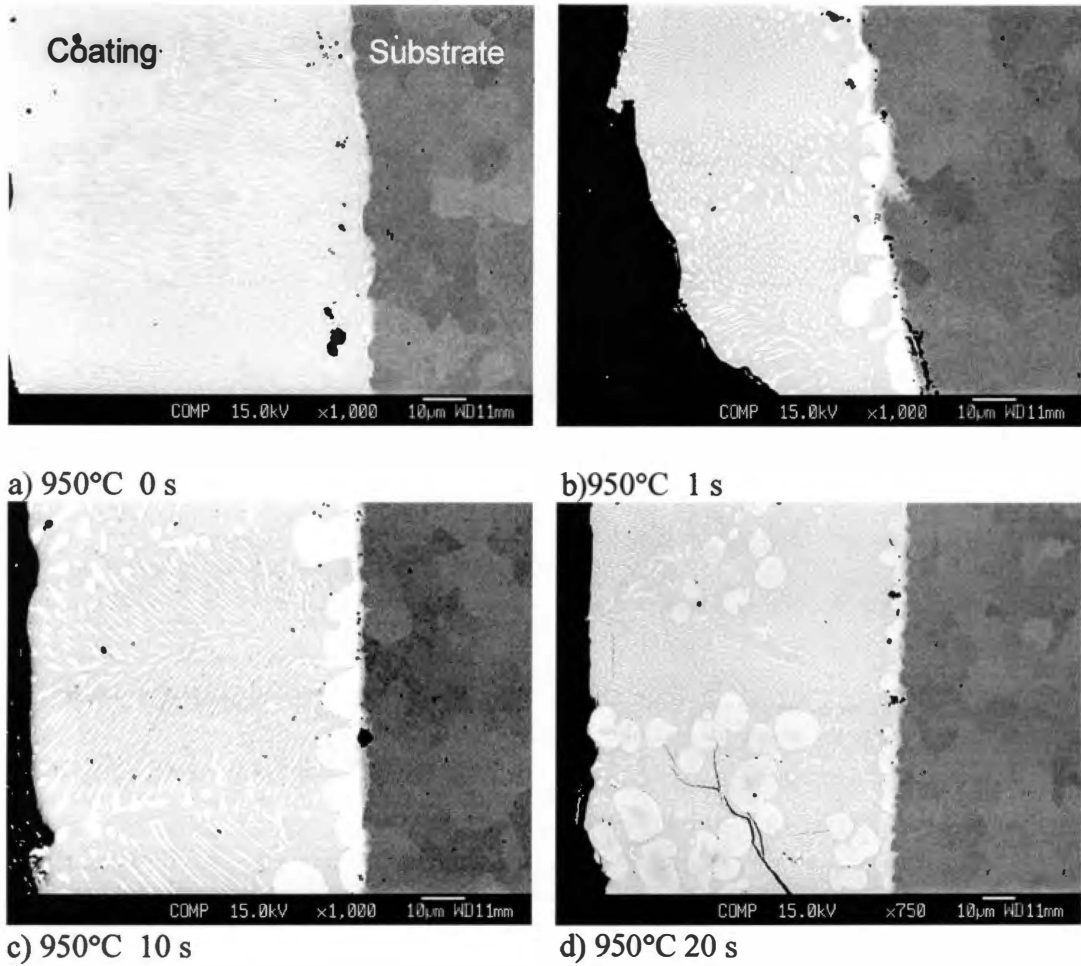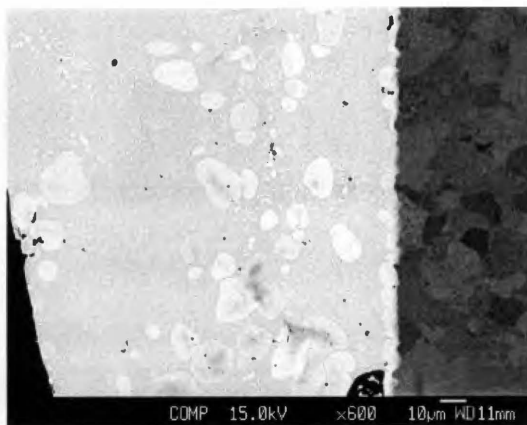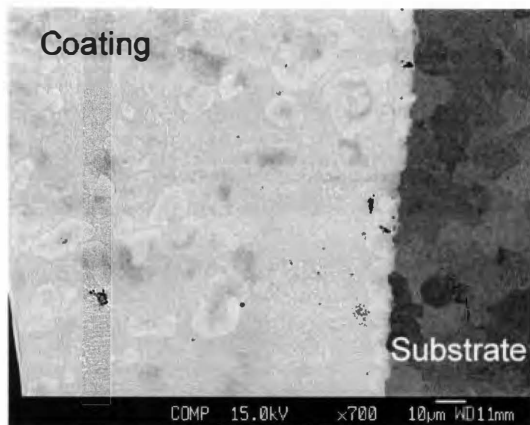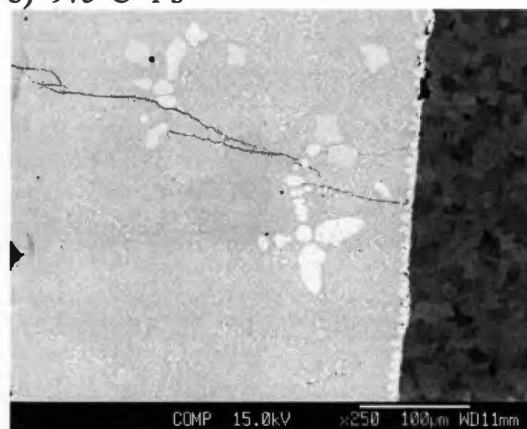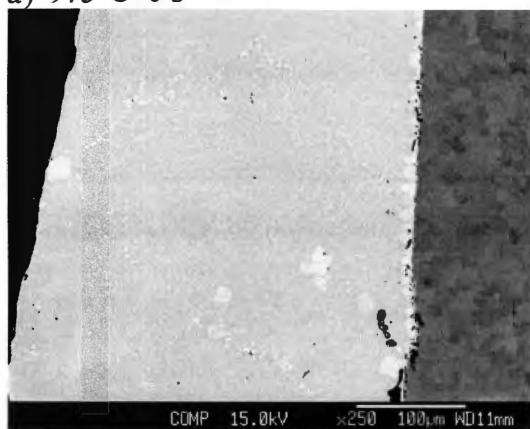
Figure 21 Microprobe electron cross-sectional images for specimens processed at 950°C, a) 0 s, b) 1 s, c) 10 s, d) 20 s.

a) 975°C 0 s b) 975°C 1 s

c) 975°C 10 s d) 975°C 20 s

Figure 22 Microprobe electron cross-sectional images for specimens processed at 975°C, a) 0 s, b) 1 s, c) 10 s, d) 20 s.
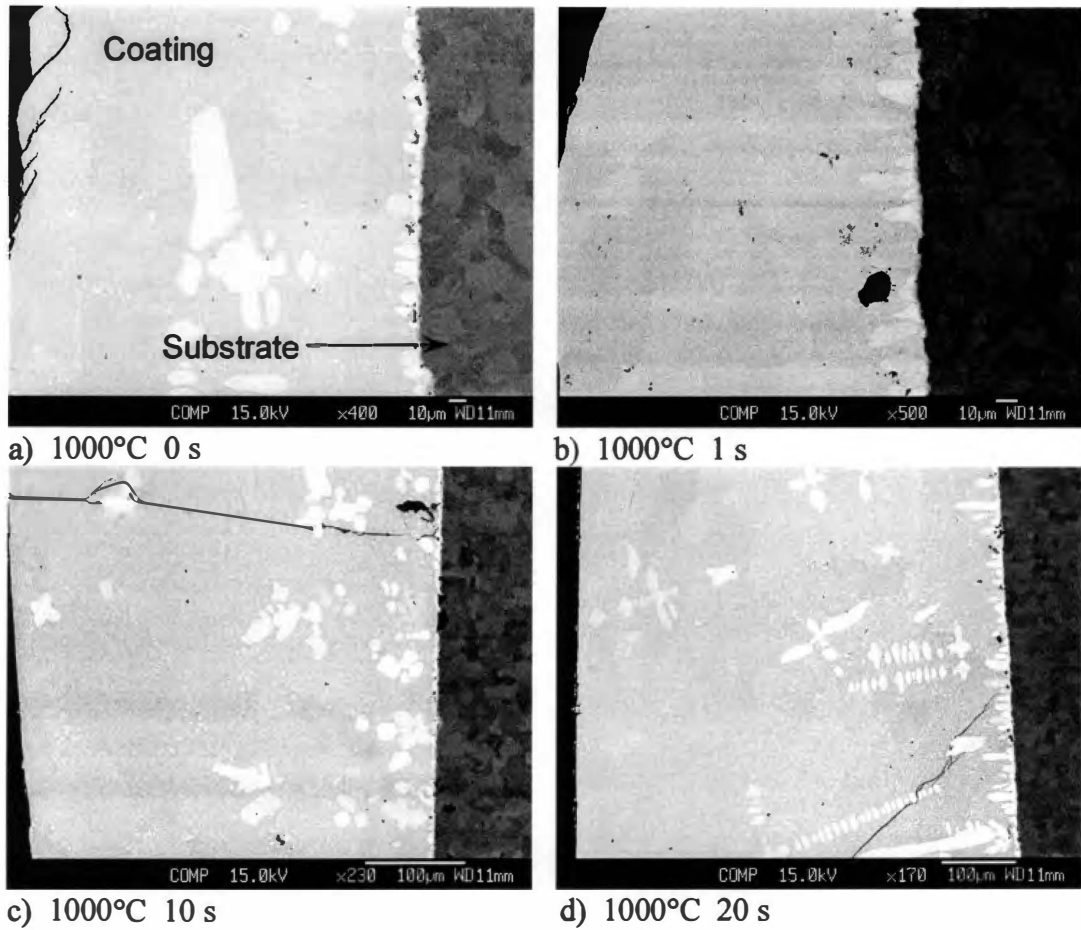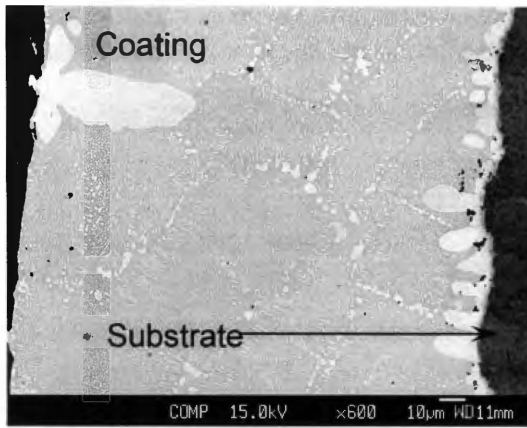
a) 1000°C 0 s   b) 1000°C 1 s

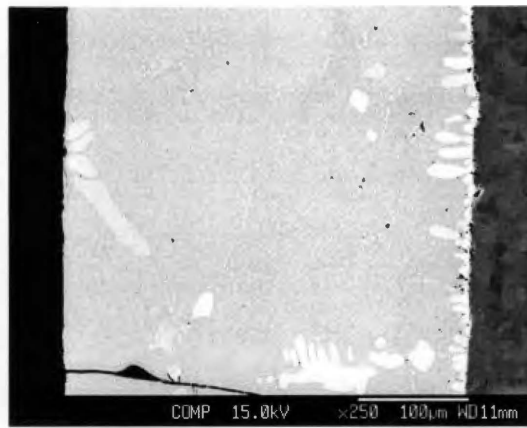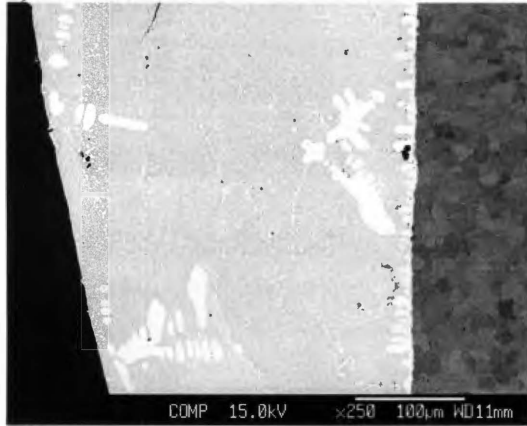c) 1000°C 10 s   d) 1000°C 20 s

Figure 23 Microprobe electron cross-sectional images for specimens processed at 1000°C, a) 0 s, b) 1 s, c) 10 s, d) 20 s.

a) 1025°C 0 s

b) 1025°C 1 s

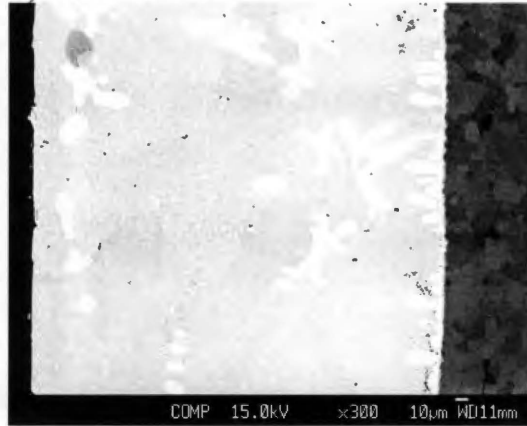c) 1025°C 10 s

d) 1025°C 20 s

Figure 24 Microprobe electron cross-sectional images for specimens processed at 1025°C, a) 0 s, b) 1 s, c) 10 s, d) 20 s.
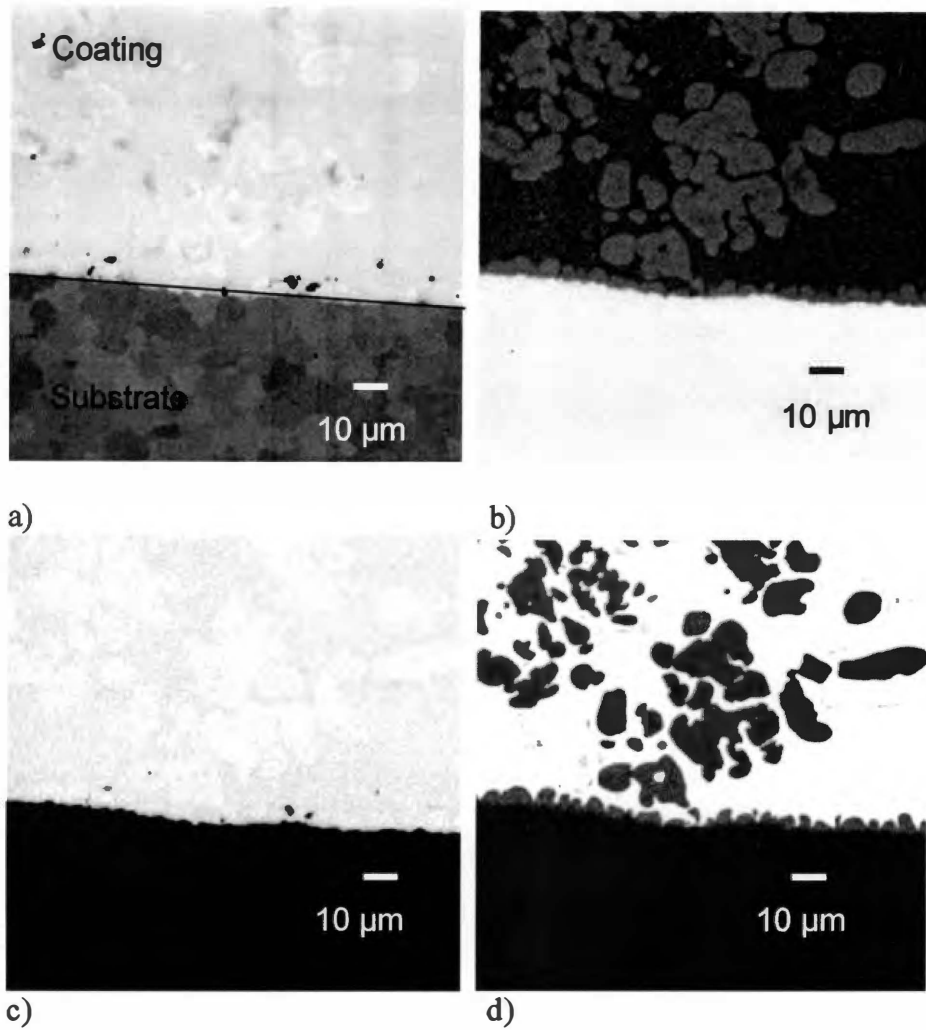
Figure 25 Electron micrograph of an etched specimen processed at 975°C and a processing time of 0s showing a) composite image (secondary and backscattered electron image), b) X-ray map of Fe, c) X-ray map of Ni, and d) X-ray map of P.

components. Examination of the Ni-P, Fe-P and Fe-Ni binary phase diagrams suggest that the nuclei (columnar, eutectic and dendritic) may be an iron-nickel alloy, an iron-phosphorus, or a nickel-phosphorus compound. Again, we must remember that this is a complex, multicomponent system and that it is possible that the nuclei are formed from a complex, high melting point compound or possibly from pure iron or nickel. The theoretical pseudo-binary phase diagram suggests that the nuclei are formed from a ferritic core that develops a layer of Fe_3P on cooling and resides in a ferritic matrix with some retained austenite.

Examination of the X-ray maps (Figure 25 c, d and e) reveals increased amounts of iron in the cores and nuclei as well as higher amounts of nickel and significantly reduced amounts of phosphorus. Immediately surrounding the cores and nuclei are layers with less iron and significantly less nickel, but with slightly higher amounts of phosphorus. This suggests that the conclusions drawn from examination of the pseudo-binary phase diagram may be correct, although further evidence is still necessary.

By ignoring the general trends and by closely examining the X-ray line scans in the areas where the dendrites are, we can gain an even better understanding of the system. Initial examination reveals regions in the coating, corresponding to the dendrite in nuclei locations that are higher in nickel and iron and significantly lower in phosphorus. Closer examination reveals that the amount of iron decreases slightly from its level in the dendrites, in the regions immediately surrounding the dendrites and columns, while the amount of nickel remains at about the same level and the amount of phosphorus increases

slightly. There are some interesting things that happen if we examine the trends as time and temperature change. For example, as the time and temperature increase, the amount of iron in the dendrites decreases, the amount of nickel in the dendrites increases and the amount of phosphorus in the dendritic regions decreases slightly with time and remains fairly consistent with temperature. These trends support what was stated earlier regarding the pseudo-binary phase diagram. Higher levels of iron and nickel in the dendritic cores indicate that the iron and nickel are probably freezing out first as pure metals. Examination of the phase diagrams indicates that it would only take a small amount of phosphorus diffusing away, even at higher temperatures, for cores to start forming. Some interesting observations are made when the weight ratios of Fe-Ni, Fe-P, and Ni-P from the microprobe analysis are compared with the atomic weight ratios for common compounds formed by these elements (Table 4). For instance, the ratios corresponding to Ni_5P_2, Ni_3P, and NiP show up consistently in the coating; the ratios corresponding to $Ni_{12}P_5$, $Ni_{1.22}P$ and Ni_3P show up in the substrate and $FeNi_3$ appears in the interface region. There is not enough data to make any conclusions as to the distribution of these compounds.

4.4.5 Comparison of Models to Experimental Data and Conclusions

Finally, the experimental results can be compared to the results from the modeling. The computational results were used to determine the width of the interface by summing the average diffusion depth for iron and manganese with the average diffusion depth for nickel and phosphorus,

Table 4 Presence of some common Fe, Ni, and P compounds based on ±3% variance from the theoretical atomic weight ratio.

Specimen #	Temperature	Time	Compound															
			Iron-Phosphorus				Nickel-Phosphorus									Iron-Nickel		
			Fe_3P	Fe_2P	FeP	FeP_2	Ni_3P	Ni_5P_2	$Ni_{12}P_5$	Ni_2P	Ni_5P_4	$Ni_{1.22}P$	NiP	NiP_2	NiP_3	Fe_3Ni	$FeNi$	$FeNi_3$
Theoretical Atomic Weight Ratio→			5.41	3.61	1.8	0.9	5.68	4.74	4.55	3.79	2.37	2.31	1.9	0.95	0.63	2.85	0.95	0.32
1	950	0	S	--	--	--	I	S	S	S	S	S	--	--	--	I	--	I
2		1	--	S	--	--	C	--	--	--	--	--	--	--	--	--	--	I
3		10	S	S	--	--	S	--	--	--	S	S	S	--	--	--	--	--
4		20	S	S	S	--	C,S	S	S	--	--	S	--	--	--	--	--	--
5	975	0	S	--	--	--	--	--	--	S	S	S	--	--	--	--	--	--
6		1	--	--	S	--	C,S	S	S	--	--	--	S	--	--	--	--	--
7		10	S	--	S	--	C,S	S	S	S	S	S	S	S	--	--	--	--
8		20	S	--	S	--	C	S	S	S	S	S	S	--	S	--	--	--
9	1000	0	S	S	--	--	C,S	S	--	S	S	--	--	--	--	--	--	--
10		1	--	S	S	--	C	S	--	S	S	S	--	--	--	--	--	--
11		10	--	S	--	S	C,I	S	--	S	S	S	S	--	--	--	--	--
12		20	S	S	S	--	C	S	S	S	--	--	S	--	--	--	--	--
13	1025	0	--	--	--	--	C	--	--	--	--	--	--	--	--	--	--	--
14		1	--	--	--	--	S	S	--	--	--	--	--	--	--	--	I	--
15		10	S	--	--	--	C,S	--	--	--	S	--	--	--	--	--	--	--
16		20	S	S	S	--	C,S	S	S	S	S	S	S	--	--	--	--	--
C=Coating					I=Interface				S=Substrate					-- =Not Seen				

$$\frac{iron\_diffusion + manganese\_diffusion}{2} + \frac{nickel\_diffusion + phosphorus\_diffusion}{2} = \text{int}erface\_width$$

(Figure 26). This method was used because the theoretical results showed that the diffusion depth for Fe and Mn into the coating were similar to each other, likewise the diffusion depth for Ni and P into the substrate were similar to each other. From this, it is seen that the interface advances further into the substrate as the temperature and time increase (Figure 27). These results can then be compared with the average column height as measured from the experimental data (Figure 28). So, in general, the computational and experimental results both agree that the interface width increases with temperature.

As stated before, the shape of the diffusion plots for iron indicate that the amount of iron in the coating is probably diffusion rate controlled. From the experimental work, the existence of the columns, and the high presence of iron in the columns, indicates that diffusion of iron into the coating is rate limited. However, the presence of iron throughout the coating is an indicator that diffusion may not be happening by a single mechanism.

As stated before, the shape of the diffusion plots for iron indicate that the amount of iron in the coating is probably diffusion rate controlled. From the experimental work, the existence of the columns, and the high presence of iron in the columns, indicates that diffusion of iron into the coating is rate limited. However, the presence of iron throughout the coating is an indicator that diffusion may not be happening by a single mechanism.
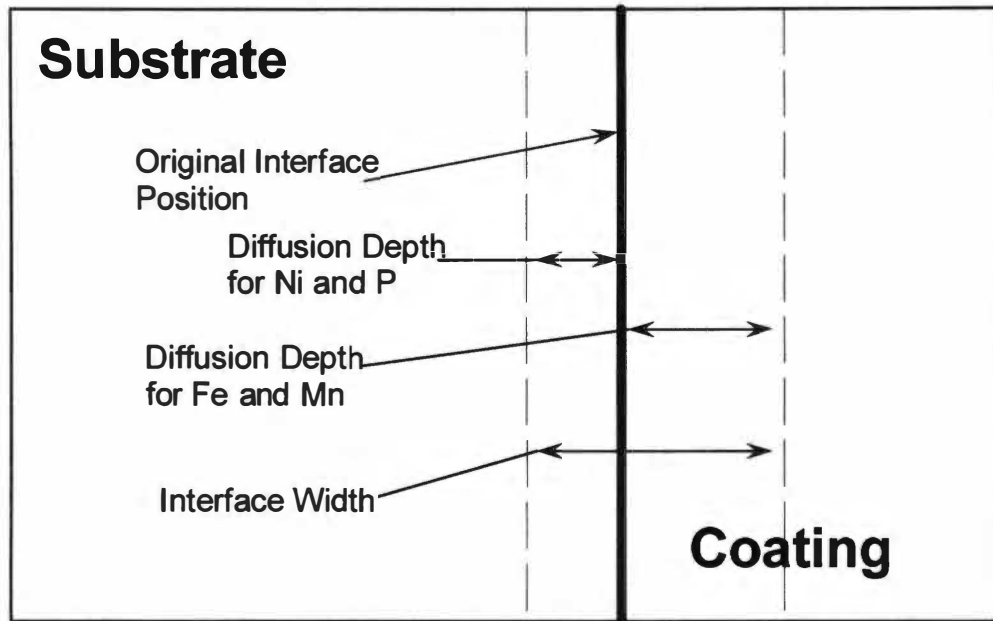
Figure 26 Schematic representation for measuring the interface width as a function of time and temperature.
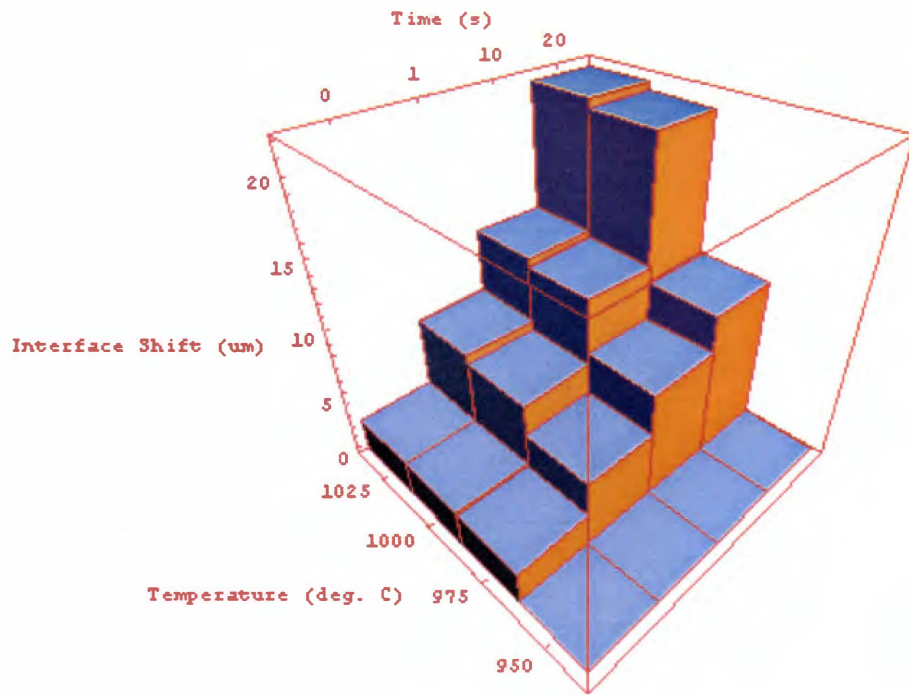
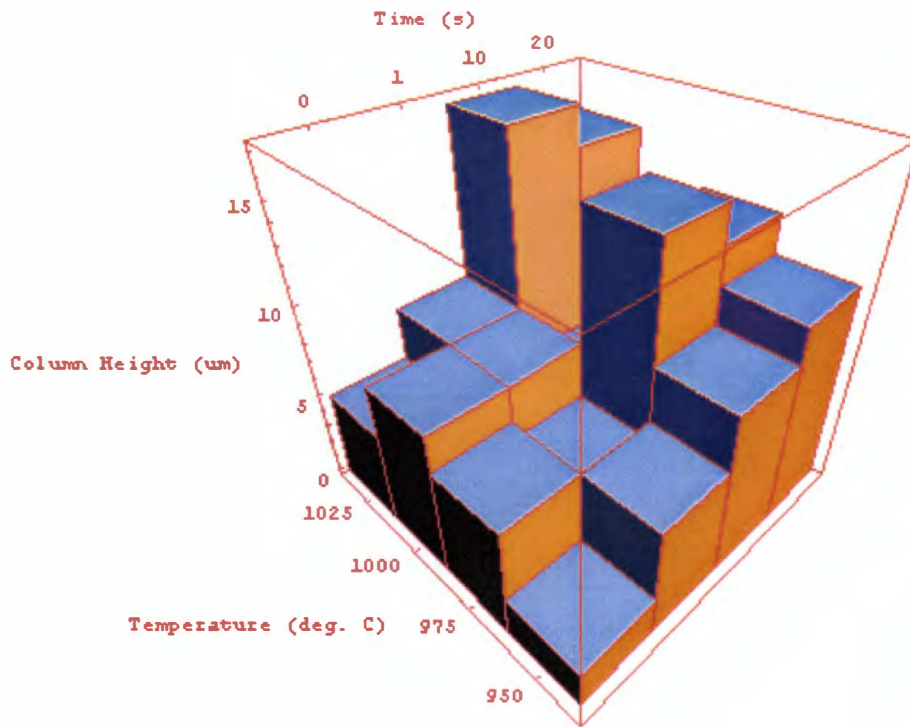**Figure 27** Interface width as calculated for each time and temperature combination.

Figure 28 Column height as measured for each time and temperature combination.

In both the experimental work and in the model an increase in solubility for Fe in the coating and for Ni and P in the substrate was seen. In order to make a direct comparison for these values, it would be necessary to have a method to integrate the amount of an element in a particular area. To a minor degree this can be accomplished by examining the x-ray maps produced by the electron microprobe. What is interesting is that the pseudo-binary phase diagram suggested that Fe_3P would be fairly common in the interface and coating regions; but failed to predict what other compounds would form (Table 4). The most likely reason for this is the inability of Thermo-Calc™ to predict non-equilibrium compounds. From Figure 4 it is seen that the cooling curve has a steep gradient. The steep gradient of the cooling curve along with the short processing times limits the amount of homogenization that will occur in the coating resulting in many non-equilibrium and metastable compounds being formed.

Compositional cooling, or isothermal solidification was expected at the interface since P is a temperature depressant in both the Ni-P and the Fe-P systems. Because Fe and Ni are miscible and tend to behave in a similar fashion, and because the Fe-P and the Ni-P systems are similar to each other (eutectics at 10.1 wt% P and 11 wt% P respectively), the ternary Fe-Ni-P system is assumed to behave in a manner similar to that of the binary systems. The lack of P (1.1 ±0.5 wt%) within the columns (Figure 29), which are confined to the interface region, is a good indicator that they have a composition with a higher melting point than the rest of the coating. In fact, aside from the substrate, the amount of phosphorus in the system is lowest in the columns. The presence of cores and dendrites in the coating was also predicted, although close inspection indicates that some
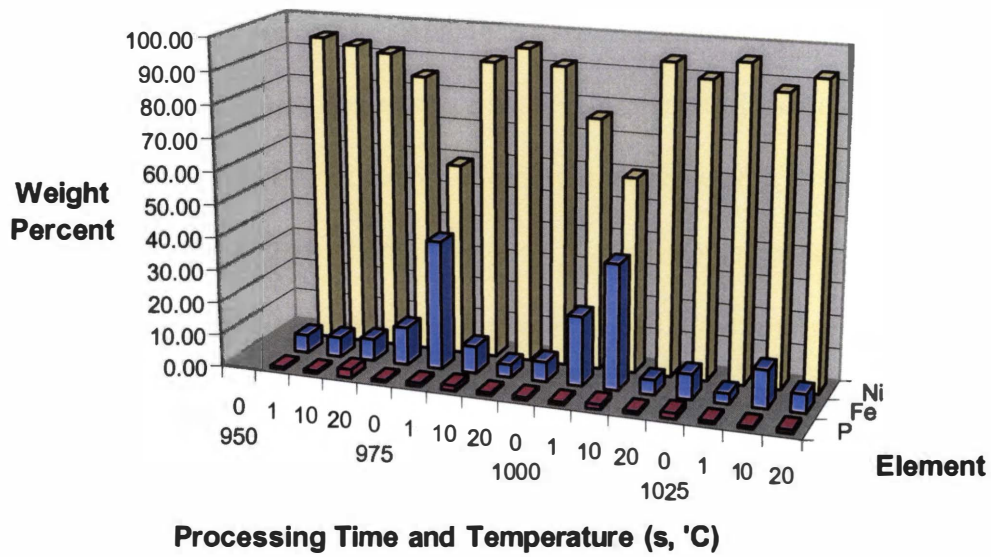
75

Figure 29 Composition of the columns (wt %) formed from the interface during infrared processing of the Ni-P coating on the A570 steel substrate.

of the dendrites may not be due to coring upon cooling, but might be pinched off from some of the columns. Inspection of the dendrite composition (Figure 30) shows that the dendrites are similar in composition to the columns, which is further evidence that the dendrites might be pinched off from the columns. Finally, the length of the columns seems to remain fairly static with increasing time and temperature (Figure 18 and Figure 19), which could be an indicator that there is some critical length (about 15μm) beyond which they cannot grow, or that they pinch off forming a dendritic core. As expected though, there is much more iron present in the coating than Ni and P in the substrate. Also as expected, a eutectic structure was found in the coating matrix surrounding the dendrites or cores. Since the coating matrix has a composition that is nearly uniform for all of the processing times and temperatures (Figure 31), and the amount of P present in the matrix (12.2 ± 0.6 wt%) is similar to that in both the Fe-P and Ni-P binary systems it is assumed that the coating matrix has the lowest melting temperature of the coating system and thus solidifies out last. Examination of the pseudo-binary phase diagram (Figure 9) indicates that the fcc phase is the first to solidify upon cooling followed by Fe_3P and transforming into a complex steel-like microstructure at room temperature.

In conclusion, it was found that with carefully designed experiments in combination with some careful study, and some knowledge of diffusion, phase diagrams, and phase transformations, Dictra™ and Thermo-Calc™ can be useful in assessing the Ni-P system prior to any coating procedures. Dictra™ does not provide any data regarding what phases may be present, but used in conjunction with Thermo-Calc™ and some inductive reasoning, some reasonable inferences can be made as to how the system will perform.
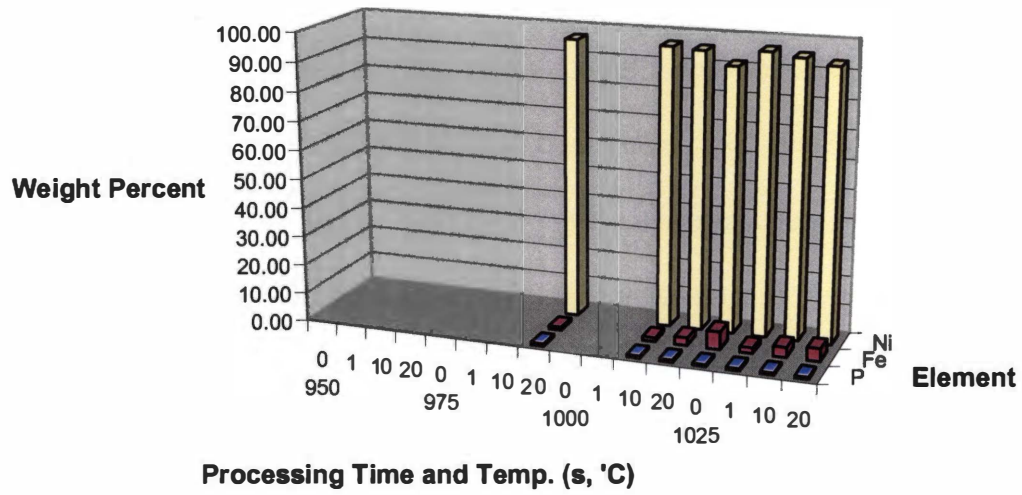
Figure 30 Composition of the dendrites (wt%) isolated in the coating during infrared processing of the Ni-P coating on the A570 steel substrate.
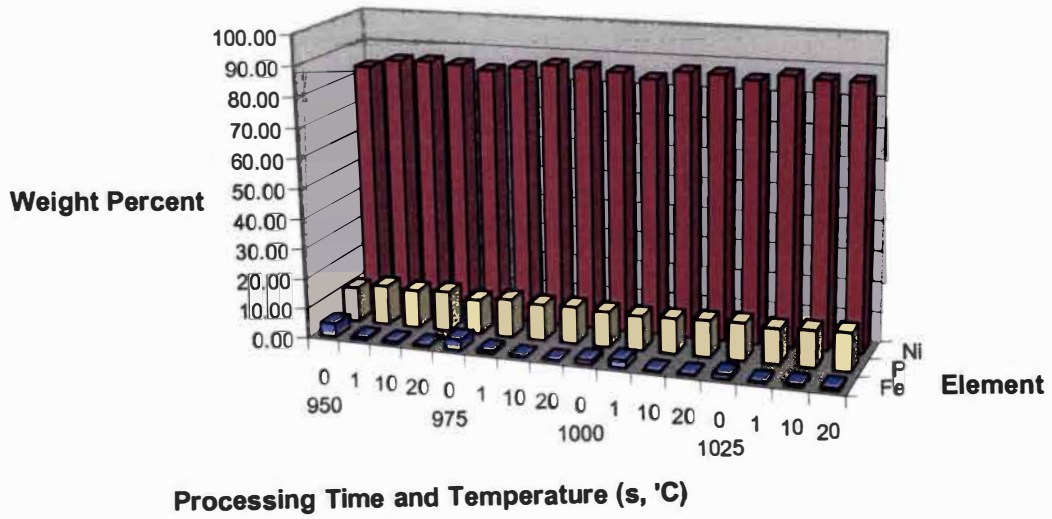
Figure 31 Composition (in wt%) of the coating matrix during infrared processing of a Ni-P coating on an A570 steel substrate.

Although, neither model provides definite information on the final microstructure, Dictra™ provides very little information on elemental distribution, both models in compliment can be used as tools to limit the possibilities when working with a new system. Finally, it was determined through this work that with careful management of the processing times and temperatures, the microstructure of the coating and the degree of phase transformation in the coating can be controlled.

4.5 Future Work

There is still a lot of work that can be done on this system. With more models available and faster computers, it would be nice to do some phase-field modeling of this system in an attempt to predict what microstructure might look like. In sticking closer to the present work though, more accurate predictions could be made using Dictra™ by carefully programming heating and cooling rates to match those of the experiment. Further work using Thermo-Calc™ could include plotting of ternary Fe-Ni-P isothermal sections, and further development of the Ni-P/A570 system by calculating more pseudo-binary phase diagrams at other coating alloy compositions. Evidence that the columns and dendrites are solidifying isothermally could be bolstered with Scheil calculations using Thermo-Calc™ and the column, dendrite and matrix compositions to predict the melting temperature for each of these systems. The same work should also be done for other substrates, such as 4340 steel or H13 steel. Originally this work was suggested in order to model the coating system as a possible matrix for ceramic reinforcements, so it would make sense to model the system with ceramic particles, varying the loading and

the type of particles (WC, TiC, VC, etc.). As stated above, there are plenty of new

models, it would be very helpful to use the Thermo-Calc™ and Dictra™ results with

another model to gain a better idea of the system.

References

[1] C. N. Panagopoulos, A. E. Markaki, P. E. Agathocleous, *"Eximer Laser Treatment of Nickel-Coated Cast Iron"*, Materials Science and Engineering A, A241 (1998) 226-232.

[2] J. W. Jang, P. G. Kim, K. N. Tu, D. R. Frear, and P. Thompson, *"Solder Reaction-Assisted Crystallization of Electroless, Ni-P Under Bump Metallization in Low Cost Flip Chip Technology"*, Journal of Applied Physics, 85 (1999) 8456-8463.

[3] C. –Y. Lee, and K. –L. Lin, *"The Interaction Kinetics and Compound Formation between Electroless Ni-P and Solder"*, Thin Solid Films 249 (1994) 201-206.

[4] G. Ghosh, *"Interfacial Microstructure and the Kinetics of Interfacial Reaction in Diffusion Couples Between Sn-Pb Solder and Cu/Ni/Pd Metallization"*, Acta Materialia, 48 (2000) 3719-3738.

[5] D. R. Frear, and P. T. Vianco, *"Intermetallic Growth and Mechanical Behavior of Low and High Melting Temperature Solder Alloys"*, Metallurgical and Materials Transactions A, 25A (1994) 1509-1523.

[6] C. Zhang, G. Qiao, and Z. Jin, *"Active Brazing of Pure Alumina to Kovar Alloy Based on the Partial Transient Liquid Phase (TLP) Technique with Ni-Ti Interlayer"*, Journal of the European Ceramic Society, 22 (2002) 2181-2186.

[7] A. Ludwig, *"The interface Response-Functions in Multi-Component Alloy Solidification"*, Physica D, 124 (1998) 271-284.

[8] Y. Nakamura, M. Kambara, T. Izumi, and Y. Shiohara, *"Phase Diagram and Crystal Growth of RE123 Superconductive Oxides"*, Physica C, 235 (2000) 56-60

[9] W. J. Boettinger, S. R. Coriell, A. L. Greer, A. Karma, W. Kurz, M. Rappaz, and R. Trivedi, *"Solidification Microstructures: Recent Developments, Future Directions"*, Acta Materialia, 48 (2000) 43-70.

[10] O. Hunziker, and W. Kurz, *"Directional Solidification and Phase Equilibria in the Ni-Al System"*, Metallurgical and Materials Transactions A, 30A (1999) 3167-3175.

[11] A. A. Wheeler, N. A. Ahmad, W. J. Boettinger, R. J. Braun, G. B. McFadden, and B. T. Murray, *"Recent Developments in Phase-Field Models of Solidification"*, Advanced Space Research, 16 (1995) (7)163-(7)172.

[12] Y. Saito, G. Goldbeck-Wood, and H. Muller-Krumbhaar, *"Numerical Simulation of Dendritic Growth"*, Physical Review A, 38 (1988) 2148-2157.

[13] P. –R. Cha, D. –H. Yeon, and J. –K. Yoon, *"A Phase Field Model for Isothermal Solidification of Multicomponent Alloys"*, Acta Materialia, 49 (2001) 3295-3307.

[14] S. G. Kim, W. T. Kim, and T. Suzuki, *"Interfacial Compositions of Solid and Liquid in a Phase-Field Model with Finite Interface Thickness for Isothermal Solidification in Binary Alloys"*, Physical Review E, 58 (1998) 3316-3323.

[15] A. A. Wheeler, W. J. Boettinger, and G. B. McFadden, *"Phase-Field Model of Solute Trapping During Solidification"*, Physical Review E, 47 (1993) 1893-1909.

[16] J. Miettinen, *"Approximate Thermodynamic Solution Phase Data for Steels"*, Calphad, 22 (1998) 275-300.

[17] A. D. Pelton, and C. W. Bale, *"Computational Techniques for the Treatment of Thermodynamic Data in Multicomponent Systems and the Calculation of Phase Equilibria"*, Calphad, 1 (1977) 253.

[18] B. Sundman, B. Jansson, and J. –O. Andersson, *"The Thermo-Calc Databank System"*, Calphad, 9 (1985) 153-190.

[19] M. Hillert, L. Hoglund, and M. Schalin, *"Role of Back-Diffusion Studied by Computer Simulation"*, Metallurgical and Materials Transactions A, 30A (1999) 1635-1641.

[20] J. Tiaden, B. Nestler, H. J. Diepers, and I. Steinbach, *"The Multiphase-Field Model with an Integrated Concept for Modelling Solute Diffusion"*, Physica D, 115 (1998) 73-86.

[21] A. Jacot, and M. Rappaz, *"A Two-Dimensional Diffusion Model for the Prediction of Phase Transformations: Application of Austenization and Homogenization of Hypoeutectoid Fe-C Steels"*, Acta Materialia, 45 (1997) 575-585.

[22] A. Jacot, and M. Rappaz, "*A Pseudo-Front Tracking Technique for the Modeling of Solidification Microstructures in Multi-Component Alloys*", Acta Materialia, 50 (2002) 1909-1926.

[23] J. A. Warren, and W. J. Boettinger, "*Prediction of Dendritic Growth and Microsegregation Patterns in a Binary Alloy Using the Phase-Field Method*", Acta Metallurgica et Materialia, 43 (1995) 689-703.

[24] H. Assadi, A. A. Shirzadi, and E. R. Wallach, "*Transient Liquid Phase Diffusion Bonding Under a Temperature Gradient: Modelling of the Interface Morphology*", Acta Materialia, 49 (2001) 31-39.

[25] F. J. J. van Loo, "*Multiphase Diffusion in Binary and Ternary Solid-State Systems*", Progress in Solid State Chemistry, 20 (1990) 47-99.

[26] V. Leute, "*Thermodynamics of Solid Solutions with Ordering Tendencies*", Calphad, 20 (1996) 407-418.

[27] K. Glasner, "*Solute Trapping and the Non-Equilibrium Phase Diagram for Solidification of Binary Alloys*", Physica D, 151 (2001) 253-270.

[28] V. Leute, A. Behr, C. Hunting, and H. M. Schmidtke, "*Phase Diagram and Diffusion Properties of the Quasibinary System (Sn, Pb)S*", Solid State Ionics, 68 (1994) 287-294.

[29] Y. Nakamura, T. Izumi, and Y. Shiohara, *Analysis of Growth Behaviour of the RE123 Crystals Using the Ternary Phase Diagram*", Physica C, 341-348 (2000) 2417-2420.

[30] J. –S. Park, and R. Trivedi, "*Convection-Induced Novel Oscillating Microstructure Formation in Peritectic Systems*", Journal of Crystal Growth, 187 (1998) 511-515.

[31] P. Mazumder, R. Trivedi, and A. Karma, "*A Model of Convection-Induced Oscillatory Structure Formation in Peritectic Alloys*", Metallurgical and Materials Transactions A, 31A (2000) 1233-1246.

[32] A. Karma, W. –J. Rappel, B. C. Fuh, and R. Trivedi, "*Model of Banding in Diffusive and Convective Regimes During Directional Solidification of Peritectic Systems*", Metallurgical and Materials Transactions A, 29A (1998) 1457-1470.

[33] B. –J. Lee and K. H. Oh, "*Numerical Treatment of the Moving Interface in Diffusional Reactions*", Zeitschrift fur Metallkunde, 87 (1996) 195-204.

[34] S. Crusius, G. Inden, U. Knoop, L. Hoglund, and J. Agren, "*On the Numerical Treatment of Moving Boundary Problems*", Zeitschrift fur Metallkunde, 83 (1992) 673-678.

[35] S. A. Moir, and D. M. Herlach, "*Observation of Phase selection from Dendrite Growth in Undercooled Fe-Ni-Cr Melts*", Acta Materialia, 45 (1997) 2827-2837.

[36] S. C. Gill, and W. Kurz, "*Rapidly Solidified Al-Cu Alloys—II. Calculation of the Microstructure Selection Map*", Acta Metallurgica et Materialia, 43 (1995) 139-151.

[37] D. J. Srolovitz, M. P. Anderson, G. S. Grest, and P. S. Sahni, *Acta Metallurgica*, 32 (1984) 783.

[38] H. V. Atkinson, *Acta Metallurgica*, 36 (1988) 469.

[39] A. D. Rollet, D. J. Srolovitz, and M. P. Anderson, *Acta Metallurgica*, 37 (1989) 1227.

[40] C. –A. Gandin, and M. Rappaz, *Acta Metallurgica et Materialia*, 42 (1994) 2233.

[41] P. Shah, P. Chakrabarti, and C. Chakravarty, "*Structure and Melting of Morse Solids*", Molecular Physics, 99 (2001) 573.

[42] A. A. Wheeler, W. J. Boettinger, and G. B. McFadden, "*Phase-Field Model for Isothermal Phase Transitions in Binary Alloys*", Physical Review A, 45 (1992) 7424-7440.

[43] S. G. Kim, W. T. Kim, and T. Suzuki, "*Phase-Field Model for Binary Alloys*", Physical Review E, 60 (1999) 7186-7197.

[44] G. W. Marshall, D. B. Lewis, D. Clayton, K. Blake and B. Dodds, "*The Electrodeposition of Ni-P-Al₂O₃ Deposits*", Surface and Coatings Technology, 96 (1997) 353-358.

[45] G. W. Marshall, *Electrodeposition of Alloys: Principles and Practice*, **Academic Press**, New York, (1963) 461-464.

[46] U. Pittermann, and S. Ripper, "*Direct Investigation by Electron Diffraction of the Crystallization of NiP-Alloys*", Zeitschrift fur Metallkunde, 74 (1983) 783-786.

[47] M. Earming, L. Shoufu, and L. Pengxing, "*A Transmission Electron Microscopy Study on the Crystallization of Amorphous Ni-P Electroless Deposited Coatings*", Thin Solid Films, 166 (1988) 273-280.

[48] M. W. Mahoney, and P. J. Dynes, "*The Effects of Thermal History and Phosphorus Level on the Crystallization Behavior of Electroless Nickel*", Scripta Metallurgica, 19 (1985) 539-542.

[49] R. M. Allen, and J. B. VanderSande, "*The Structure of Electroless Ni-P Films as a Function of Composition*", Scripta Metallurgica, 16 (1982) 1161-1164.

[50] S. V. S. Tyagi, S. K. Barthwal, and V. K. Tondon, *"The Annealing Behavior of Electroless Noncrystalline Nickel Phosphorus Films"*, *Thin Solid Films*, 169 (1989) 229-233.

[51] L. Chandrasekaran, N. Saunders, and A. P. Miodownik, *"On the Nature of Bonding in Transition Metal-Phosphorus Alloys"*, *Calphad*, 11 (1987) 163-164.

[52] G. Straffelini, D. Columbo, and A. Molinari, *"Surface Durability of Electroless Ni-P Composite Deposits"*, *Wear*, 236 (1999) 179-188.

[53] R. L. Zeller III, and L. Salvati Jr., *"Effects of Phosphorus on Corrosion Resistance of Electroless Nickel in 50% Sodium Hydroxide"*, *Corrosion*, 50 (1994) 457-467.

[54] S. J. Lee, and S. K. Wu, *"Infrared Joining Strength and Interfacial Microstructures of Ti-48Al-2Nb-2Cr Intermetallics using Ti-15Cu-15Ni Foil"*, *Intermetallics*, 7 (1999) 11-21.

[55] S. J. Lee, S. K. Wu, and R. Y. Lin, *"Infrared Joining of TiAl Intermetallics using Ti-15Cu-15Ni Foil –I. The Microstructure Morphologies of Joint Interfaces"*, *Acta Materialia*, 46 (1998) 1283-1295.

[56] R. Singh, *"Rapid Isothermal Processing"*, *Journal of Applied Physics*, 63 (1988) R59-R114.

[57] S. J. Lee, S. K. Wu, and R. Y. Lin, *"Infrared Joining of TiAl Intermetallics Using Ti-15Cu-15Ni Foil –II. The Microstructural Evolution at High Temperature"*, *Acta Materialia*, 46 (1998) 1297-1305.

[58] D. Gur and M. Bamberger, *"Reactive Isothermal Solidification in the Ni-Sn System"*, *Acta Materialia*, 46 (1998) 4917-4923.

[59] J. A. van Beek, S. A. Stolk, and F. J. J. van Loo, *"Multiphase Diffusion in the Systems Fe-Sn and Si-Sn"*, *Zeitschrift fur Metallkunde*, 73 (1982) 439-444.

[60] C. –L. Tsao, and S. –W. Chen, *"Interfacial Reactions in the Liquid Diffusion Couples of Mg/Ni, Al/Ni, and Al/(Ni)—Al$_2$O$_3$ Systems"*, *Journal of Materials Science*, 30 (1995) 5215-5222.

[61] V. N. Yeremenko, Y. V. Natanzon, and V. I. Dybkov, *"The Effect of Dissolution on the Growth of the Fe$_2$Al$_5$ Interlayer in the Solid Iron-Liquid Aluminum System"*, *Journal of Materials Science*, 16 (1981) 1748-1756.

[62] V. I. Dybkov, *"Reaction Diffusion in Heterogeneous Binary Systems –Part 1 –Growth of the Chemical Compound Layers at the Interface between Two Elementary Substances: One Compound Layer"*, *Journal of Materials Science*, 21 (1986) 3078-3084.

[63] S. Bader, W. Gust, and H. Hieber, *"Rapid Formation of Intermetallic Compounds by Interdiffusion in the Cu-Sn and Ni-Sn Systems"*, *Acta Metallurgica et Materialia*, 43 (1995) 329-337.

[64] A. A. Shirzadi, and E. R. Wallach, *"Analytical Modeling of Transient Liquid Phase (TLP) Diffusion Bonding when a Temperature Gradient is Imposed"*, *Acta Materialia*, 47 (1999) 3551-3560.

[65] A. Shirzadi, and A. Ghousouni, U. K. Patent # 9709167.2, *Metal Bonding*.

[66] A. A. Shirzadi, and E. R. Wallach, *"Temperature Gradient Transient Liquid Phase Diffusion Bonding: a New Method for Joining Advanced Materials"*, *Science and Technology of Welding and Joining*, 2 (1997) 89-94.

[67] S. R. Cain, J. R. Wilcox and R. Venkatraman, *"A Diffusional Model for Transient Liquid Phase Bonding"*, *Acta Materialia*, 45 (1996) 701-707.

[68] M. Enomoto, H. Harada, and M. Yamazaki, *"Calculation of γ'/γ Equilibrium Phase Compositions in Nickel-Base Superalloys by Cluster Variation Method"*, *Calphad* 15 (1991) 143-158.

[69] *Metals Handbook, 10th ed. Volume 1: Properties and Selection: Irons, Steels, and High-Performance Alloys*, **ASM International**, Materials Park (1985) 691, 950.

[70] J. S. Kirkaldy, *Diffusion in the Condensed State*, **Institute of Materials**, London, (1987), 361.

[71] *Binary Phase Diagrams: Volume 1*, eds. T. B. Massalski, J. L. Murray, L. H. Bennett, H. Baker, and L. Kacprzak, **American Society for Metals**, Metals Park, (1986), 1083, 1086, 1090-1091.

[72] *Binary Phase Diagrams: Volume 2*, eds. T. B. Massalski, J. L. Murray, L. H. Bennett, H. Baker, and L. Kacprzak, **American Society for Metals**, Metals Park, (1986), 1738-1739.

[73] D. A. Porter, and K. E. Easterling, *Phase Transformations in Metals and Alloys*, **Stanley Thornes (Publishers) Ltd.**, Cheltenham, (1992) 214-216, 232-233.

[74] F. N. Rhines, *Phase Diagrams in Metallurgy: Their Development and Application*, **McGraw-Hill**, New York, (1956), 26-28, 49.

[75] D. Gupta, R. R. Campbell, and P. S. Ho in *Thin Film Interdiffusion and Reactions*, eds. J. M. Poate, K. N. Tu, and J. W. Mayer, **John Wiley and Sons**, New York, (1978) 161-165.

[76] M. L. Santella, *"Fundamental Metallurgical Considerations in Brazing and Soldering"*, *The Metal Science of Joining, Proceedings of the Fall Meeting of the Metallurgical Society—Americal Institute of Minerals and Metals Engineering, Metal Science and Joining Symposium*, Cincinnati, October 20-24, 1991, **American Society for Minerals, Metals and Materials**, (1992) 61-65.

Appendices

Appendix A

A.1 Outline for Thermo-Calc™ and Dictra™ Computations

A.1.1 Dictra™ Procedures

Using Dictra™ with a Linux interface to determine the interdiffusion of the primary elements (Fe, Ni, P, and Mn) in a system through the solid/liquid interface. The commands are typed in boldface and the variables are in normal font and italics represent special notes.

set-log NiP_A570

go data   *sets the module to be used*

switch ssol   *switches to the solubility database*

define-species ni p fe mn   *define species present*

reject-phases graph 112 v3c2 fecn alni cem white cu3p1 dia fe4n ksi al3ni2 al5fe4

does not calculate equilibria for species not present

get   *gets data for remaining species*

append mobility   *appends data from mobility database*

define-system   *defines species present in the system*

reject-phases graph 112 v3c2 fecn alni cem white cu3p1 dia fe4n ksi al3ni2 al5fe4

get

go dictra-module

set-conditions glob t o 1323; * n

enter-region steel		*sets the first region on the left to represent steel*
enter-region coat steel y		sets the next region to represent the coating
enter-grid		*assemble grid for calculations*
	steel	*steel region*
	3175e-6	*width of region*
	geo	*geometrically spaced grid points*
	100	*number of grid points*
	1.1	*R value for grid spacing*
enter-grid		
	coat	
	70e-6	
	geo	
	25	
	0.9	
enter-phase		
	active	*whether the phase is active or passive*
	steel	the name of the region where the phase exists
	matrix	*the phase exists as part of the matrix*
	fcc	*phase name*
enter-phase		
	active	
	coat	
	matrix	
	liq	

enter-composition

steel	*name of the region*
fcc	*phase name*
fe	*major constituent*
w-p	*expressed in weight percent*
c lin 0.142 0.142 mn lin 0.45 0.45	component name and homogeneity in model
ni lin 0 0	
p lin 0.12 0.12	

enter-composition

coat
liq

ni

w-p

fe lin 0 0

mn lin 0 0

p lin 10 10

set-simulation-condition ,,,,yes   *check interface position*

set-simulation-time 36e5,,,,, *set simulation time for time when reaction will be complete*

simulation   *performs simulation*

save NiP_A570

A.1.2 Thermo-Calc™ Procedures

Creating a Ni-10P/A570 steel, pseudo-binary phase diagram using Thermo-Calc™ with a Linux interface. The commands are typed in boldface and the variables are in normal font and italics represent special notes.

set-log NiP_sys,,,

go data	*sets module to use*
switch ssol	*sets database to use*
define-system Ni P	
get	*retrieves available data*
go p-3	*sets processing module*

change-status phases, graph, fecn, dia, cub, cu3p1, alni, al3ni2, suspend

set-conditions t=1800, p=101470, n=1, w(p)-.1*w(ni)=0, w(c)-0.00142*w(fe)=0, w(mn)-0.0045*w(fe)=0

list-conditions	*shows the equilibrium status of the system*
set-axis-variable	

1	*axis number*
w(fe)+w(c)+w(mn)	*condition (weight percent nickel)*
0	*low value on axis*
1	*high value of axis*
0.025	*increment*

set-axis-variable

2

t   *(temperature)*

0

1800

20

compute-equilibrium

compute-equilibrium

list-equilibrium

    screen

    vwcs

list-axis-variable   ***double check prior to plotting***

save

    NiP_A570

map   *computes the phase diagram and saves to the previously*

named file

post

set-label   *turns on computer labels on phase diagram*

    n

set-plot-format   *identifies output device*

    9   *registers screen as output device*

set-title Pseudo-Binary Phase Diagram for Ni-10P/A570   *sets plot title*

set-plot-options

    y   *turns header on*

    n   *turns logo off*

95

n	*turns footer off*
y	*turns on the white contour for post-script characters*
y	*turns on display for remote exponents*
0	*turns symbols at node points off*
0.1	*sets the symbol size*

set-diagram-axis

y	*y-axis*
t-c	*temperature in °C*

set-axis-text-status *set axis labels*

x	*x-axis*

Weight Fraction A570

set-axis-text-status

y
Temperature (deg. C)

Appendix B

B.1 Results from Dictra™ Simulations

Results are grouped by element in order of ascending processing temperature. Figure 32 is an example indicating the interface and the substrate and coating areas. In general the interface is at 317.5 x 10⁻⁵, the substrate is from 0 to 317.5 x 10⁻⁵ and the coating is in the area >317.5 x 10⁻⁵ and is either 70µm or 100µm thick. In each case curves 1-4 represent processing times of 0s, 1s, 10s, and 20s respectively. Distance shown is in meters, beware that the exponent is displayed remotely and may change from image to image.

B.1.1 Diffusion Plots for Iron
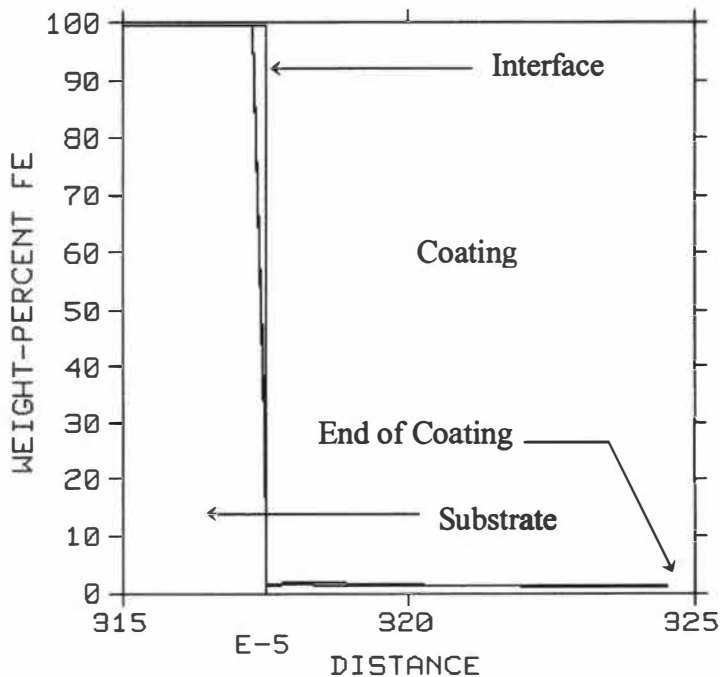
Figure 32 Location of key points in the Dictra™ calculated diffusion prediction for Fe processed at 950°C for 0, 1, 10, and 20s.
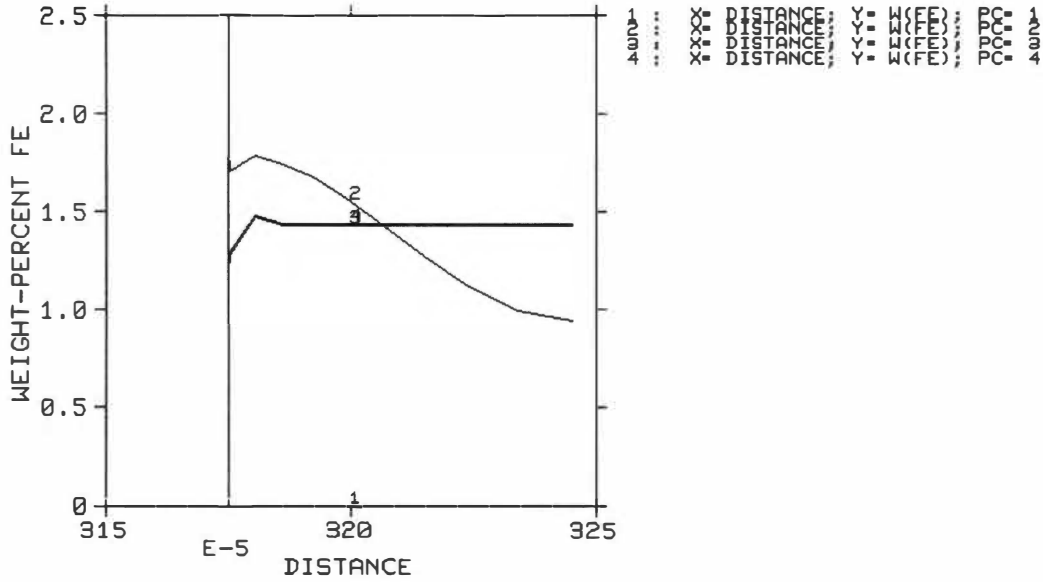
Figure 33 Diffusion of Fe near interface at 950°C (1223K) and 0, 1, 10, 20 seconds with no C in system.
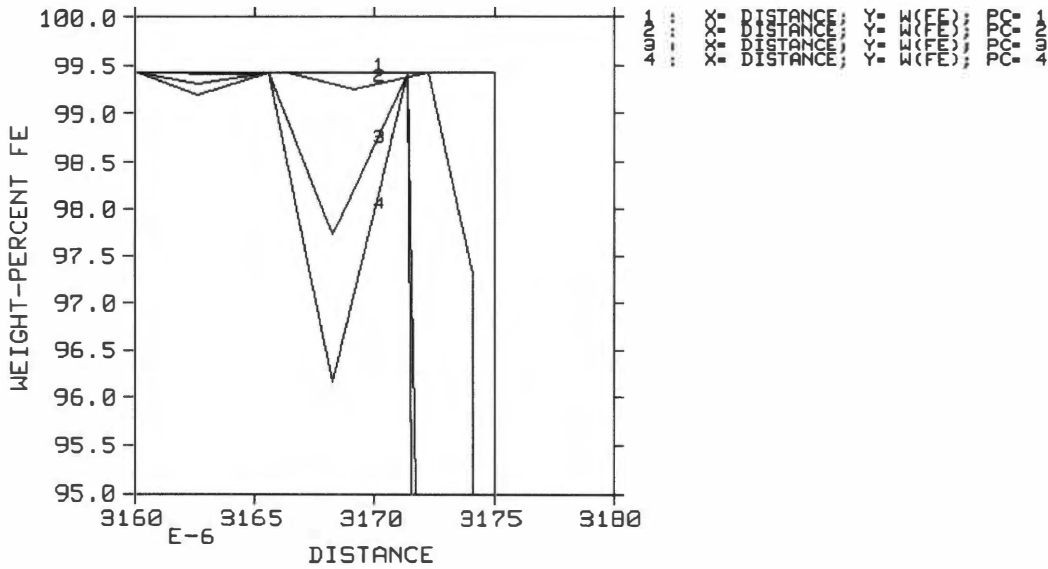
Figure 34 Diffusion of Fe near interface at 975°C (1248K) and 0, 1, 10, 20 seconds with no C in system, part 1.
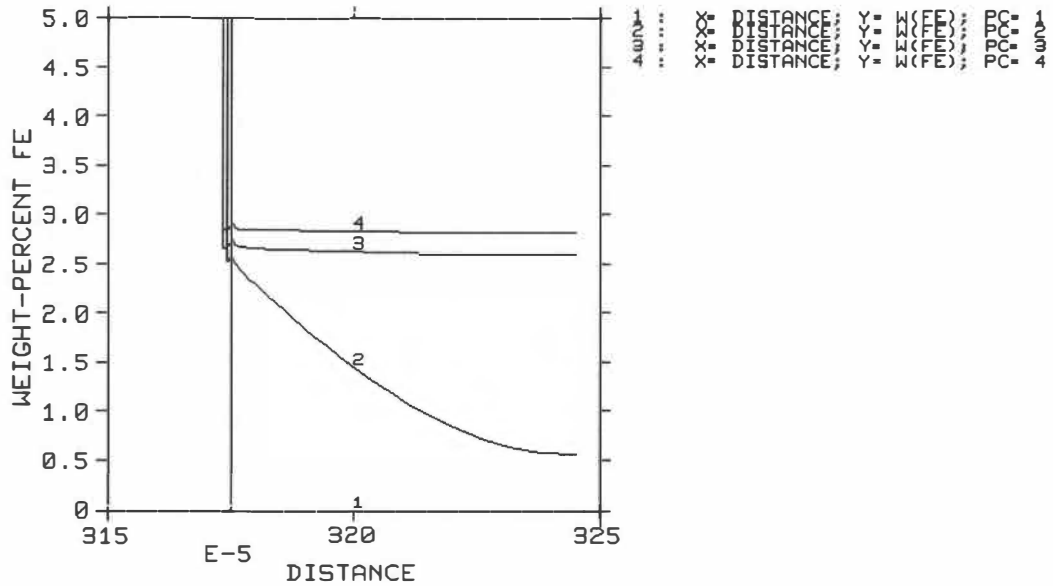
Figure 35 Diffusion of Fe near interface at 975°C (1248K) and 0, 1, 10, 20 seconds with no C in system, part 2.
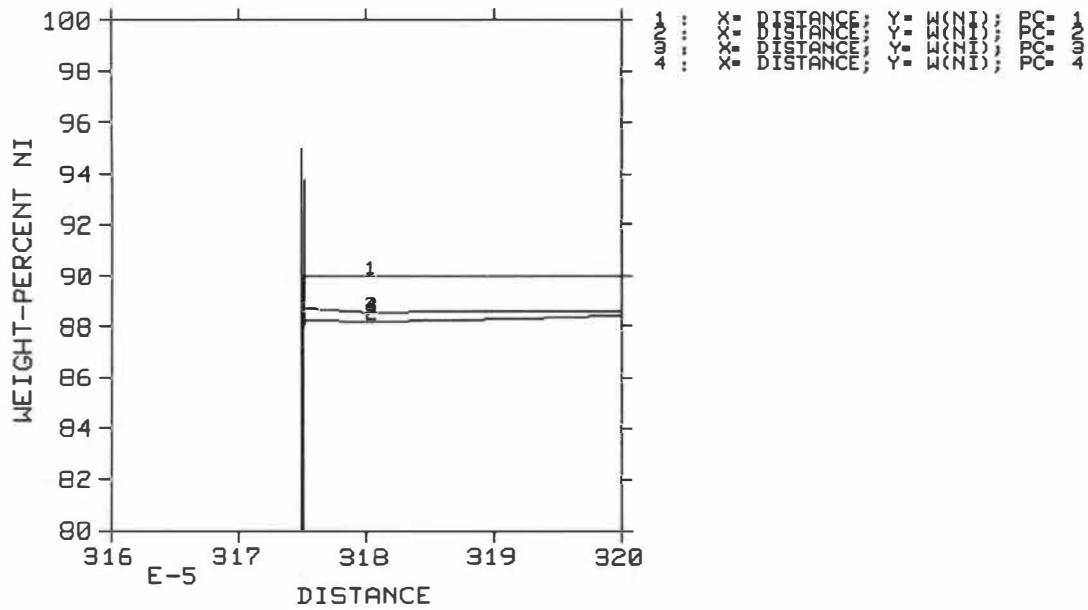
Figure 36 Diffusion of Fe near interface at 1000°C (1273K) and 0, 1, 10, 20 seconds with no C in system, part 1.

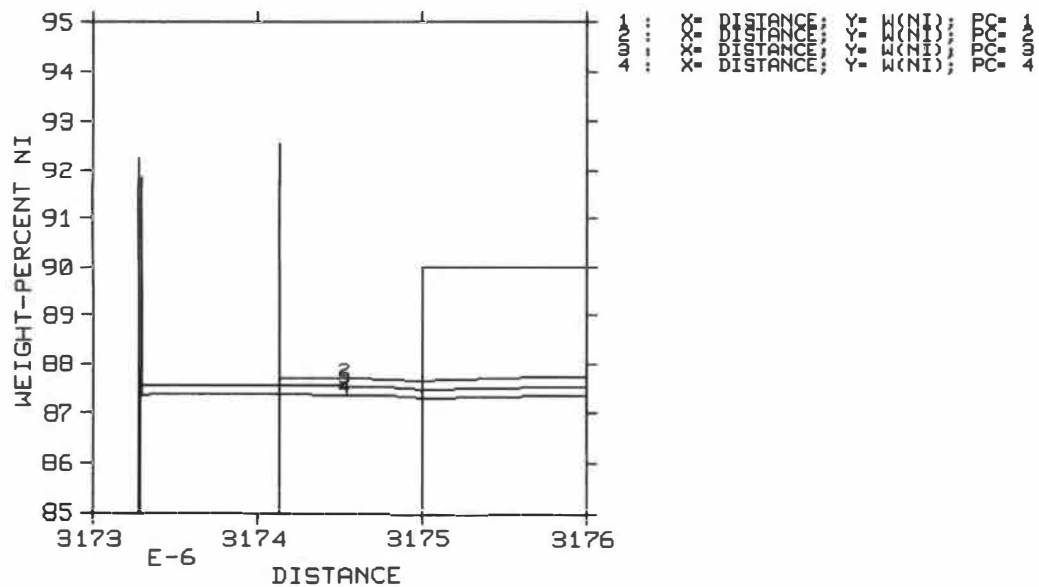DICTRA (2002-11-26:19.04.46) :Diffusion Couple for Ni-P/ASTM A570 at 1273K
    TIME = 0,1,10,20

1 : X= DISTANCE; Y= W(FE); PC= 1
2 : X= DISTANCE; Y= W(FE); PC= 2
3 : X= DISTANCE; Y= W(FE); PC= 3
4 : X= DISTANCE; Y= W(FE); PC= 4
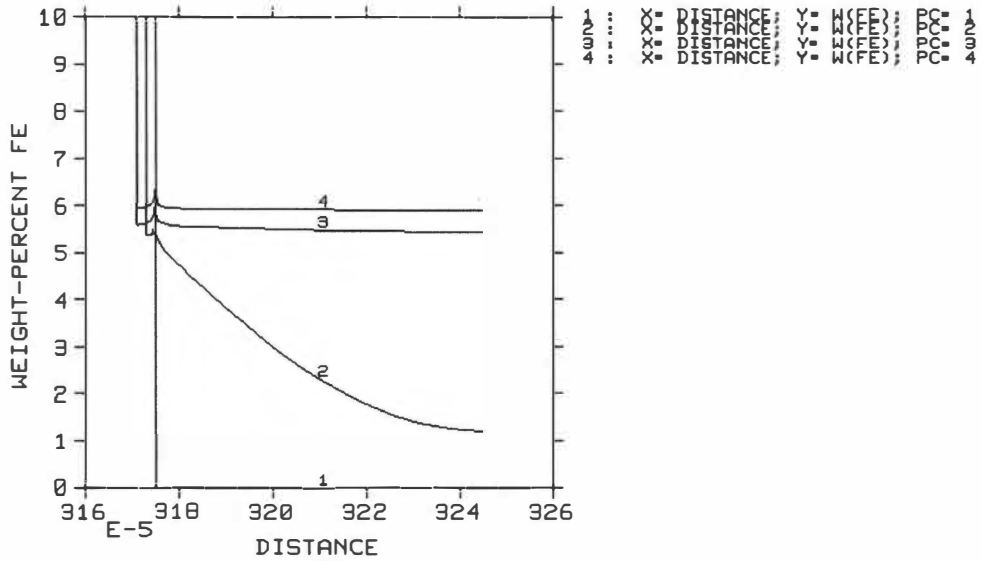
Figure 37 Diffusion of Fe near interface at 1000°C (1273K) and 0, 1, 10, 20 seconds with no C in system, part 2.

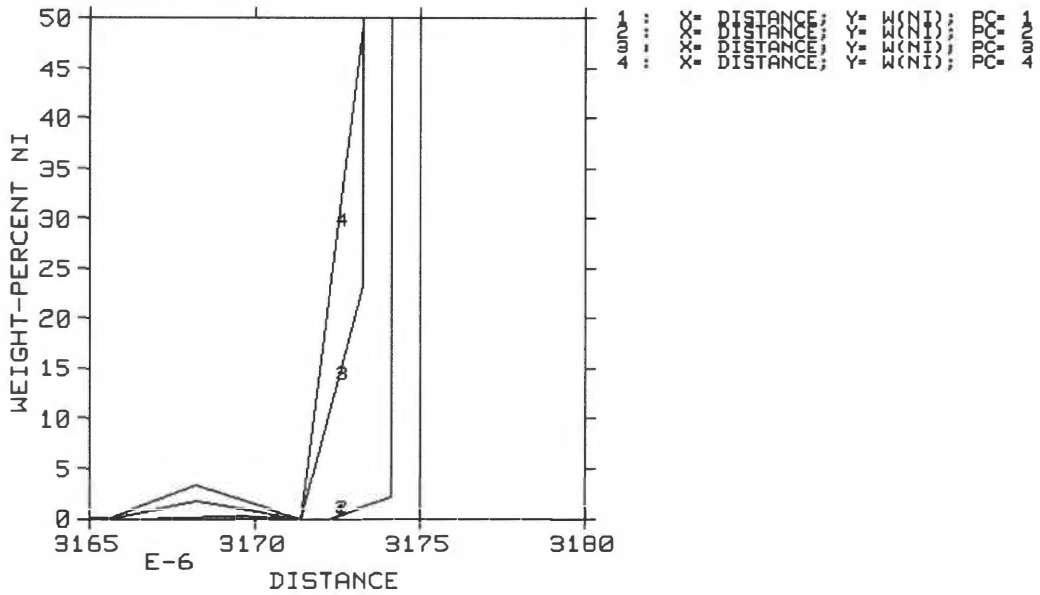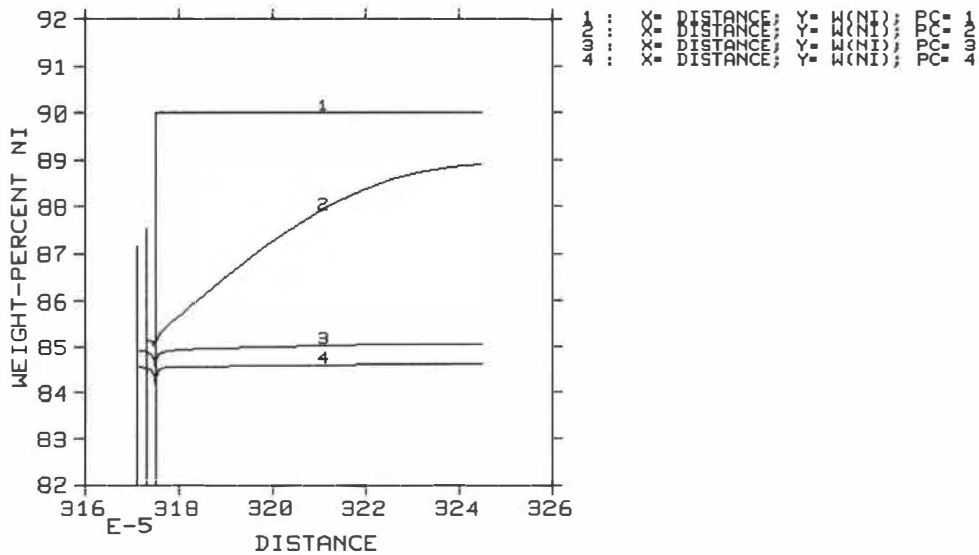DICTRA (2002-11-26:20.17.52) :Diffusion Couple for Ni-P/A570 Steel
    TIME = 0,1,10,20

1 : X= DISTANCE; Y= W(FE); PC= 1
2 : X= DISTANCE; Y= W(FE); PC= 2
3 : X= DISTANCE; Y= W(FE); PC= 3
4 : X= DISTANCE; Y= W(FE); PC= 4
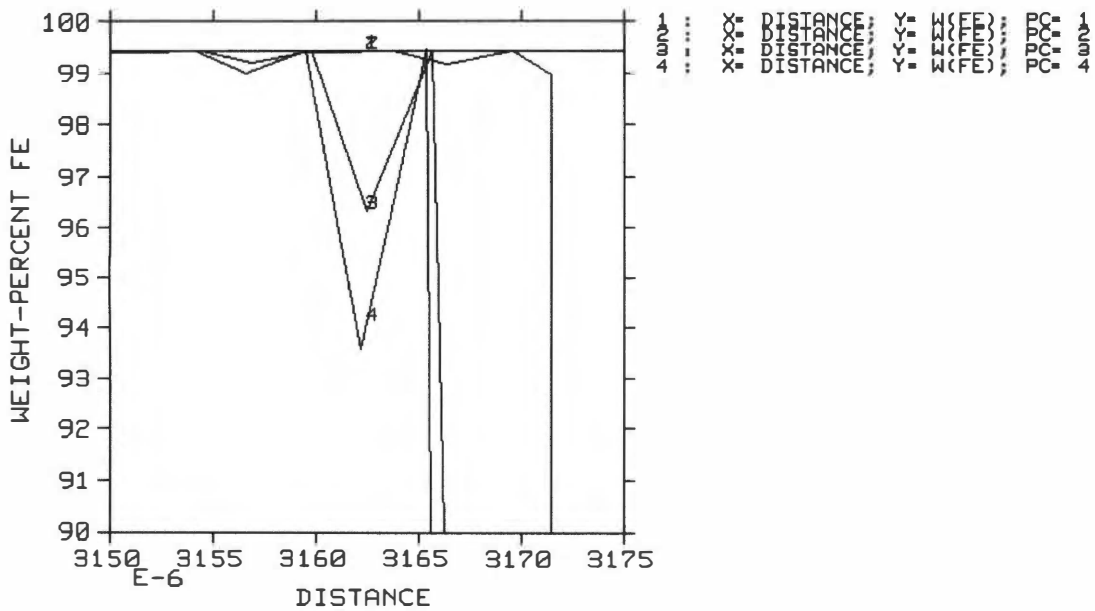
Figure 38 Diffusion of Fe near interface at 1025°C (1298K) and 0, 1, 10, 20 seconds with no C in system, part 1.

100

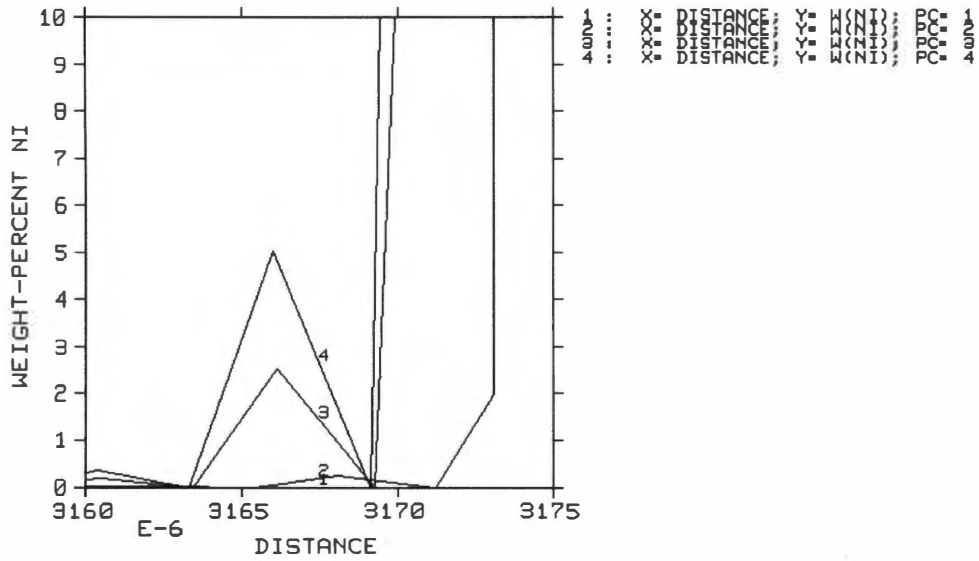DICTRA (2002-11-26:20.19.45) :Diffusion Couple for Ni-P/A570 Steel
TIME = 0,1,10,20
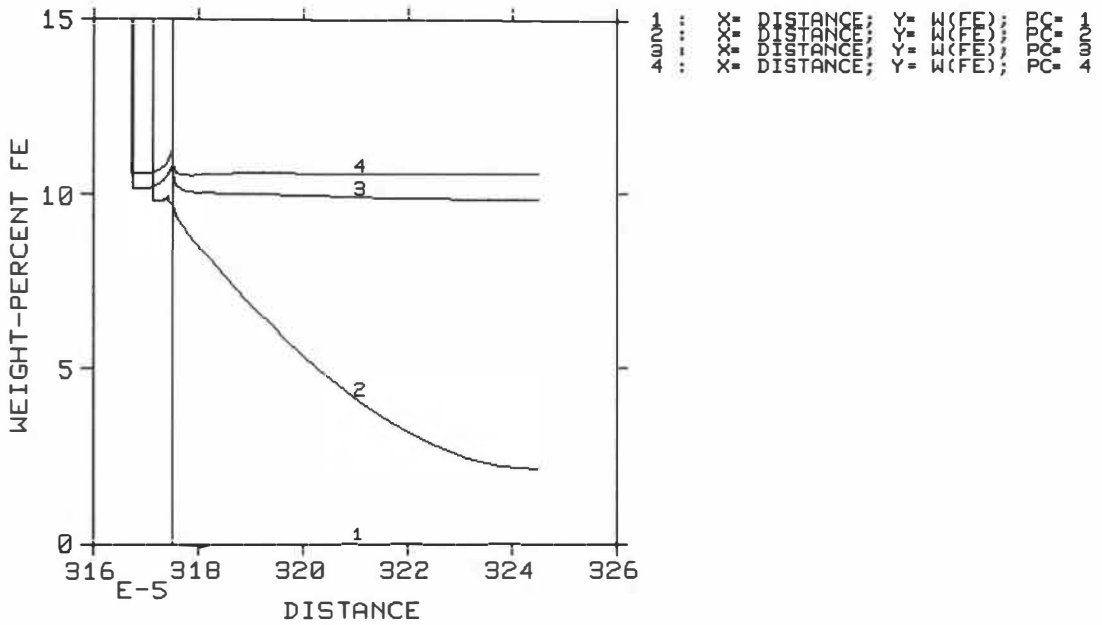
Figure 39 Diffusion of Fe near interface at 1025°C (1298K) and 0, 1, 10, 20 seconds with no C in system, part 2.

B.1.2 Diffusion Plots for Manganese

DICTRA (2002-11-20:23.10.37) :Diffusion Near Interface
TIME = 0,1,10,20
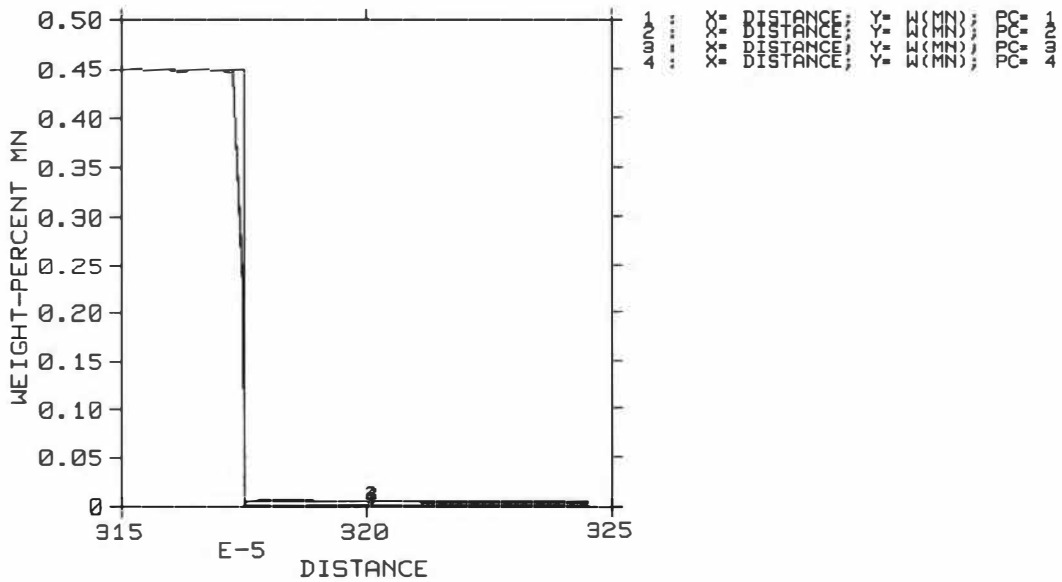
Figure 40 Diffusion of Mn near interface at 950°C (1223K) and 0, 1, 10, 20 seconds with no C in system, part 1.

101
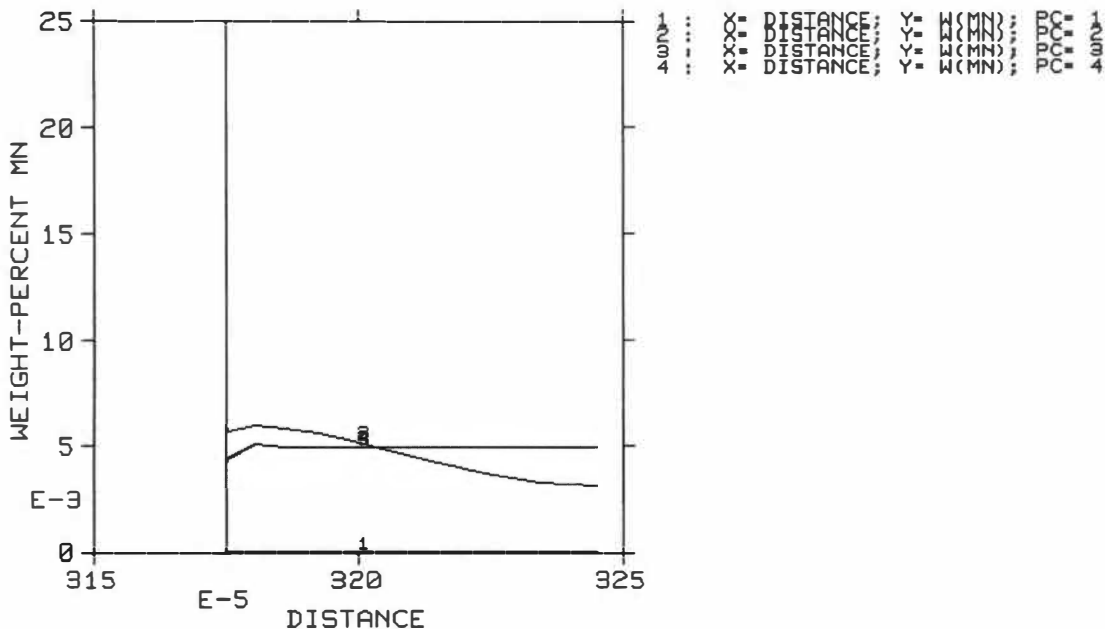
Figure 41 Diffusion of Mn near interface at 950°C (1223K) and 0, 1, 10, 20 seconds with no C in system, part 2.
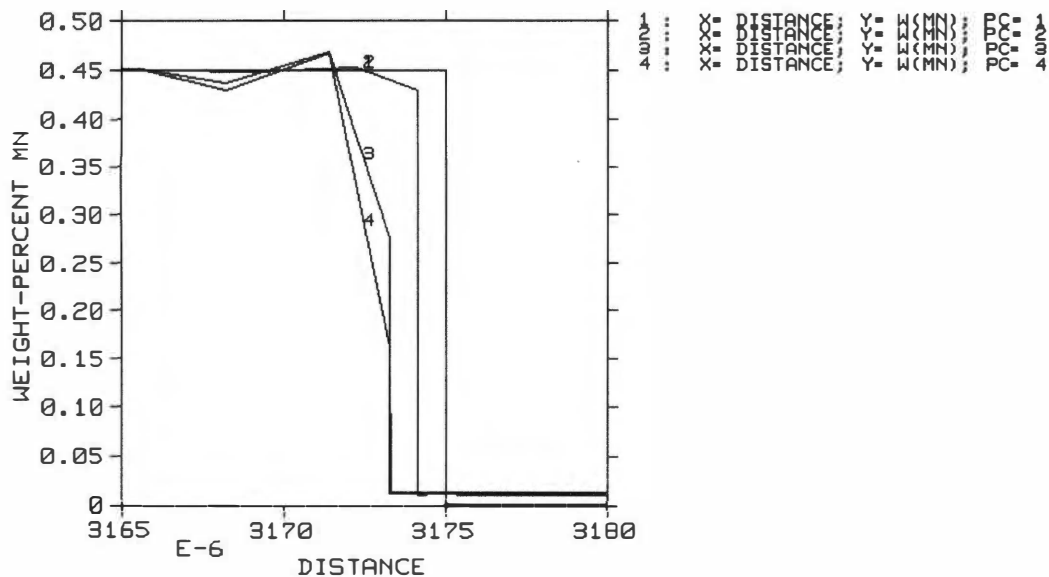
Figure 42 Diffusion of Mn near interface at 975°C (1248K) and 0, 1, 10, 20 seconds with no C in system, part 1.
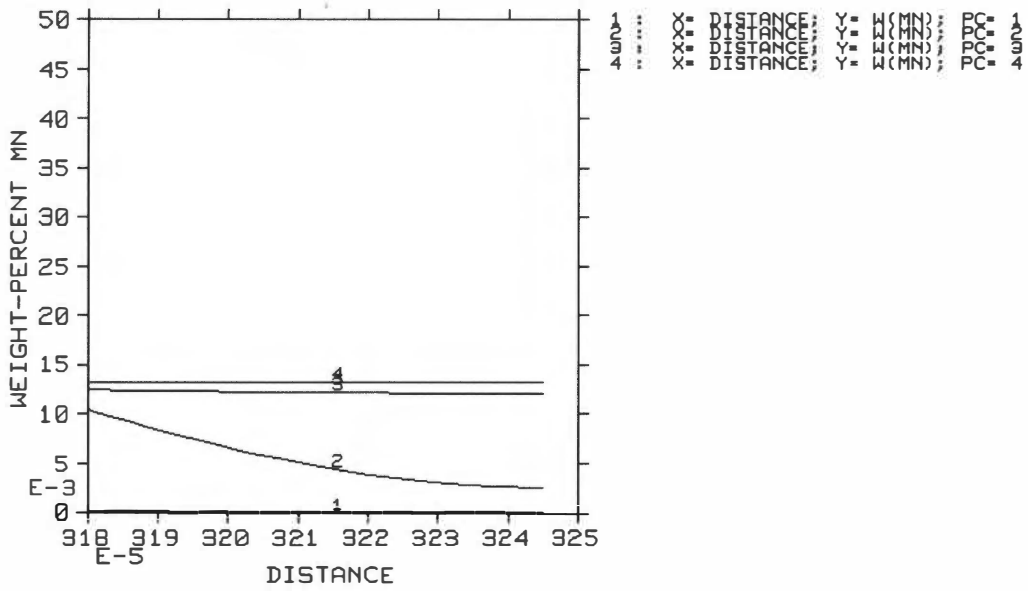
Figure 43 Diffusion of Mn near interface at 975°C (1248K) and 0, 1, 10, 20 seconds with no C in system, part 2.
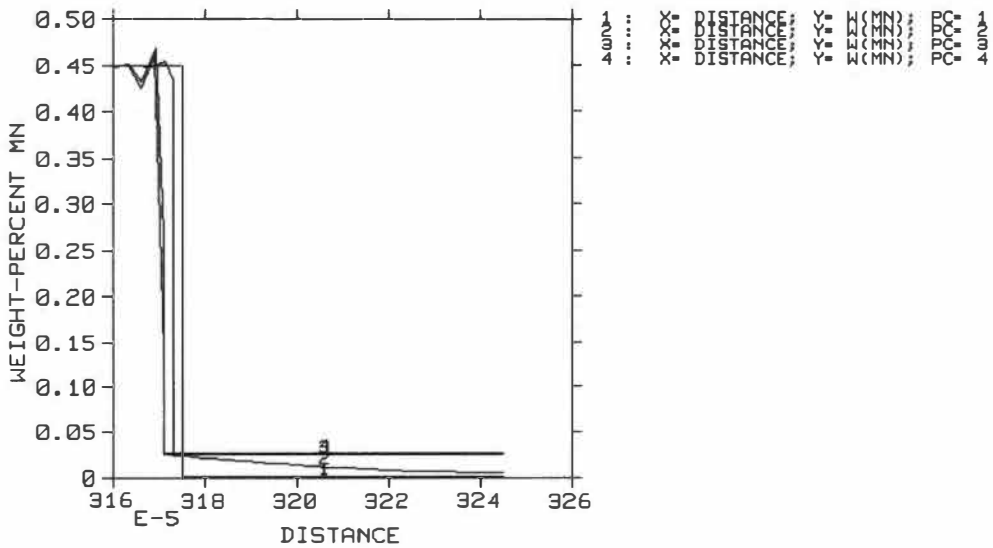
Figure 44 Diffusion of Mn near interface at 1000°C (1273K) and 0, 1, 10, 20 seconds with no C in system, part 1.
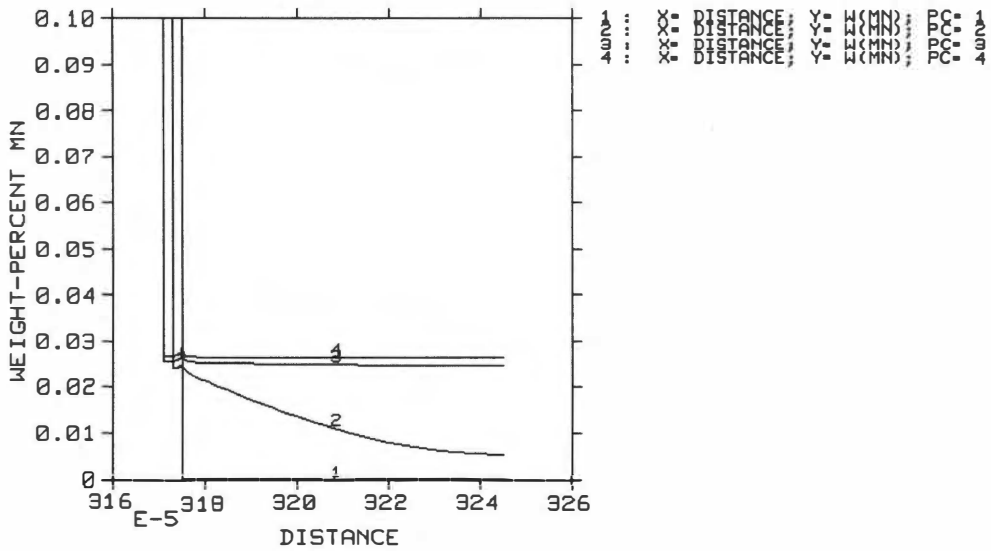
Figure 45 Diffusion of Mn near interface at 1000°C (1273K) and 0, 1, 10, 20 seconds with no C in system, part 2.
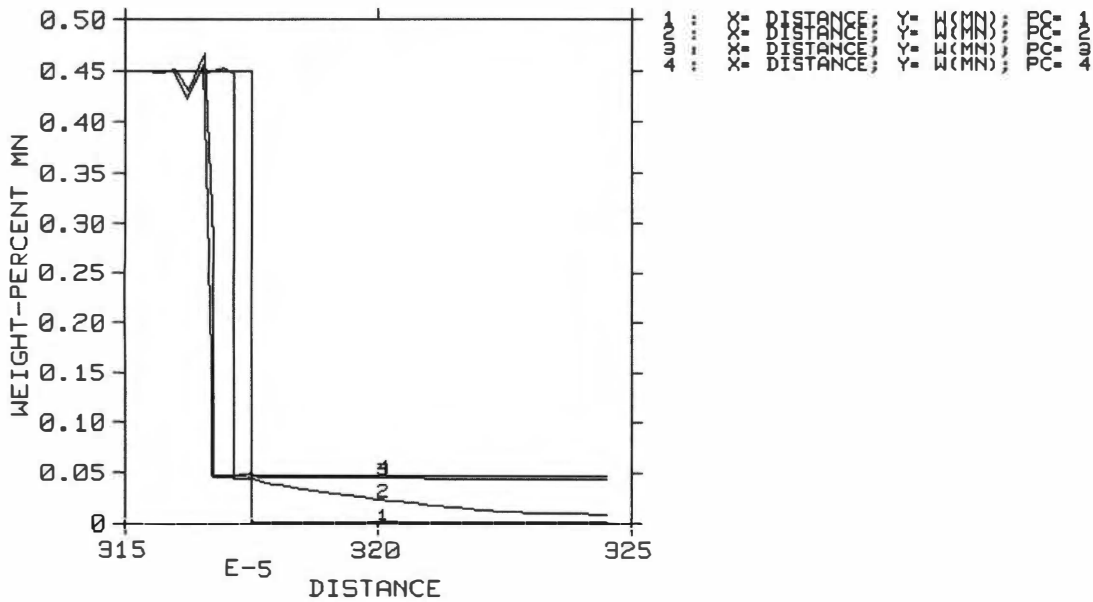
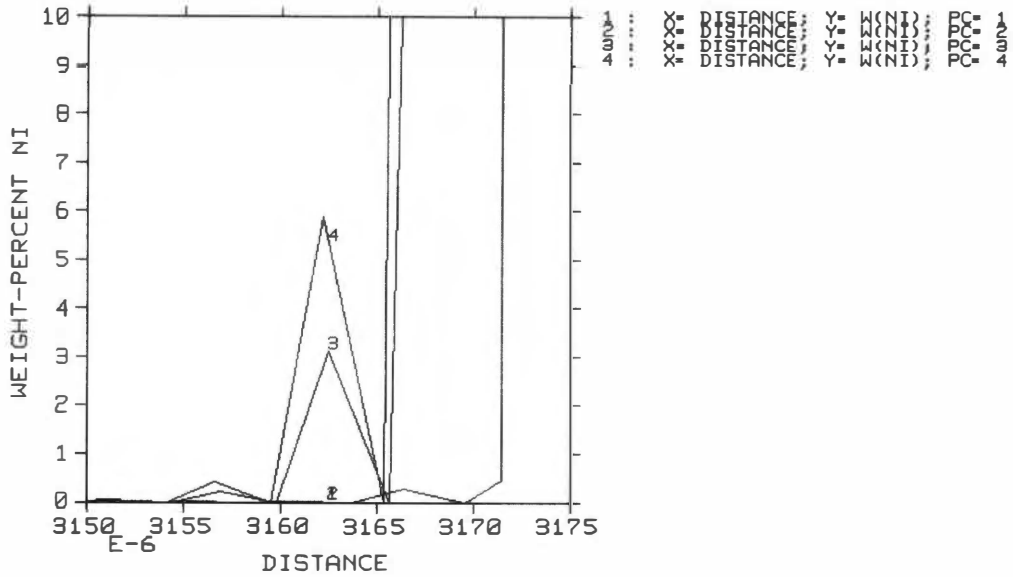**Figure 46** Diffusion of Mn near interface at 1025°C (1298K) and 0, 1, 10, 20 seconds with no C in system, part 1.
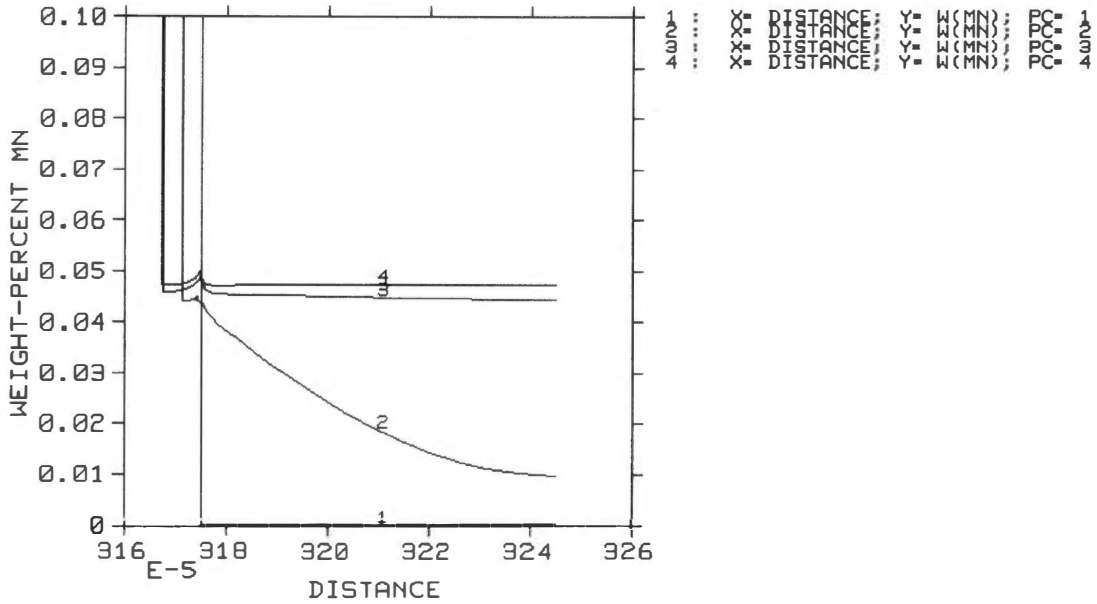
Figure 47 Diffusion of Mn near interface at 1025°C (1298K) and 0, 1, 10, 20 seconds with no C in system, part 2.

B.1.3 Diffusion Plots for Nickel

Figure 48 Diffusion of Ni near interface at 950°C (1223K) and 0, 1, 10, 20 seconds with no C in system, part 1.

Figure 49 Diffusion of Ni near interface at 950°C (1223K) and 0, 1, 10, 20 seconds with no C in system, part 2.
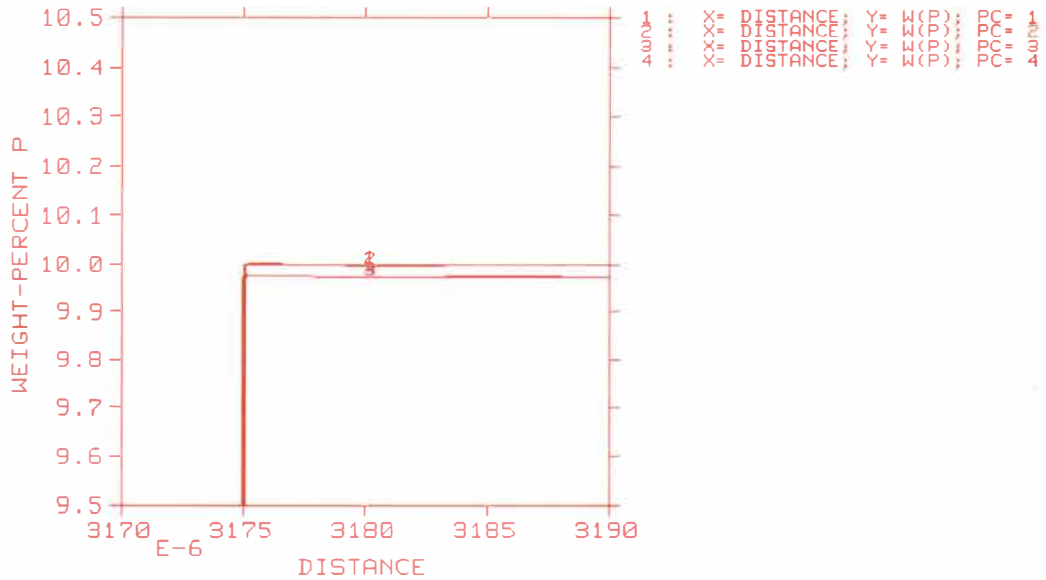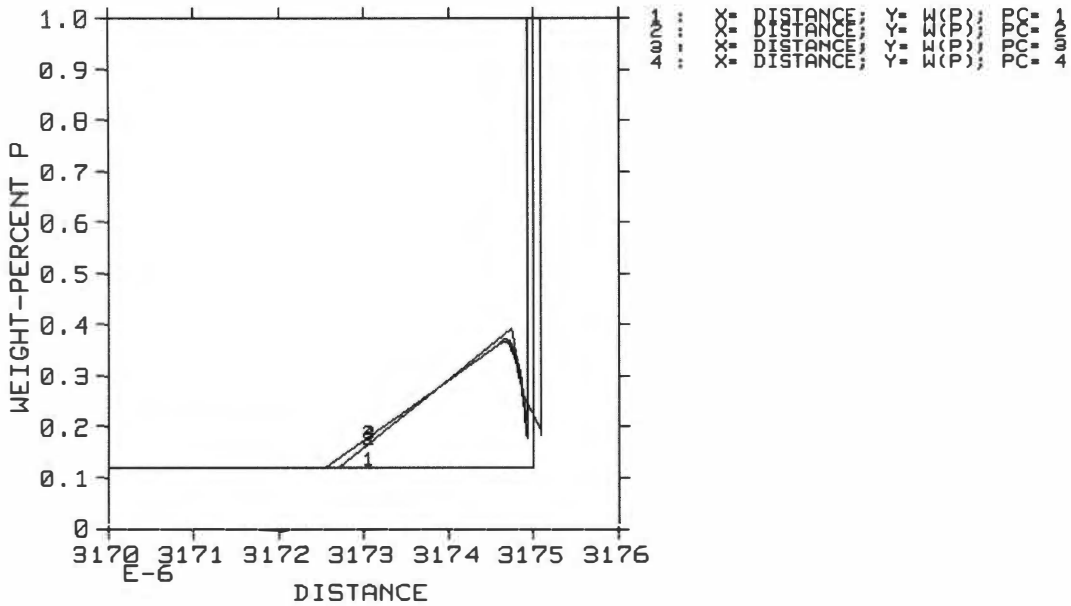

Figure 50 Diffusion of Ni near interface at 975°C (1248K) and 0, 1, 10, 20 seconds with no C in system, part 1.

106

DICTRA (2002-11-26:18.37.13) :Diffusion Couple for Ni-P/A570 at 1248K
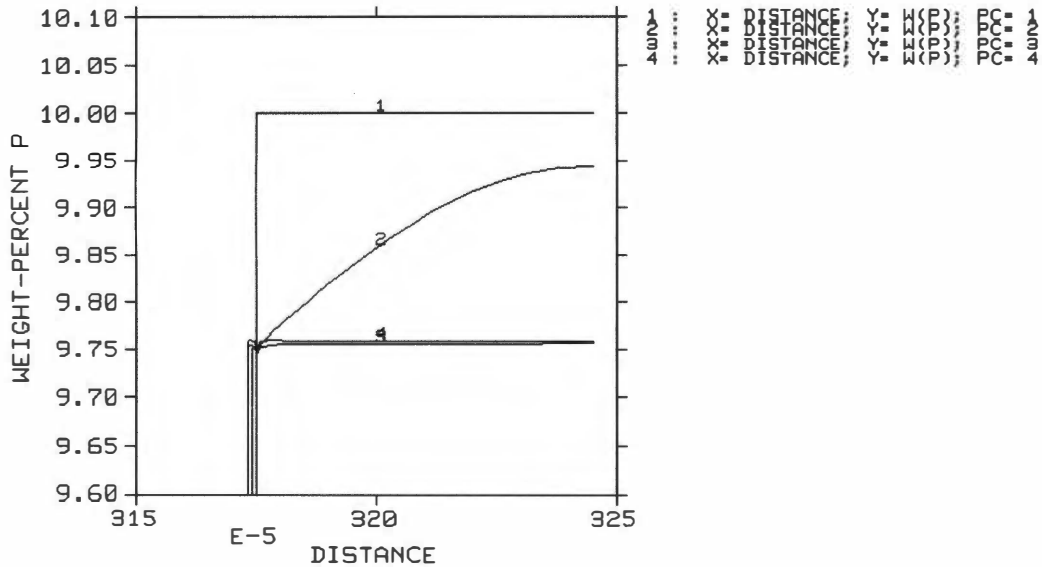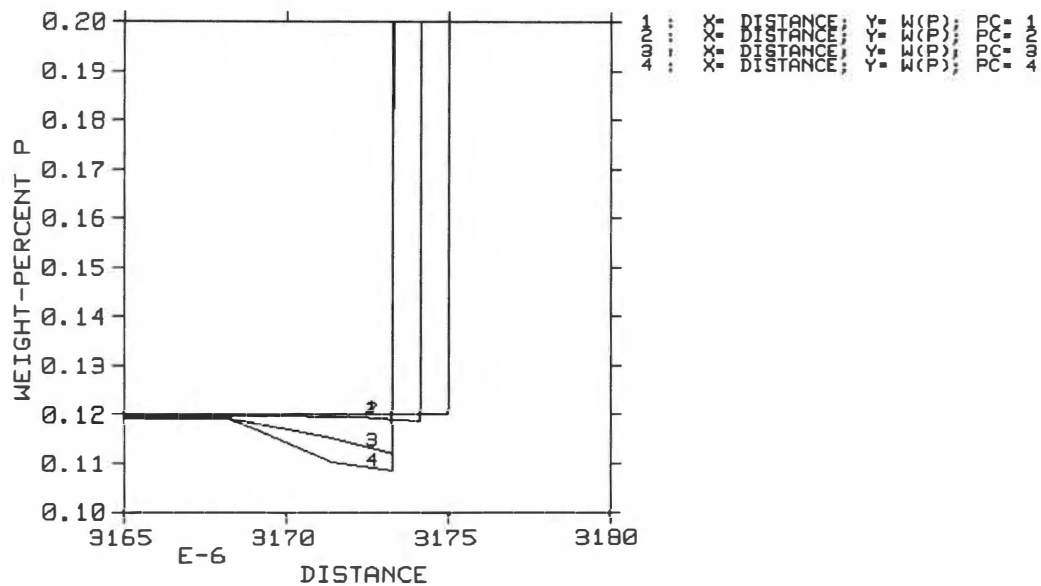   TIME = 0,1,10,20

Figure 51 Diffusion of Ni near interface at 975°C (1248K) and 0, 1, 10, 20 seconds with no C in system, part 2.

DICTRA (2002-11-26:19.22.52) :Diffusion Couple for Ni-P/ASTM A570 at 1273k
        TIME = 0,1,10,20

Figure 52 Diffusion of Ni near interface at 1000°C (1273K) and 0, 1, 10, 20 seconds with no C in system, part 1.

107

Figure 53 Diffusion of Ni near interface at 1000°C (1273K) and 0, 1, 10, 20 seconds with no C in system, part 2.
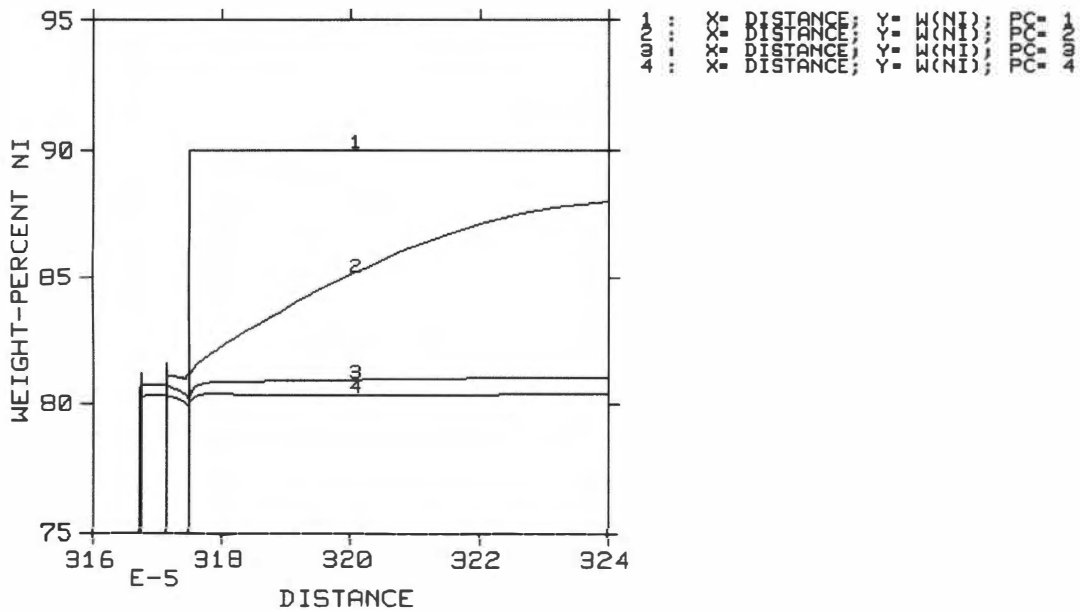
Figure 54 Diffusion of Ni near interface at 1025°C (1298K) and 0, 1, 10, 20 seconds with no C in system, part 1.

Figure 55 Diffusion of Ni near interface at 1025°C (1298K) and 0, 1, 10, 20 seconds with no C in system, part 2.

B.1.4 Diffusion Plots for Phosphorus

Figure 56 Diffusion of P near interface at 950°C (1223K) and 0, 1, 10, 20 seconds with no C in system, part 1.

```
DICTRA (2002-11-20:23.25.05) :Diffusion Near Interface
       TIME = 0,1,10,20
```

Figure 57 Diffusion of P near interface at 950°C (1223K) and 0, 1, 10, 20 seconds with no C in system, part 2.


```
DICTRA (2002-11-26:18.29.36) :Diffusion Couple for Ni-P/A570 at 1248K
       TIME = 0,1,10,20
```
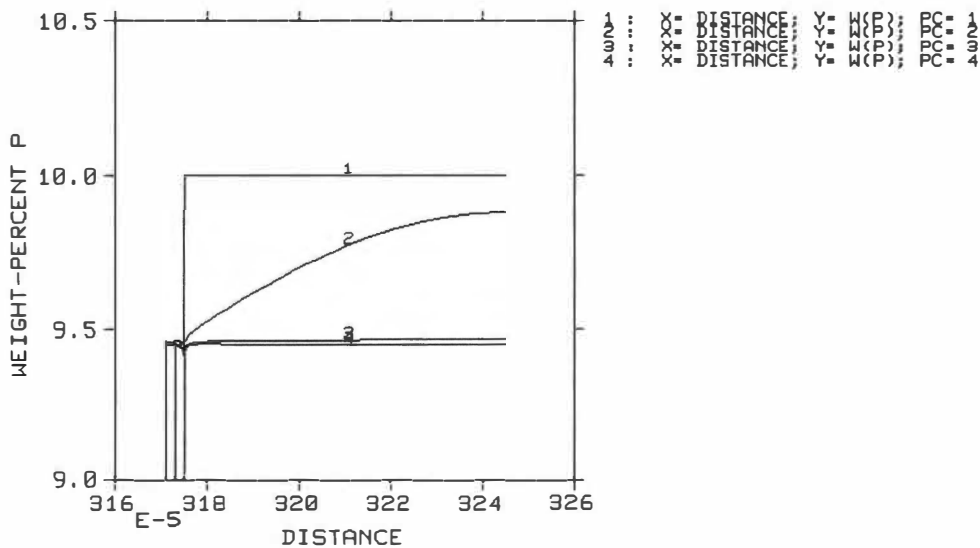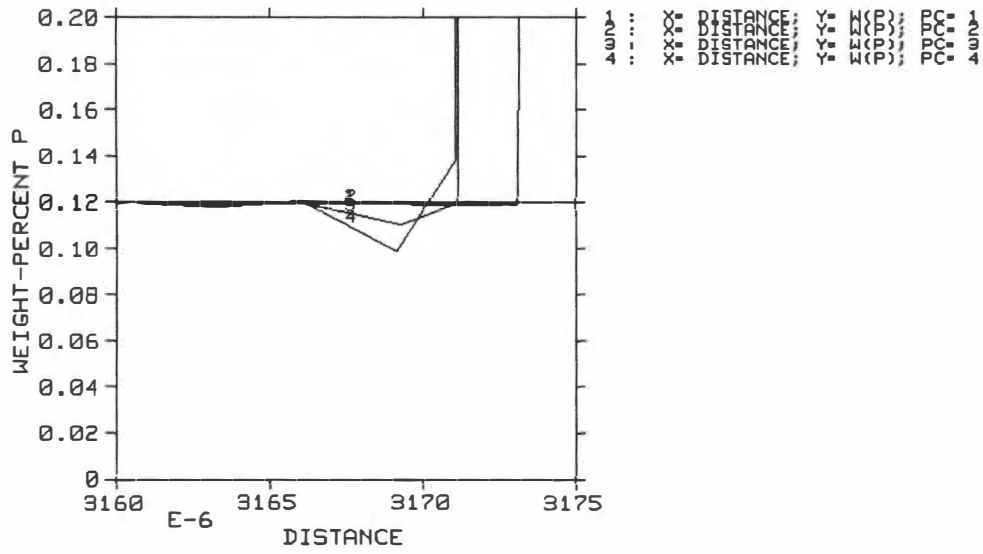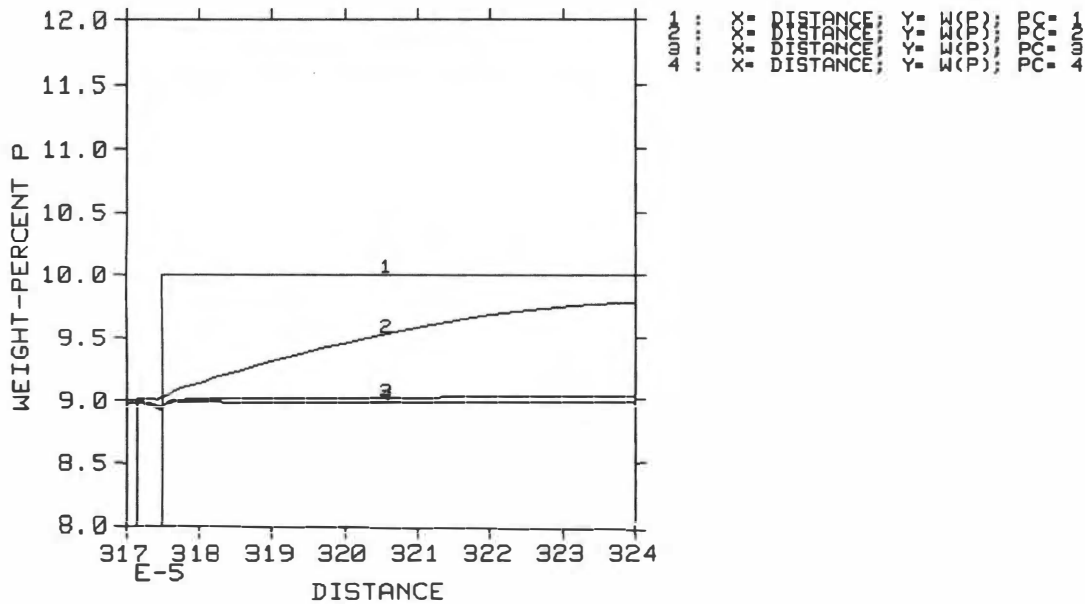
Figure 58 Diffusion of P near interface at 975°C (1248K) and 0, 1, 10, 20 seconds with no C in system, part 1.

110

Figure 59 Diffusion of P near interface at 975°C (1248K) and 0, 1, 10, 20 seconds with no C in system, part 2.

Figure 60 Diffusion of P near interface at 1000°C (1273K) and 0, 1, 10, 20 seconds with no C in system, part 1.

Figure 61 Diffusion of P near interface at 1000°C (1273K) and 0, 1, 10, 20 seconds with no C in system, part 2.

Figure 62 Diffusion of P near interface at 1025°C (1298K) and 0, 1, 10, 20 seconds with no C in system, part 1.
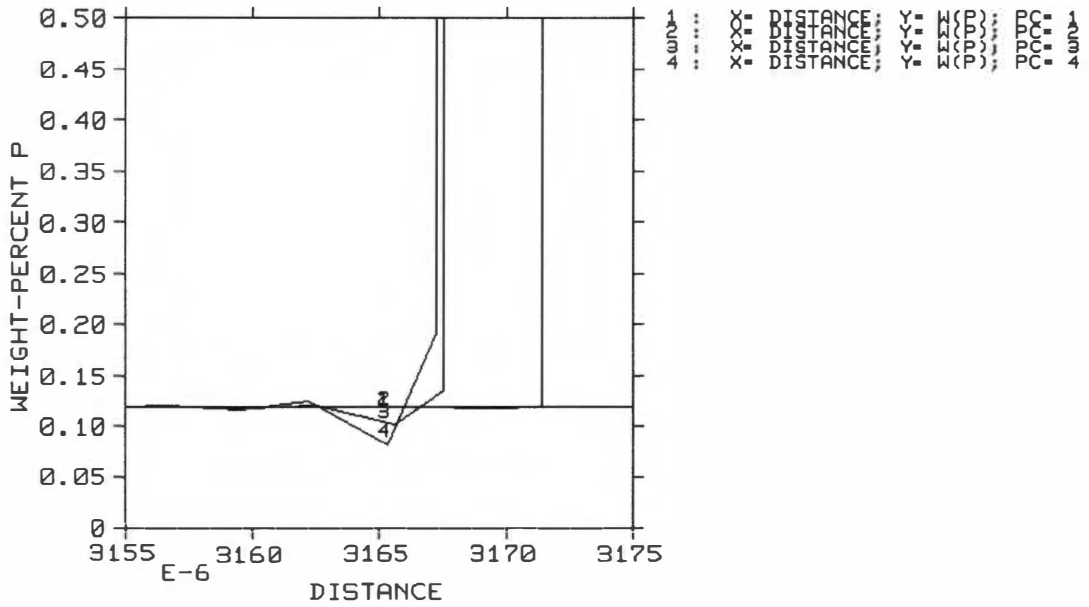
Figure 63 Diffusion of P near interface at 1025°C (1298K) and 0, 1, 10, 20 seconds with no C in system, part 2.

Vita

Greg Engleman, born in Coupeville, WA in 1971, was raised in eastern part of Washington State and transplanted to the eastern part of Tennessee in 1998. He graduated high school in 1990 and pursued a bachelors of science in physics at Central Washington University. Greg accepted a fellowship offer to work at Oak Ridge National Laboratory in 1998 and, to date, is still there pursuing his various sundry interests. During his time at ORNL, Greg decided to return to school and pursue a Masters of Science degree in Materials Science and Engineering, graduating May of 2003. Also during this time period, he decided to begin pursuing a Masters of Engineering degree at the Pennsylvania State University. To this date, Greg is still pursuing that degree, but he hopes to finish it someday.

In his spare time, Greg enjoys teaching dance, writing, hiking and finding other interests, of which there seems to be no limit. Currently, Greg is continuing to pursue those interests.